SURFACE MODIFICATION OF TITANIUM BY ELECTROLYTIC PLASMA PROCESSING AND *IN-VITRO* STUDIES

by

WISANU BOONRAWD

DISSERTATION

Submitted in Partial Fulfillment of the Requirements for the Degree of

Doctor of Philosophy

The University of Texas at Arlington

August 2021

Acknowledgements

Firstly, I would like to acknowledge and thank Dr. Efstathios I. Meletis for his valuable advice and giving me the opportunity to be part of Surface and Nanoengineering Laboratory (SaNEL) research group in the first place. I would also like to acknowledge The Royal Thai Government for granting me a full scholarship to pursue the doctoral degree in UTA. I would also like to thank Dr. Kyungsuk Yum, Dr. Harry Tibbals, Dr. Yaowu Hao, and Dr. Venu Varanasi for accepting to be members of my dissertation committee. I would also like to acknowledge and thank Dr. Jiechao Jiang and Mr. Dajing Yan for their support at The UTA Characterization Center for Materials and Biology. I also would like to acknowledge and thank Dr. Venu Varanasi and Mr. Kamal Awad from UTA's bone-muscle Research Center for the collaborative work on the *in-vitro* studies. Lastly, I sincerely acknowledge all colleagues in SaNEL research group including Dr. Hooman Rahmani, Dr. Randall Kelton, Dr. Golsa Mortazavi, Dr. Yi Shen, Dr. Nastaran Barati, and Dr. Anna Zaman for their technical assistance and support.

Dedication

To my parents and my beloved wife for their unconditional love, faith in me, limitless support, and encouragement.

Abstract

SURFACE MODIFICATION OF TITANIUM BY ELECTROLYTIC PLASMA PROCESSING AND *IN-VITRO* STYDIES

Wisanu Boonrawd, Ph.D.

The University of Texas at Arlington, 2021

Supervising Professor: Efstathios I. Meletis

Electrolytic plasma processing (EPP) can be operated in two modes, namely plasma electrolytic saturation (PES) and plasma electrolytic oxidation (PEO). In this study, the PES was used to create hydrophilic surface profiles on titanium (Ti). The wettability, surface morphology characteristics and chemical composition of the treated samples were studied as a function of PES processing parameters. The PES profiled surfaces comprised of a characteristic "hills and valleys" morphology because of continuous surface melting and freezing cycles. A bimodal surface profile was produced with 2-3 μm height hills and valleys with nano-roughness (≤ 200 nm). The produced profile resulted in a significant contact angle decrease (from 38.7° to 5.4°). Ratios of actual surface area to projection area (r) and fraction of solid surface remaining dry (φ) were obtained from profilometry. The surface characteristics and large r values produced by PES were able to induce *hemi-wicking*. Hence, PES produced superhydrophilic surfaces on Ti. The bioactivity of PES treated Ti was evaluated using cell free and MC3T3 cells *in-vitro* studies. The treated Ti surface significantly increased the bioactivity and formed stoichiometric hydroxyapatite after immersion in a bone cell culture medium for 21 days. Cells' attachment and proliferation studies indicated

that PES treated surface significantly enhances the cells' adhesion and growth after 24 and 48 hr compared to the untreated surface. The results show that Ti surface profiling by PES constitutes a promising method to potentially improve bone implant bonding.

PEO was used to produce titanium oxide (TiO_2) coatings on Ti surface in potassium – phosphate electrolyte. The morphology, wettability, phase, and chemical compositions were studied as a function of processing parameters. The bioactivity of the coating was assessed by the ability to form biomimetic apatite *in-vitro* using cell culture medium. *In-vitro* studies using human mesenchymal stem cells were also conducted to evaluate cells' proliferation and viability of the treated Ti. The results revealed that the produced TiO_2 coatings comprised pore features with the pore size increasing with applied current density and treatment duration due to high energy discharge channels at higher potential. The PEO treated Ti exhibited superhydrophilic characteristics with a contact angle <1°. The findings indicated that the large actual surface area produced by the PEO treatment and the presence of negatively charge PO_4^{3-} are the key factors for the superhydrophilic behavior. The *in-vitro* studies revealed that the PEO treated groups had higher amount of biomimetic apatite formation compared to the as-polished Ti. The PEO treatment significantly enhanced the cells' adhesion and growth after 24 and 72 hrs compared to the untreated Ti. A significant difference in the bioactivity was not observed between anatase and rutile.

Table of contents

List of tables

List of figures

Chapter 1 Introduction

1.1. Introduction and motivation

Properties of a biomaterial depend greatly on its surface characteristics. Ti has superior corrosion resistant due to a thin and stable TiO_2 film that naturally built up on the Ti surface. It also has desire mechanical properties to be used as an implant. However, a surface treatment is required to improve longevity of the Ti implant since it has poor osteoconduction and osseointegration [1][2].

A number of surface modification techniques have been explored to overcome these drawbacks. The most common solution is to coat the Ti implant with bioactive ceramics, such as calcium phosphate. Even though the osteoconduction and osseointegration have been promoted on the Ti implant by this strategy, the detachment of the coating materials often leads to implant loosening [3][4]. Recently, it has been reported that Ti with a characteristic surface texture has shown better bioactivity compared to a flat surface [5][6][7]. Furthermore, Ti with superwetting surface has beneficial for cell adherence and proliferation [6][7][8][9]. Thus, there is still room to ameliorate its bioactivity without introducing the calcium phosphate layers on the Ti implant.

Electrolytic plasma processing (EPP) is an emerging surface modification technique due to its versatility and ease of operation. It can be used to clean, create characteristic surface profile, and build up TiO_2 layer on the Ti surface, depending on a selected working polarity and electrolytic bath. Processing parameters of the EPP are also affecting the surface characteristic of the treated Ti.

EPP can be operated in cathodic, known as plasma electrolytic saturation (PES), or anodic regime, known as plasma electrolytic oxidation (PEO). The study of metal film depositions by PES has been growing in numbers because it allows various metal ions to be deposited on metal substrates by controlling ion species that present in the electrolyte [10][11]. The PES is also able to clean and create characteristic profile on a metal surface when operating in a proper electrolytic bath [12]. The produced surface profile may have positive effects on the bioactivity of the Ti since surface texture has been proven to enhance osteoconductivity and osseointegration of the Ti implants [5][6][7]. However, there is no research conducted on the bioactivity of the Ti profiling surface treated by PES.

In the view of PEO, it is used to build ceramic layers on a light metal surface. Numerous studies have been focusing on the deposition of calcium phosphate on the Ti substrate [13][14][15]. But there are only a few reports that investigate on the osteoconduction of TiO_2 films produced by PEO in the electrolytic bath that calcium ions are absent. The PEO produces the TiO_2 layers with a unique surface topography, chemical compositions, and phases [16]. Therefore, because of the need in an alternative surface modification technique to overcome the existing drawbacks of the Ti implants, it would be worthwhile to study the EPP as a promising surface treatment for the Ti implants.

This dissertation provides an opportunity to investigate the surface characteristics of EPP treated Ti at different processing parameters by conducting surface characterization studies. Moreover, the osteoconductive of the EPP treated Ti as a function of its surface characteristics will also be investigated by conducting *in-vitro* studies. Understanding the relationship of the surface characteristics and the bioactivity would be beneficial for the selection of processing parameter.

1.2. Research objectives

i. **Study the effect of EPP parameters that producing a desirable Ti surface profile for bone replacement applications by characterizing the EPP treated Ti surface in terms of surface composition, morphology, topography, and hydrophilicity.** This study provides the fundamental understanding on how the working polarity, electrolytic bath compositions, input power, and treatment duration affect the surface characteristics of the EPP treated Ti. Fundamental understanding of the wetting mechanism on the EPP treated surface will also be focused in this study. A goal of this objective is to get a desirable surface roughness and wettability. The surface composition and morphology are going to be characterized by SEM, EDS, XRD, and FTIR. An optical profilometry and a sessile drop technique will be used to evaluate the roughness and wettability of the Ti samples, respectively.

ii. ***In-vitro studies*** **of the EPP treated Ti as a function of its surface characteristics using cell free media, MC3T3-E1 pre-osteoblast cells, and human mesenchymal stem cells.** The cell free media, alpha modified minimum essential medium (α-MEM) is an appropriate media for bone cell culture studies; its ions concentration, pH, and amino acids and vitamins make it similar to that of human blood plasma. The precipitation of bone like calcium phosphate on the Ti surface after immersion in α-MEM is reflecting the osteoconductivity of the Ti surface. The *in-vitro* study using cells will also be performed to further investigate the bioactivity and cellular behavior. SEM, EDS, XRD and FTIR will be used to characterize the Ti surface after the *in-vitro* studies. These studies are going to reveal the relation of the surface characteristics of the EPP treated Ti and its bioactivity.

Chapter 2 Literature review

2.1. Ti characteristics

Ti is one of the most important metals in the industry. Its unique high strength to weight ratio brought Ti into the aerospace industry started in the 1950s. Thereafter, Ti has not limited its usage only to the aerospace industry. Ti also offers other properties as well, such as low elastic modulus, excellent biocompatibility, and superior corrosion resistance. The latter characteristic of the Ti owes to its thin passive oxide layer that naturally built up upon air exposure. Due to the desire properties mentioned earlier, Ti and its alloys have been used extensively as artificial bones, joints, and dental implants [17]. Physical properties of the Ti are listed in **Table 2.1**.

Table 2.1. Physical properties of unalloyed Ti [17]

Property	**Value**
Atomic number	22
Atomic weight (g/mol)	47.9
Density (g/cm^3)	4.54
Coefficient of thermal expansion (K^{-1}) at 20 °C	8.4×10^{-6}
Thermal conductivity (W/(mK)	19.2
Melting temperature (°C)	1668
Boiling temperature (°C)	3260
Transformation temperature (°C)	882.5
Electrical resistivity (μΩcm)	55

Pure Ti is an allotropic metal, having hexagonal closed pack (HCP) below 882 °C and starting to change to body centered cubic (BCC) above that temperature. The HCP and BCC also known as α-phase and β-phase, respectively. The α-phase is strong due to the nature of HCP structure, while the BCC structure of β-phase is more ductile. The addition of alloying elements can stabilize α-phase and β -phase to coexist below the transition temperature. The prime example of Ti alloy is Ti6Al4V, it contains 6 wt.% Al and 4wt.% V. The present of Al stabilizes the α-phase which promotes good weldability, excellent strength characteristics and oxidation resistance. The specific added amount of V stabilizes the β-phase under 882 °C and improves its strength [18]. Some important mechanical properties of commercially pure Ti (CP grade 1 - 4) and Ti6Al4V are summarized in **Table 2.2**.

Table 2.2. Mechanical properties of commercial Ti (ASTM F67, F136)

Property	**Grade 1**	**Grade 2**	**Grade 3**	**Grade 4**	**Ti6Al4V**
Tensile strength (MPa)	240	345	450	550	860
Yield Strength (MPa)	170	275	380	485	795
Elongation (%)	24	20	18	15	10
Modulus of elasticity (GPa)	103	103	103	105	114
Hardness (HV)	128	160	191	251	327

Ti and its alloys are used in artificial hip joints, consist of an artificial bearing (femoral head, liner, and acetabular cup) and stem. The artificial bearing is made up from different materials, the femoral head and cup are usually made from very low friction materials since their functions require excellent wear property. The femoral head can be a ceramic material coupling with an ultra-high molecular weight polyethylene liner. The acetabular cup and the stem are

usually made of Ti alloys [19]. The schematic picture of artificial hip joint is shown in **Fig. 2.1**. Ti and its alloys are also used commonly as dental implants. Although Ti and its alloys are biocompatible, its bioinertness requires surface modification to improve osteoconductivity and osseointegration in order for them to fuse with surrounding bones. Numerous techniques have been implemented to ameliorate bioactivity of Ti, such as grit blasting, coating, chemical etching, anodizing, and alkaline treatments [5][20][21].

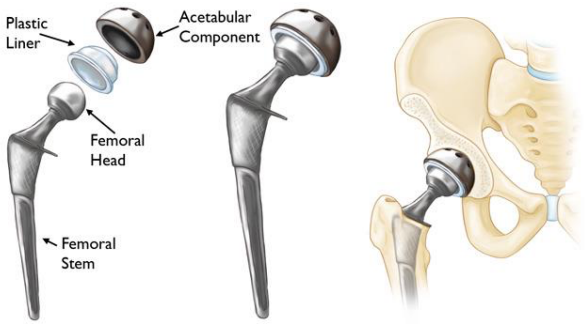

Fig. 2.1. Schematic of an artificial hip joints

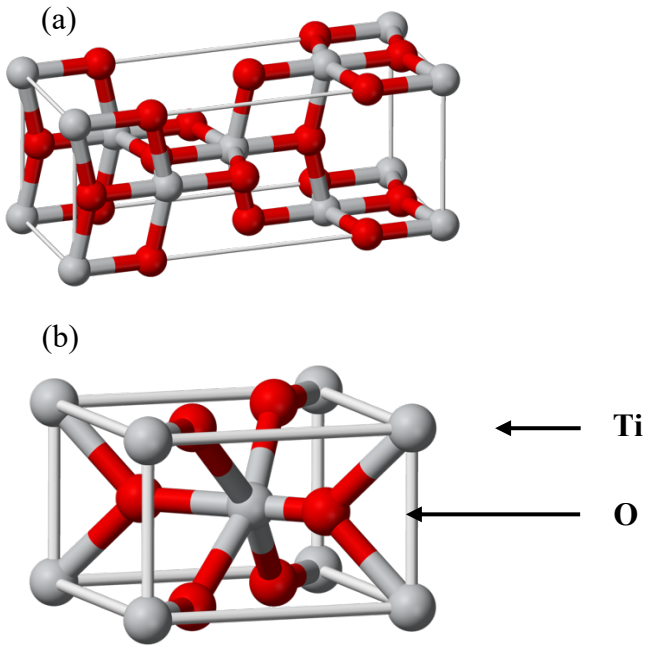

Fig. 2.2. Crystal structure of **(a)** anatase and **(b)** rutile

As mentioned earlier, the stable oxide film, TiO_2, grows spontaneously on the Ti surface when exposed to air. Thickness of the natural TiO_2 film typically ranges from 3 – 10 nm. TiO_2 can be found in 3 different phases at ambient pressure, namely anatase, brookite, and rutile. Brookite has orthorhombic crystal structure with lattice parameters a = 0.5456 nm, b = 0.9182 nm and c = 0.5143 nm. Anatase and rutile have tetragonal crystal structure with lattice parameters a = 0.3785 nm, c = 0.9514 and a = 0.4593, c = 0.2959, respectively. **Fig. 2.2** presents crystal structure of anatase and rutile. Rutile is the most stable form, thermodynamically, while anatase and brookite are metastable [22][23]. However, anatase is kinetically favored due to its open structure, hence it is usually the product of Ti oxidation. The crystal structure of rutile is more compact, thus, it is more difficult for short-range ordered TiO_6 octahedra to form long-range ordered of rutile than anatase. Furthermore, surface free energy of rutile is higher which results in slower recrystallization of rutile compared to anatase [24]. Metastable anatase can transform to stable rutile (ART) at the temperature between 600 – 1000 °C and there must be sufficient time allowing for the transformation to occur.

Various surface modification techniques have been used to produce TiO_2 films. It is possible to control the oxidation product of Ti by selecting proper processing parameters. Mortazavi et al. have investigated TiO_2 films prepared by PEO on Ti substrates at difference applied current densities, 30 – 120 mA/cm^2. The treatment durations were different, the treatment was stopped when arcing observed. The produced oxides were mainly comprised of anatase, since it was kinetically preferred as described above. However, when applied current density was at 30 mA/cm^2 rutile and anatase were both present because the heat generated from plasma and treatment time was sufficient for ART to occur [16]. In general, the treatment duration in PEO is limited by the occurrence of arcing. The arcing is avoided because it deteriorates the integrity of the produced

oxide layer. Thus, the lower applied current density the longer treatment duration until arcing will be observed due to slower oxide built up to reach critical thickness.

In view of the bioactivity, anatase and rutile are both able to induce osteoconduction when immersed in simulated body fluid (SBF) [25][26][27][28]. Nonetheless, there is a contradiction on which phase has better osteoconduction. Uchida et al. studied the formation of apatite on TiO_2 prepared by sol solutions. The authors postulated that anatase exhibited better osteoconduction than rutile due to the crystallographic matching between the apatite (0001) plane and the anatase (001) plane [28]. This was in a good agreement with TiO_2 prepared by electrolytic deposition in alcoholic solution and plasma electrolytic oxidation in KOH + $K_4P_2O_7$ electrolytes [29][30]. On the other hands, TiO_2 that contained rutile prepared by anodic arc oxidation in H_2SO_4 + CH_3COOH + H_3PO_4 electrolytes have shown better bioactivity than anatase [27][31]. Moritz el al. have also compared the bioactivity of anatase and rutile with two different surface modification techniques, namely heat treatment and CO_2 laser treatment. The anatase from heat treatment process exhibited better bioactivity than rutile, but the anatase prepared by CO_2 laser treatment has shown the opposite results. It should be noted that the TiO_2 prepared by heat treatment lacks OH-group on the surface. The authors proposed that surface functional groups also play an important role for osteoconduction [26]. It is clearly seen that TiO_2 produced from a different surface modification technique has unique bioactivity level because there are a number of factors to be accounted. Hence, more studies on the bioactivity of TiO_2 should be conducted in order to understand the nature of it.

2.2. Surface modification techniques to improve bioactivity of Ti

A bioactive surface is related to the ability of the surface to facilitate biomineralization, which helps to diminish an adverse host response and facilitate the formation of direct bonding with the bone [32]. Several techniques have been explored to improve osteoconduction and osseointegration of Ti and its alloys. Most of the studies have aimed to deposit bioactive calcium phosphate layers on top of the Ti surface. The idea is to combine the desire mechanical properties of Ti and the excellent osteoconductive of calcium phosphate, especially hydroxyapatite phase (HA). However, each technique has its own advantages and disadvantages. Recently, the modification of the Ti surface has not only limited to the coating of calcium phosphate layers. There are more reports on positive effects of surface texturing and wettability on the bioactivity [5][6][7][8][9]. Thus, any surface medication that has the ability to control surface topography and wettability is worthwhile to investigate.

2.2.1. Plasma spraying

Plasma spraying process is a form of thermal spraying processes. It has been one of the most popular coating techniques to deposit calcium phosphate on Ti substrates. The plasma spraying system consists of a plasma source providing heat from ionized inert gas and a feedstock supplying coating materials (coating precursors). The coating materials can be metals, alloys, ceramics, plastics and composites. They can be fed in a form of powder or wire. The coating materials are melted by very high temperature plasma then accelerated towards and deposited on a substrate surface. Plasma spraying can produce coatings with thickness ranges from 20 μm to several mm at high deposition rate and considerably low operation cost compared to other coating techniques [33].

Levingstone et al. studied the effect of plasma spraying processing parameters on the HA coatings in terms of roughness, crystallinity and purity [34]. The current, gas flow rate, powder feed rate, spray distance and carrier gas flow rate were varied. The roughness of the coatings increased when current was high, gas flow rate was low and powder feed rate was high due to less splat flattening was occurred. Coating crystallinity was highest at high current, short spray distance and low gas flow rate. This is due to short spray distance can increase the temperature of the substrate and allow the amorphous film to crystallize. The phase decomposition of HA to other less stable phases decreased when the spray conditions produced low temperature particles. However, this would reduce adhesion strength of the HA coatings to the substrate. There was no report on bioactivity of the HA coatings in this study. Hung et al. also studied plasma sprayed coating of HA for dental implant in terms of biocompatibility and mechanical properties [35]. The coatings were produced with different processing parameters depositing on Ti6Al4V substrates. High purity crystalline HA powder was used as a precursor. The coatings were mainly comprised of HA and some α –TCP, β – TCP phases due to phase decomposition during high temperature plasma spraying process. The coating thickness, surface roughness (S_a) and adhesion strength of the coatings to the substrate were 47 – 130 μm, 6.20 μm and 41.44 MPa, respectively. The bioactivity test by immersing in SBF for 28 days revealed the increasing of crystallinity amount of HA.

More studies have also reported that plasma spraying of calcium phosphate coatings are having phase decomposition and poor adhesion strength [3][36]. This can lead to poor service reliability and mechanical integrity of the Ti prosthesis when implanted [37].

2.2.2. Sputter coating

Sputtering technique is a physical vapor deposition (PVD) method. It involves ejecting materials from a source, known as a target, then depositing on a substrate surface in a vacuum chamber. The sputtering process utilizes plasma gas, usually argon gas, in a very low-pressure chamber to remove materials from the negatively charged target. The knocked-out materials will then deposit and form thin layers on the substrate surface. Dense and uniform coatings with high adhesion strength can be produced by the sputtering technique. Calcium phosphate and composite coatings can be achieved by radio frequency magnetron sputtering.

Stoica et al. have conducted a research on magnetron sputtering of HA. The as deposited HA coatings were amorphous. Post-heat treatment at 550 °C for 1 hour in air environment was performed to regain crystalline HA [38]. Lenis et al. studied the effect of thermal treatment of the HA coatings by RF magnetron sputtering with bias substrate voltage. It has been reported that annealing at higher temperature resulted in higher crystallinity. However, the high temperature annealing has an adverse effect on the adhesion strength of the coating and underlying substrate [39]. Boonrawd et al. also observed similar behavior on heat-treated sputtered HA/Ti composite coatings. The crystallinity and adhesion strength of the produced films increased with increasing annealing temperature. However, annealing the coatings at temperature of 700 °C, the adhesion strength of the films decreased dramatically. This is due to the mismatch of thermal expansion coefficient between the HA coatings and underlying substrates that caused the delamination of the coatings during high temperature heat treatment [40].

Even though, sputtering can produce HA coatings with high adhesion strength, the coatings still need post-heat treatment to acquire the proper crystalline phase. It is important to note that the

heat-treatment process can decrease the adherence of the HA coatings. Moreover, the sputtering technique is a line-of-sight process. Complicated substrate holder design is needed for complex substrate geometry in order to create uniform coatings at hidden areas.

2.2.3. Sol-gel derived coating

Sol-gel process involves the formation of solid materials, mainly inorganic non-metallic materials from a solution. The sol – gel process consists of;

(i) Producing a homogeneous solution of purified precursors in an organic solvent which can be mixed with the reagent used in the next step or water.

(ii) Shaping the solution to a sol form by using treatment with a suitable reagent, e.g. water for oxide ceramics.

(iii) Changing the sol to a gel by polycondensation.

(iv) Converting the gel to the finally preferred shape like thin film, and fiber.

(v) Finally converting the shaped gel to the desired ceramic material at temperatures (~500 °C) much lower than those required in the conventional procedure of melting the oxides together [41].

The sol – gel coating technique produces thin coating with high purity and high adhesion to substrates. It also offers flexibility to coat a substrate with complex geometry. The sintering is done at relatively low temperature, usually in the range of 200 – 600 °C. However, high permeability, low wear resistance, and difficult porosity control are the main drawbacks for the sol – gel technique. Furthermore, the thermal process always introduces crack in the coatings thicker than 0.5 μm and trapped organic substance would result in coating failure [42]. Depositing a desire calcium phosphate phase by the sol – gel coating technique requires extremely stringent processing

parameters, particularly for the thermal processing phase, such as the duration and calcination temperature, chemical compositions of the precursor, types of substrate, and number of coating layers. These disadvantages of sol – gel technique have limited its usage for the industry [43][44][45].

2.2.4. Chemical treatment

A postulate that Ti – OH group on Ti surface is beneficial for the apatite nucleation has ignited the study on chemical treatment of Ti and its alloys [46]. The most common chemical treatments are done in an alkaline solution, such as NaOH and KOH due to the presence of OH^- group can easily attach to the Ti surface. It should be noted that treated Ti with NaOH has shown better apatite formation ability than KOH [47][48][49][50]. The treatment is usually done by soaking Ti substrates in 5 – 10 M NaOH at 60 °C for 24 hrs. The mechanism behind the formation of apatite is described as followed. During the alkaline treatment in NaOH, the thin native TiO_2 layer reacted with NaOH to form sodium titanate gel layer. The titanate layer is expected to form a number of Ti – OH groups on the Ti surface when in contact with body fluid via Na^+ ions exchange with H_3O^+ ions in the body fluid. These Ni – OH groups are negatively charged in the SBF at pH = 7.4, then an amorphous calcium titanate is formed by combining with positively charged Ca^{2+} ions. At some point, the surface becomes positively charged due to the accumulation of Ca^{2+} ions, hence it combines with phosphate ions in SBF and form amorphous calcium phosphate. Finally, the amorphous calcium phosphate transforms to apatite, the thermodynamically stable phase [47][51][52].

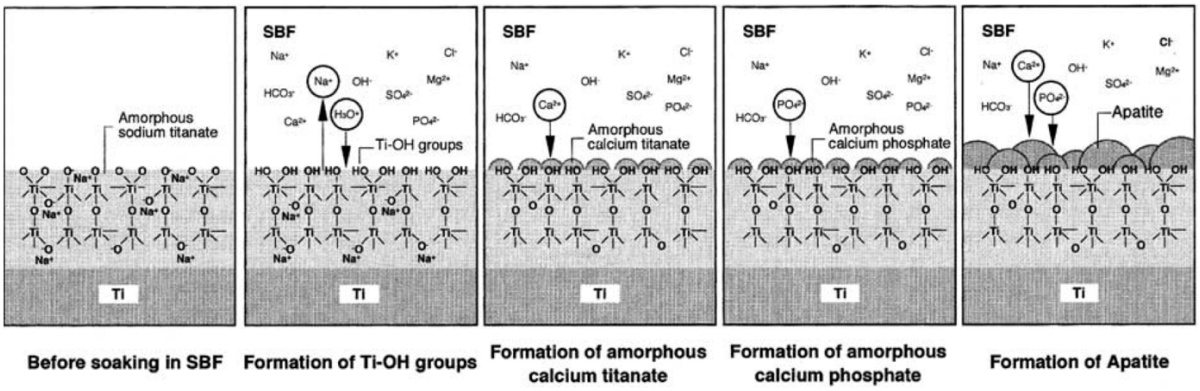

Fig. 2.3. Mechanism of the apatite formation on the NaOH- and heat-treated Ti in SBF [51]

It has been reported that thermal treatment after alkaline treatment is improving the osteoconduction and osseointegration of the Ti. Kawai et al. have studied the apatite formation on NaOH treated Ti surface. The effect of post-heat treatment was also investigated. The post-heat treatment after alkaline treatment promoted better apatite formation in SBF compared to the alkaline treated alone [53]. The mechanism of the apatite formation on the NaOH and heat-treated Ti is shown in **Fig. 2.3**. Wei et al. has designed a study on alkaline treatment with various processing parameters, such as the NaOH concentration, soaking duration, soaking temperature, and post-heat treatment temperature to optimize the osteoconduction and osseointegration of the Ti6Al4V. It was found that soaking in the 5 M NaOH at 80 followed by heat-treatment at 600 °C for 1 hr had the best osteoconduction. The apatite was formed on the treated Ti alloys after immersion in SBF for only 3 days. It should be noted that when the heat-treatment temperature was at 700 °C, the ability to induce apatite formation in SBF has decreased [54].

The alkaline treatment is a promising surface modification technique for bone replacement applications due to the simplicity of the process and relatively low operation cost. The ability to induce osteoconductivity and osseointegration has already been proven in *iv-vitro* and *in-vivo* [51]. However, the need of post-heat treatment could have a negative effect to the underlying substrate

due to the possible change of microstructure. The heating and cooling rate have to be carefully controlled.

2.2.5. Surface texturing

Ti with texture profile on the surface behaves differently from flat surface. It has been reported that Ti with a profile texture is able to attract osteoblast cells to adhere on the surface and increase protein adsorption. These osteoblast cells are important for bone regeneration process on the implants [5]. Moreover, increasing surface roughness of Ti resulted in improving bone integration, osteoconduction and osteogenesis [55]. The prefer roughness is in the range of 1-2 μm, however additional nano-submicrometer features play an important role for the bioactivity as well [6][20][21].

Numerous surface texturing techniques have been explored to produce a desire surface profile for hard tissue replacement applications. Schwarz et al. studied the effect of surface roughness and porosity on osseointegration of titanium in a minipig model using glass pearl blasting, sand blasting, plasma spraying Ti particles and plasma spraying Ti particles then electrochemically deposited a thin layer of resorbable calcium phosphate. The result of *in-vivo* studies revealed that rougher surface giving higher implant anchorage and osseointegration. It is good to note that the resorbable of calcium phosphate enhanced significant amount of bone growing on the implant but not the level of anchorage [56]. Alenezi et al. investigated the osseointegration, bone – implant contact (BIC), percentage and the bone area (new – BA), and new bone area (BA), of 2 commercially available Ti implants with and without nanotopography texture by conducting an *in-vivo* study in 12 rabbits. The sample with nanotopography texture prepared by TiO_2 micro – blasted then bombarded with noble gas ion. The other group prepared

by anodic oxidation process in an electrolytic bath that contained Ca and P. The statistical analysis results revealed that both groups have shown strong osseointegration properties, but there are no significant differences in BIC and in total BA. However, the new – BA has significantly higher percentage for the implant with nanotopography [21]. Similar results have been reported by Xu et al. [57]. Selective laser melting (SLM) was used to create Ti substrate with micro-rough surface. The SLM Ti substrates were then subjected to various additional surface modification processes. The first group, control group, was the as manufactured SLM Ti. The rest of the SLM samples were sandblasted with 250 μm ZrO_2 particles then immersed in an acidic mixture of 40% HF and 60% HNO_3 (H_2O/HF/HNO_3, 1:4:5, v:v:v) for 2 minutes to remove oxide layer and then polished. The second group of substrates was subjected to sandblasting/acid etching (SLA) process, acid etch in 98% H_2SO_4 and 36.5% HCl solution (H_2O/HCl/H_2SO_4, 2:4:3, v:v:v) at 95 °C for 15 minutes. For the third group, SAN, the polished specimens were used as the electrode anode with a titanium rod as a cathode and were anodized in a 0.5 wt% HF in distilled water solution using 20 V power supply for 45 minutes. For the fourth group, alkaline treatment (SAH), the sandblasted specimens were treated with NaOH solution for 8 hours. All specimens were then clean and subjected to *in-vivo study* in rabbits for 4 and 8 weeks. The results revealed that, even though there was no bioactive material coating, surface with micro-/nano-textured hierarchical topographies enhanced bone regeneration and BIC. The SAH treatment showed higher bone-implant contact percentage, almost double compared to that of native-SLM and SLA group.

It has only been recently found that the surface topography and the present of the nano-submicrometer textures on top of the rough profile have positive effects to the bioactivity of Ti implants. More studies on improving bioactivity of the Ti are focusing on surface modification

techniques that possess the ability to create such rough profile on the Ti implants. An alternative surface modification technique which is environmental friendly and cost efficiency is still needed.

2.3. Electrolytic plasma processing

Electrolytic plasma processing (EPP) is an electrochemical process operating at a high electrical potential range in an aqueous environment. It involves electrolysis of the aqueous electrolyte accompanied by several electrode processes. The EPP system consists of a power supply, an electrolytic cell, aqueous electrolytes, and two electrodes. The aqueous electrolyte acts as a conductive bridge between the two electrodes. It can be used to clean a metal surface and coat metal films on a metal substrate when connected the workpiece to the negative electrode. A thick oxide layer can be built up on a light metal surface when connecting the workpiece to the positive electrode by oxidation process. However, the oxidation process can also dissolve the oxide depending on the electrolyte chemical activity. **Fig. 2.4** represents the electrodes reactions in electrolysis of aqueous solutions.

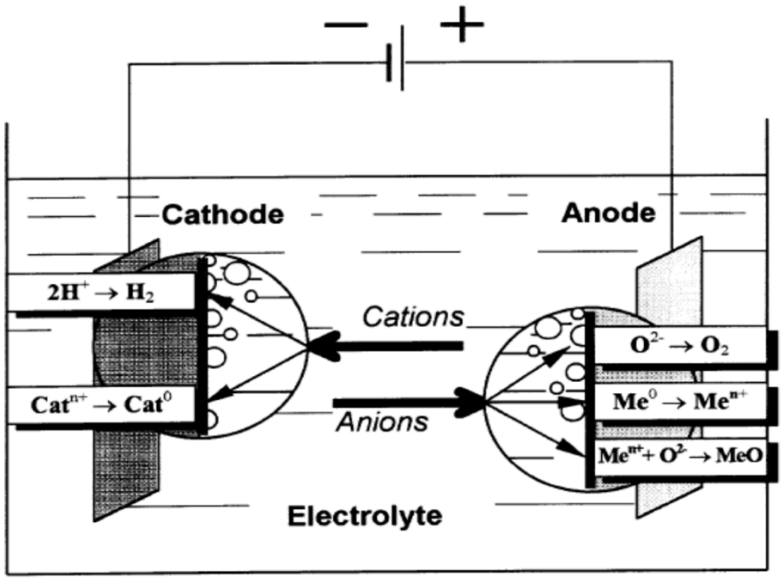

Fig. 2.4. Electrode reactions in electrolysis of aqueous solutions [58]

2.3.1. Plasma electrolytic saturation

The EPP is also known as plasma electrolytic saturation (PES) when the workpiece is connected to the negative electrode, cathodic process. During the applying of high electrical potential, the liberation of gaseous hydrogen and cation reduction occur on the cathodic surface. The cation species present in the electrolyte are drawn to interact with the substrate surface. Hence, the PES can deposit various metal ions by carefully choosing the compositions of the electrolytic bath. It can also utilize hydrogen plasma to clean a metal surface and create unique surface profile when performing PES in an electrolytic bath containing $NaHCO_3$. The cleaning process of PES requires simple set up and nontoxic chemical compared to tradition surface cleaning, such as acid pickling.

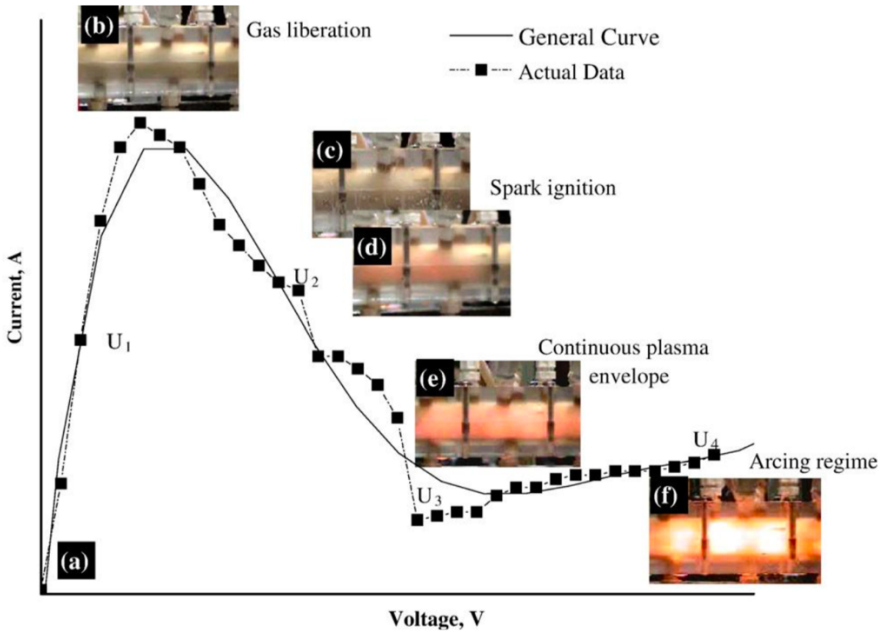

Fig. 2.5. A general current – voltage response of PES process [59]

Fig. 2.5 presents a typical current – voltage plot of the PES process. The mechanism of PES can be divided into four stages;

(i) The production of fine hydrogen gas (gas liberation) due to a strong electric field from the applied potential to the electrodes, at this stage the current is increased with the applied potential.

(ii) Scatter plasma starts to appear at the workpiece surface, at this stage the current drops sharply due to the breakdown of the electric field.

(iii) As increasing the applied potential further, the current drops to the lowest point and the plasma becomes stable and uniform. This stage is defined as working region or Kellog's region.

(iv) In the last stage, increasing the applied potential further, the current starts to increase again, and intense arcing is observed. Hence, the arcing is usually avoided because it causes deterioration of the surface.

The PES treated surface is usually comprised of submicron hill and valley features, due to the collapse of the generated plasma. An energetic shock wave from the collapsed plasma bubbles melts the substrate surface, then subsequently freezing event occurs due to the present of aqueous electrolyte. When the electrolytic bath contains metal cation species, a thick and high adhesion metal coating is formed in less than a minute of processing time. The cleaning effect takes place when the electrolytic bath only contains hydrogen cations. Thus, performing PES in $NaHCO_3$ electrolyte will provide clean surface with desirable surface characteristics which could be beneficial for rapid osteoconduction.

As described earlier, the process characteristics of the PES are possible to improve the osteoconduction of Ti surface. It is important to note that there is no report on how Ti surface

prepared by PES supports osteoconduction *in-vitro* and *in-vivo*. Furthermore, the wettability of PES treated Ti as a function of its surface characteristics has not been studied yet.

2.3.2. Plasma electrolytic oxidation

Plasma electrolytic oxidation (PEO), also known as micro arc oxidation (MAO), is similar to the PES but the working electrode is connected to the positive panel. It is widely used to build up thick oxide layers on light metals, such as aluminum, magnesium and titanium. PEO produces hard, corrosion and wear resistance oxides on the metal surface at high deposition rates. The principle of PEO is similar to anodizing but operating at higher potentials which results in generation of plasma discharges. Formation of these microdischarges produce high temperature resulting in conversion of the substrate into the coating and production of high adhesion strength coatings [60][61].

During PEO, the working electrode is surrounding by a continuous gas envelope of oxygen. Highly localized electric field is generated by high voltages between the electrodes. This strong electric field leads to implosion of bubbles and ionization of gas space inside the bubbles, then a plasma discharge is initiated. The temperature of the microdischarges is estimated between 8,000 to 10,000 K in the core and as high as 2,000 °C at their surroundings [12][62]. It is reported that high temperature of the plasma discharges leads to the localized melting of the substrate close to the discharges and forming discharge channels. Furthermore, anionic species present in the electrolytic bath enter these channels under the strong electric field and react with cations of substrate and forming oxides. During PEO processing, cations move outwards and oxygen ions and other anions move toward the substrate. Depending on the nature of the substrate, electrolyte, and mobility of ions, the inward and outward growth rate can change [63][64][65].

A typical mechanism of PEO treatment as a function of voltage and time is shown in **Fig. 2.6** and can be divided into three stages:

(i) The first stage is similar to the traditional anodizing process where the increasing of voltage is almost linearly with time. Numerous bubbles containing oxygen are formed near the workpiece surface due to the electrolysis of water. This stage involves a formation and growth of a passive film on the substrate. Thus, the voltage increases as the thickness of the oxides increased.

(ii) When the voltage reaches breakdown point, the rate of voltage increasing is slowly decreased, also scattered and fine spark appear on the workpiece due to the discharge of plasma. At this stage, the extremely high potential between the two electrodes triggers the breakdown of the dielectric layers. This resulting in cycles of the very high temperature local melting at the zone of developed microdischarges and quenching of oxides due to the present of the cold electrolyte. The PEO is usually done within this stage.

(iii) At the last stage, the voltage is nearly stable, also intense sparks are noticeable. When the critical thickness of the oxides has reached, an intense arcing will appear at a particular area. This results in deterioration of the oxide layers. It is good to note that these three stages can vary depending on workpiece material and electrolytic bath compositions.

PEO has also been explored as a surface modification technique for Ti implant because of its ease of use and versatility. The compositions of chemical in the electrolytic bath, current density and other processing parameters have been reported to affect the coating characteristics (thickness, roughness, and phases). The key phases of PEO produced coatings for bioapplications are HA and other calcium phosphate phases. These phases are bioactive and can support osteoconduction rapidly when implanted in living systems.

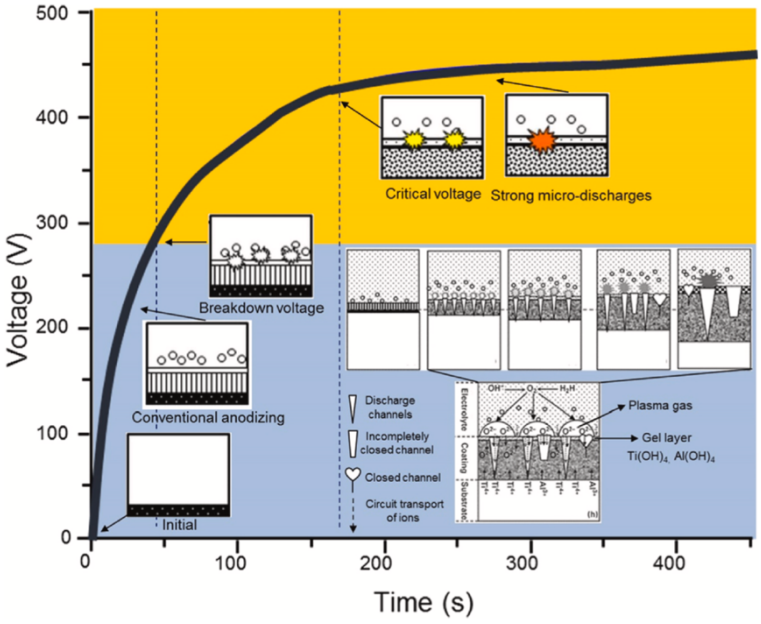

Fig. 2.6. PEO treatment as a function of voltage and time [66]

Song et al. performed PEO on Ti substrates in an electrolyte containing β-glycerophosphate disodium salt pentahydrate and calcium acetate monohydrate. The applied voltage was ranged from 250 – 500 V. The produced titanium oxide films contain Ca and P which strongly dependent on the applied voltage. The compounds such as $CaTiO_3$, β-$Ca_2P_2O_7$ and α-$Ca_3(PO_4)_2$ were produced at voltage higher than 450 V. The coatings were able to induce biomimetic HA after immersed in SBF for 28 days [67]. Faghili-Sani et al. also performed PEO on Ti alloys in an electrolyte containing calcium acetate and calcium glycerophosphate. But the Ca/P molar ratio was adjusted to 6.8. The applied current density was 0.212 A/cm^2, frequency of 100 Hz and duty ratio of 60% for 4 minutes. The PEO films were then subjected to hydrothermal treatment in an autoclave containing NaOH solution, pH 11.5, at different temperature and duration. The HA was detected by XRD after hydrothermal treated above 160 °C at least 10 hours. The crystallinity of HA increased as the hydrothermal temperature and duration increased. However, XRD did not detect HA on the as-produced PEO films and the heat-treated for 5 hours

at 160 °C [68]. As mentioned earlier, post-heat treatment could deteriorate the adhesion strength of the coatings. Durdu et al. also performed PEO on Ti alloys in an electrolyte containing calcium acetate and β-calcium glycerophosphate using and alternate current power supply at current density of 0.123 A/cm^2. The treatment duration was 1, 5, 10, 20, 40, 60, and 120 minutes. After treated for 5 minutes, small amount of HA was detected by XRD. The highest HA crystallinity was reported on the PEO treated for 120 minutes [69]. It should be noted that the treatment parameters affect not only the phase that presents in the coating but also surface morphology and topography. The change of surface morphology and topography could affect the cellular response. Unfortunately, these studies have not performed cellular response studies on the PEO treated samples.

2.4. Surface roughness

Surface topography of a surface can be quantitatively characterized by contact and non-contact scanning techniques. The latter technique is usually preferred since it gives better resolution and does not alter specimen surface. The parameters that characterize the overall morphology of the surface in this study are Sa, Sz, Ssk, and Sdr.

Sa (arithmetical mean height) is the extension of the traditional Ra (arithmetical mean height of a line) to a surface. It is representing a surface roughness within the sampling area by expressing, as an absolute value, the difference in height of each point compared to the arithmetical mean of the surface. The *Sa* is approximated by the following equation (2-2) [70]:

$$Ra = \frac{1}{l}\int_0^l |Z(x)|dx \qquad (2\text{-}1)$$

$$Sa = \frac{1}{A}\iint_A |Z(x,y)|dxdy \qquad (2\text{-}2)$$

where *A* in the integral expressions implies that the integration is performed over the area of measurement and then normalized by the cross-sectional area of the measurement, and *Z* is the surface height relative to the reference mean plane.

Sz is the ten-point height over the sampling area. It represents the average difference between the five highest peaks and five lowest valleys. The *Sz* can be estimated following equation (2-3):

$$Sz = [\sum_1^5 |Peak\ Heights| + \sum_1^5 |Valley\ Depths|]/5 \qquad (2\text{-}3)$$

Ssk or skewness is the ratio of the mean of the height cubed and the cube of *Sq* within a sampling area. The *Ssk* can be estimated following equation (2-4):

$$Ssk = \frac{1}{Sq^3}\frac{1}{A}\iint_A Z^3(x,y)dxdy \qquad (2\text{-}4)$$

where *Sq* is the root mean square height within a sampling area, it can be estimated using equation (2-5):

$$Sq = \sqrt{\frac{1}{A}\iint_A Z(x,y)dxdy} \qquad (2\text{-}5)$$

The *Ssk* parameter is used to evaluate a profile symmetry of a surface. Its value can be positive, negative or zero. The negative skew means the bulk of the material is above the mean plane where the positive skew is the opposite. This implies that the surface with negative skew is mostly comprised deep valleys rather than spikes. The zero skewness means the surface is more symmetric with having a distribution curve followed Gaussian distribution [70].

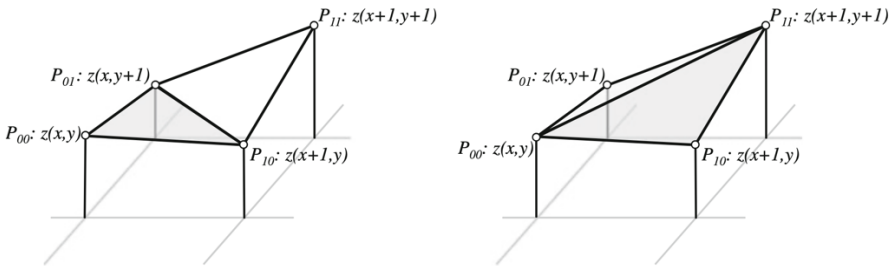

Fig. 2.7. Area between four adjacent points calculated by the average of two triangles

Sdr or the developed interfacial area ratio is expressed as the percentage of additional surface area contributed by the texture as compared to an ideal plane. The developed interfacial area of a surface can be calculated by summing the local area when following curvature. It can be estimated by the mean area of two triangles formed between four adjacent points, shown in **Fig. 2.7**. The area of a triangle is half the cross product of two vectors as shown in equation (2-6) [70]:

$$A_{00} = \frac{1}{2}\begin{bmatrix} \frac{1}{2}\left(\left|\overrightarrow{P_{00}P_{01}} \mathrm{x} \overrightarrow{P_{00}P_{10}}\right| + \left|\overrightarrow{P_{11}P_{01}} \mathrm{x} \overrightarrow{P_{11}P_{10}}\right|\right) \\ + \\ \frac{1}{2}\left(\left|\overrightarrow{P_{10}P_{00}} \mathrm{x} \overrightarrow{P_{10}P_{11}}\right| + \left|\overrightarrow{P_{01}P_{00}} \mathrm{x} \overrightarrow{P_{01}P_{11}}\right|\right) \end{bmatrix} \quad (2\text{-}6)$$

Equation (2-7) below is used to calculate Sdr, where A_{ij} is the mean area calculated at a point, and A is the projected area calculated by the product of the lengths in x and y.

$$Sdr = \frac{\sum\sum A_{ij} - A}{A} \quad (2\text{-}7)$$

From equation (2-6), it can be seen that *Sdr* is related to the ratio of the actual surface to the projected surface area (*r*). The *r* will be discussed as one of the most crucial surface characteristics in superwetting behavior in the next section. It can be simply calculated using equation (2-8). The *Sdr* is equal to zero when the surface is ideally smooth.

$$r = Sdr + 1 \quad (2.8)$$

2.5. Surface wetting

Wettability of a material is the ability of a liquid droplet to spread on the surface of the material. It plays an important role in various applications ranging from anti-fogging and heat exchanging to self-cleaning and bone replacement applications. Wettability of a surface relates to its surface energy, which is a result of inherent surface chemistry and topography [71][72]. A simple way to describe wettability of a solid surface has been proposed by Young as early as 1804 [73]. Young treats contact angle (CA) of a droplet as a result of mechanical equilibrium of three surface tensions, as shown in **Fig. 2.8**. Young's equilibrium equation is described by:

$$\gamma_{SV} - \gamma_{SL} = \gamma_{LV} \cos\theta \quad (2\text{-}9)$$

where γ_{LV}, γ_{SV} and γ_{SL} are the surface tension at the interface of liquid-vapor phases, solid-vapor phases, and solid-liquid phases, respectively [74]. Later on 1936, Wenzel reported that surface roughness can affect wettability of a material [75], as described in equation (2-10):

$$\cos\theta_A = r \cos\theta \quad (2\text{-}10)$$

where r is the ratio of actual surface area to projected area, θ_A and θ are the apparent CA on a rough surface and a flat surface, respectively.

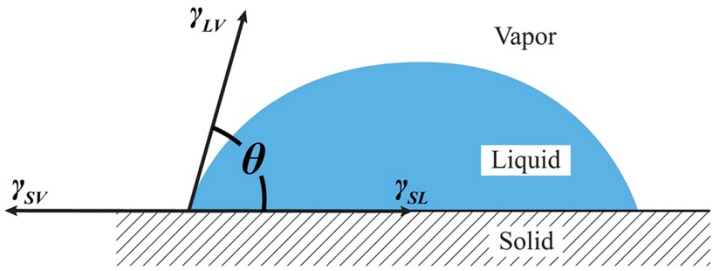

Fig. 2.8. Young's equilibrium contact angle

Since r is always equal or greater than 1 for the textured surface, rough surface will have higher level of wettability when the chemical nature of the flat surface is hydrophilic ($\theta < 90°$). On the other hand, a rough surface can become more hydrophobic when the flat surface is naturally hydrophobic ($\theta > 90°$). The Wenzel's equation can be applied if the liquid droplet fills in the valleys of the texture. This wetting state is known as Wenzel state, as shown in **Fig. 2.9**.

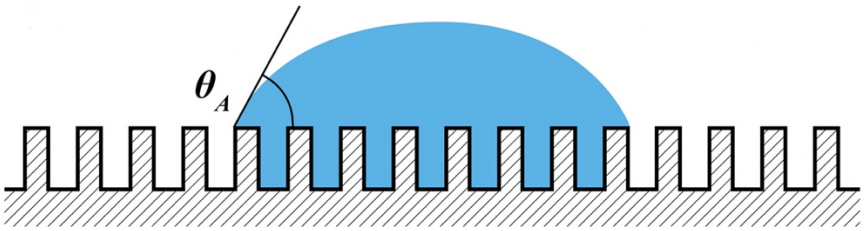

Fig. 2.9. Wenzel wetting state of a rough surface

It has been reported that surfaces with proper texture can become superhydrophobic and superhydrophilic (superwetting), when water CA is larger than 150° and smaller than 10°, respectively [76][77][78][79]. However, these results are related to how the droplet spreads/sits on rough profile contours. The superhydrophobic surface state has been extensively studied due to the need for water repellant materials. Various fabrication techniques have successfully produced

superhydrophobic surfaces, such as photolithography, laser texturing, and plasma processing [80]. On the other hand, literature reports on superhydrophilic surfaces are quite limited [71].

2.6. Surface free energy and cell adhesion

Materials or substances are formed by the interactions or bonds of atoms. Within the bulk of a material, atoms are generally stable and have a balanced set of interactions or bonds. In contrast, the atoms on a surface have an unbalanced set of interactions due to the absent of their neighbor atoms, broken bonds. Thus, these atoms on the surface have an excess internal energy compared to the atoms in the bulk and the excess energy is considered as surface free energy, in short surface energy. Surface energy affects activity of cells, such as protein adsorption and cell adhesion. Cell adhesion is important for cell sensing, cell regulation, cell proliferation, organ formation, and tissue maintenance [81][82]. It has been reported that surface with high surface free energy showed improvement of cell adhesion and spreading, while that with low surface free energy can inhibit cell behavior [83][84][85]. The mechanism behind this is still not fully understood.

The amount of surface energy depends strongly on the atomic bonding force and number of broken bonds, i.e., surface energy will be higher when the atoms have strong interactions and the surface is parallel to a high-index crystal plane. Surface energy can be described by Gibb's free energy as follows [86]:

$$G = G_0 + A\gamma \qquad (2\text{-}11)$$

Where G is the free energy of a system containing an interface of area A, G_0 is the free energy of the system, γ is the surface energy or the excess free energy from the broken bonds on a surface.

The surface energy can also be determined indirectly by CA measurements, which is more convenient. Various kinds of known surface tension liquid droplets, such as water and diiodomethane, are used to measure CA. Then the CA values will be used as parameters for surface energy calculation by a suitable model. There are a lot of surface free energy calculation models, however most of them are based on Young's equation, equation (2-9). Generally, a surface with high surface energy will have low CA of droplets or good wettability. This is due to the surface can form strong bonds, the interaction of liquid droplet with the surface will minimize the free energy of the system. Thus, the liquid is willing to break bulk bonding and spreading on the surface. The following equations are some examples for surface energy calculation.

2.6.1. Dupre's equation

This model can be used to relate interfacial tension and the interactions between the solid and liquid by describing the work of adhesion, W_{SL}. The work of adhesion represents the work that must be done to separate the two phases or the energy released in wetting of a surface. Dupre's equation is shown below:

$$\gamma_{SL} = \gamma_{LV} + \gamma_{SV} - W_{SL} \qquad (2\text{-}12)$$

When combining equation (2-12) with Young's equation (2-9), giving Young – Dupre equation which is one of the basic forms used in surface energy calculation. The Young – Dupre equation is as followed [87]:

$$W_{SL} = \gamma_{LV}(1 + \cos\theta) \quad (2\text{-}13)$$

2.6.2. Zisman Model

This model assumes that the surface energy of a solid is equal to the maximum surface tension liquid that will give a contact angle of 0°. This assumption is known as the critical surface tension. The contact angle on the surface for a series of liquid droplets is plotted versus surface tension. Then the surface energy of the solid can be extrapolated from the plot, as shown in **Fig. 2.10** [74][88]. The $\cos\theta$ is plotted against surface tension. The maximum surface tension that achieves θ = 0° is equal to surface energy. Nonetheless, The Zisman model is only suitable for non-polar surface since it ignores the impact of polar interactions.

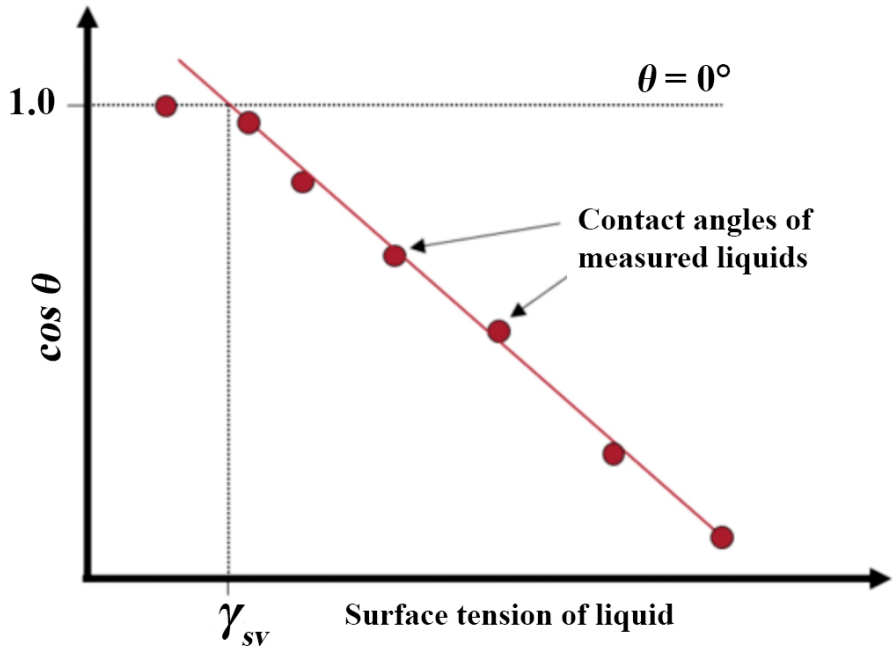

Fig. 2.10. Zisman plot

2.6.3. Owens – Wendt – Rabel & Kaelble Model

The Owens – Wendt – Rabel & Kaelble (OWRK) model requires two known polar dispersive and polar interactions liquids to determine surface energy. The most common used liquids are water and diiodomethane. The OWRK model is described in equation (2-14) and suitable for polar surfaces [89].

$$\frac{\gamma_{LV}(\cos\theta+1)}{2\left(\sqrt{\gamma_{LV}^{D}}\right)} = \left(\sqrt{\gamma_{SV}^{P}}\right)\frac{\sqrt{\gamma_{LV}^{P}}}{\sqrt{\gamma_{LV}^{D}}} + \sqrt{\gamma_{SV}^{D}} \qquad (2\text{-}14)$$

Where γ_{SV}^{P} and γ_{SV}^{D} are the polar and dispersive components of the surface energy of the solid, respectively. The γ_{LV}^{P} and γ_{LV}^{D} are the polar and dispersive components of the surface tension of the liquid, respectively [90].

Chapter 3 Experimental methods

3.1. Materials

Pure Ti (commercially pure Ti, Grade 2) sheets, 1 x 45 mm^2 and 1 mm thick, were used as substrates. The substrates were ground by silicon carbide papers down to 1000 grit as the last step and then masked to have a working surface area of about 1 cm^2. The samples were rinsed with acetone followed by ultrasonic cleaning in methanol for 15 minutes and ultrasonic cleaning in DI water for 15 minutes. These steps were followed for samples before and after their profiling process by EPP to eliminate oil, dirt, and contamination before performing contact angle measurements.

3.2. Electrolytic plasma processing

In this study, the Ti substrates were divided into three groups, which are the as-polished, plasma electrolytic saturation (PES) treated, plasma electrolytic oxidation (PEO) treated. The PES utilized cathodic reaction while the latter utilized anodic reaction. The two techniques performed in a different electrolyte and apparatus.

3.2.1. Plasma electrolytic saturation

Prior to actual PES, the entire voltage – current density response (*V-i*) was established in a 10 wt.% $NaHCO_3$ electrolyte to identify the Kellog's region, where the plasma envelope was stable. **Fig. 3.1** represents the full *V-i* response of the setup used in this study. The current density variation was plotted versus the applied potential. Based on the full *V-i* response in **Fig. 3.1**, the

Kellog's region was determined to be in the range of 90 – 110 V with a prevailing current density of ~3 A/cm^2.

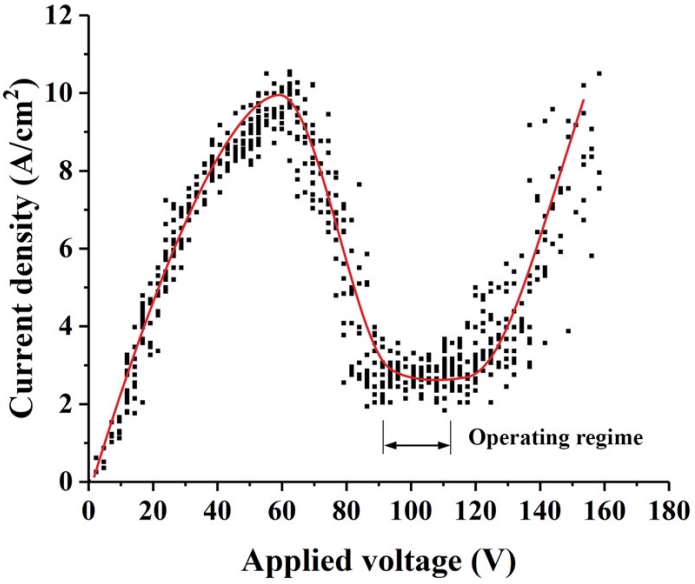

Fig. 3.1. Full PES *V-I* response of pure Ti in 10 wt.% $NaHCO_3$

PES was performed under the cathodic regime by controlling the input voltage using a DC power supply (SGA 600/17 DC, Sorensen, USA). A schematic drawing of the EPP system is shown in **Fig. 3.2**. Perforated graphite was used as the counter electrode (anode). DI water containing 10 wt.% of $NaHCO_3$ (99%, Alfa Aesar, USA) was used as the electrolyte with a pH 8.35. The electrolyte temperature was maintained at 75 °C. During the process, the electrolyte was circulated from a reservoir at a flow rate of 2 liters/min and supplied through the perforated counter electrode onto the surface of the Ti sample. The separation distance between the counter electrode and the substrate was 5 mm. The plasma processing was conducted at 105 V for different processing times; 30 s, 60 s, 90 s, 120 s, and 150 s. Duplication samples were processed at each processing time to confirm the reproducibility of the process.

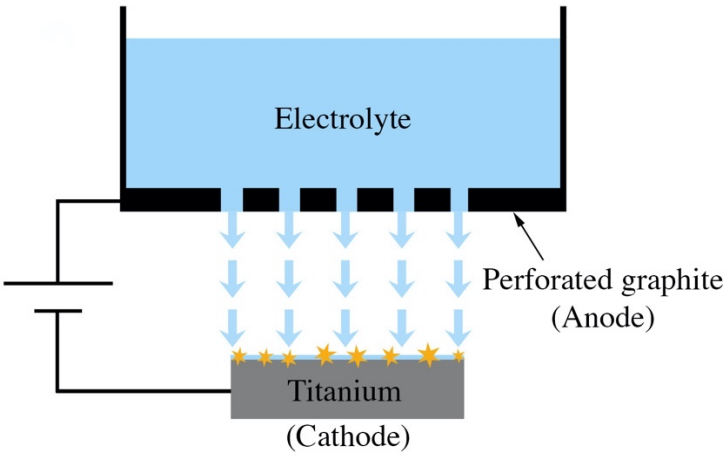

Fig. 3.2. Schematic drawing of the PES unit

3.2.2. Plasma electrolytic oxidation

A direct current power supply (SGA 600/17 DC, Sorensen, USA) was used as a power source. The PEO was done in a 800 mL double walled beaker and the temperature was kept below 30 °C by water coolant. The Ti anode was immersed in the center of the electrolytic cell and surrounded by a cylindrical stainless steel plate cathode. The coatings were prepared in 0.1 M KOH and 0.017 M $K_4P_2O_7$ electrolyte at pH = 12.7 and conductivity of 125 mS/cm at difference current density, i.e., 50, 100, and 150 mA/cm^2. The presence of the KOH in the electrolyte is beneficial for developing uniform coatings. The applied current densities were kept constant during each PEO treatment. Preliminary experiments were performed to observe the breakdown voltage and arcing regime of the setup in this study. After the PEO process reached breakdown voltage (~220 V), the Ti substrates were further treated for 90 and 270 s. The maximum treatment duration was set at 270 s to avoid detrimental effects from severe arcing.

3.3. Surface characterizations

3.3.1. Surface morphology and chemical composition

Scanning electron microscopy (SEM) in conjunction with energy dispersive X-ray spectroscopy (EDS) (S-3000N, Hitachi, Japan) was used to examine the surface morphology and the chemical composition of the Ti samples before and after EPP processing. The acceleration voltage during EDS analysis was kept constant at 15 kV, to minimize the excitation volume.

3.3.2. Surface profile characteristics

An optical profilometer (Wyko NT9100, Veeco Instruments Inc., USA) was used to measure the surface roughness (*Sa*) and other surface characteristics such as the average of maximum height of the hills to valleys (*Sz*), the asymmetry of surface about the mean plane (*Ssk*), and the ratio of the actual surface area to projected area (*r*). The samples were scanned at 7 different areas to cover the surface and extreme values were eliminated before determining average values.

3.3.3. Contact angle measurement and surface energy calculation

A simple sessile drop system was used to measure the CA on the Ti surface before and after the EPP profiling process. Briefly, an electronic pipet was used to drop DI water droplets, 5 μL, on the sample surface. An optical microscope was used to capture the images of the droplets on the Ti surface. Then, Adobe Photoshop was used to process the images into black and white. Finally, CA values were acquired in ImageJ software (NIH) by Dropsnake analysis plugin. The CA measurements were repeated for 7 times at different locations on each sample and average values are reported.

To calculate the surface energy of the Ti surfaces, the CA of the water and the diiodomethane droplets were measured using the sessile drop method. The CA values were then used as parameters to determine the surface energy using the OWRK model, Eq. (2-13).

3.4. *In-vitro* studies

To study the effect of Ti surface treatment on its bioactivity, cell free *in-vitro* studies were performed on the treated samples compared to the untreated Ti samples. Alpha modified minimum essential medium (α-MEM) (Gibco 12571063, USA) was used as an alternative solution to the conventional simulated body fluid (SBF) in this study [91][92][93]. α-MEM is an appropriate medium for bone cell culture studies; its ions concentration, pH, and amino acids and vitamins make it similar to that of human blood plasma. The ions concentration (mM) of the α-MEM are as followed Na^{+}= 144.4, K^{+}= 5.3, Mg^{2+}= 0.8, Ca^{2+}= 1.8, Cl^{-}= 126.2, HCO^{3-}= 26.2, HPO_4^{2-}= 1.0, SO_4^{2-} = 0.8 and pH = 7.4. The α-MEM has been reported to be used as an alternative SBF to evaluate HA ($Ca_{10}(PO_4)_6(OH)_2$) precipitation in *in-vitro* studies [91]. α-MEM gives similar precipitation driving forces and nucleation rates as found by Hank's balanced salt solution [92]. Untreated Ti (polished 1000 grits) samples were used as a control group. For the PES treated samples, *in-vitro* study was performed only on the 150 s treated samples, since they exhibited the lowest contact angle. Untreated, PES and PEO treated Ti samples were immersed in α-MEM and kept incubated at 37 °C for 7, 14, and 21 days. The test solution was changed every 48 hours to maintain ion concentration levels and pH. After completion, the samples were then rinsed with phosphate buffered saline and then dried under air environment for further characterizations.

X-ray diffraction (XRD) (D8, Bruker, USA) was used to identify the precipitation of HA. The θ-2θ scans were performed by Cu K_α radiation (λ = 1.5418 Å) with step size of 0.01° and dwell time of 3 s/step. Fourier transform infrared spectroscopy (FTIR) (Thermo Nicolet 6700 ATR, Thermo Electron Corporation, USA) was also used to confirm the presence of hydroxyl and phosphate groups in HA. Surface morphology and chemical composition were evaluated by high resolution (HR) SEM in conjunction with EDS (S-3000N and S-4800, Hitachi, Japan).

After studying the surface bioactivity using cell free media, *in-vitro* studies using murine calvarial MC3T3-E1 pre-osteoblast and human mesenchymal stem cells were performed to further investigate the bioactivity and the cellular behavior on the PES treated 150 s and PEO treated surface, respectively, compared to the untreated Ti. The osteoblast cells are responsible for bone deposition of bone matrix and for osteoclasts regulation [94]. They are widely used to assess the bioactivity of a biomaterial surface. For the PES treated Ti, MC3T3-E1 cells (American Type Cell Culture Inc., Manassas, VA) were cultured using α-MEM supplemented with 10% fetal bovine serum and 1% penicillin/ streptomycin until 75% confluence (passage 14-15). Then, cells were seeded on the different Ti surfaces using 24 well-plates and n=3 for each group for 24 and 48 hours. For the PEO treated Ti, male-human mesenchymal stem cells (MSCs) were carried out to investigate the surface cytotoxicity and the cellular behavior on the PEO treated samples, n = 3 for each group. MSCs are typically used in the field of tissue engineering applications due to their ability for self-renewal, capability to proliferate and then differentiate into different cell-type such as bone [95,96], ligament [97], adipose [98], cartilage [99,100], and muscle [101] tissues based on the type of conditioned cell culture media being used. Male human bone marrow MSCs were obtained from Lonza (Lonza Walkersville Inc., MD, USA) and cultured in MSCGM BulletKit™

(Lonza, PT-3238 & PT-4105) specific growth medium until 75% confluence (passage 2). The cells were seeded on the PEO treated samples for 24 and 72 hrs.

After each time point, MTS assay was performed using CellTiter 96® AQueous One Solution Cell Proliferation Assay kit (Promega, Madison, WI, USA). MTS reagent was added directly to each well, the plate was wrapped with Al foil to be protected from the light, and the plate was incubated for 2 hours. Then, the optical density (OD) readings were recorded using microplate reader (SpectraMax® i3, Molecular Devices, CA, USA) at 490 nm. Furthermore, live/dead assay using Invitrogen LIVE/DEAD Viability/Cytotoxicity Kit (Thermo Fischer Scientific Inc., Waltham, MA, USA) was performed. Green stained live cells were captured as fluorescent images using a DMi8 inverted Leica microscope (Leica Microsystems Inc., IL, USA). Five images were taken for each sample and n=3 samples for each group. Fluorescent images were further used for quantitative analysis to count the exact number of live cells on each Ti surface using ImageJ software (NIH). OriginPro 8.5 software was used for all graphs and statistical analysis, and one-way ANOVA followed by Tukey's post hoc was used between group comparisons. Statistical significance was considered when $p < 0.05$ represented as (*), $p < 0.01$ as (**), and (***) for $p < 0.001$.

Chapter 4 Results and discussion

4.1. Plasma electrolytic saturation

4.1.1. Chemical composition and surface morphology

EDS analysis was conducted on all PES processed samples. **Figs. 4.1a-b** show EDS spectrums of the untreated and EPP treated Ti, respectively. The untreated Ti surface contained carbon 8.4 at.% (± 1.0 at.%) and the rest was Ti. The untreated Ti surface may absorb carbon from ubiquitous hydrocarbon in air, solution containing organic contaminations, or the previous polishing process. For the PES treated Ti, the EDS analysis revealed a small amount of carbon, 1.7 at.% (± 0.5 at.%). The oxygen content on the PES treated Ti ranged from 7 – 10 at.%. The PES treatment eliminated surface contamination, as seen from the decreased carbon content. It's good to note that the remaining of carbon found on the PES treated may come from the carbon residual that already presents in the SEM chamber. Plasma processing creates a fresh and effectively clean metal surface that is highly reactive. Thus, oxygen in the air reacts with the treated Ti surface and a very thin TiO_2 layer is built up. Cionea has reported that the top layer of PES treated Ti has ultrafine grain (10 – 40 nm) with the depth of about 100 nm due to the repeated melting and freezing cycles during the plasma processing [59]. Thus, this thin TiO_2 layer is responsible for the small amount of oxygen content found on the PES treated Ti. The TiO_2 is capable of forming hydroxyl groups on its surface, which may help decreasing the contact angle of water droplets [102].

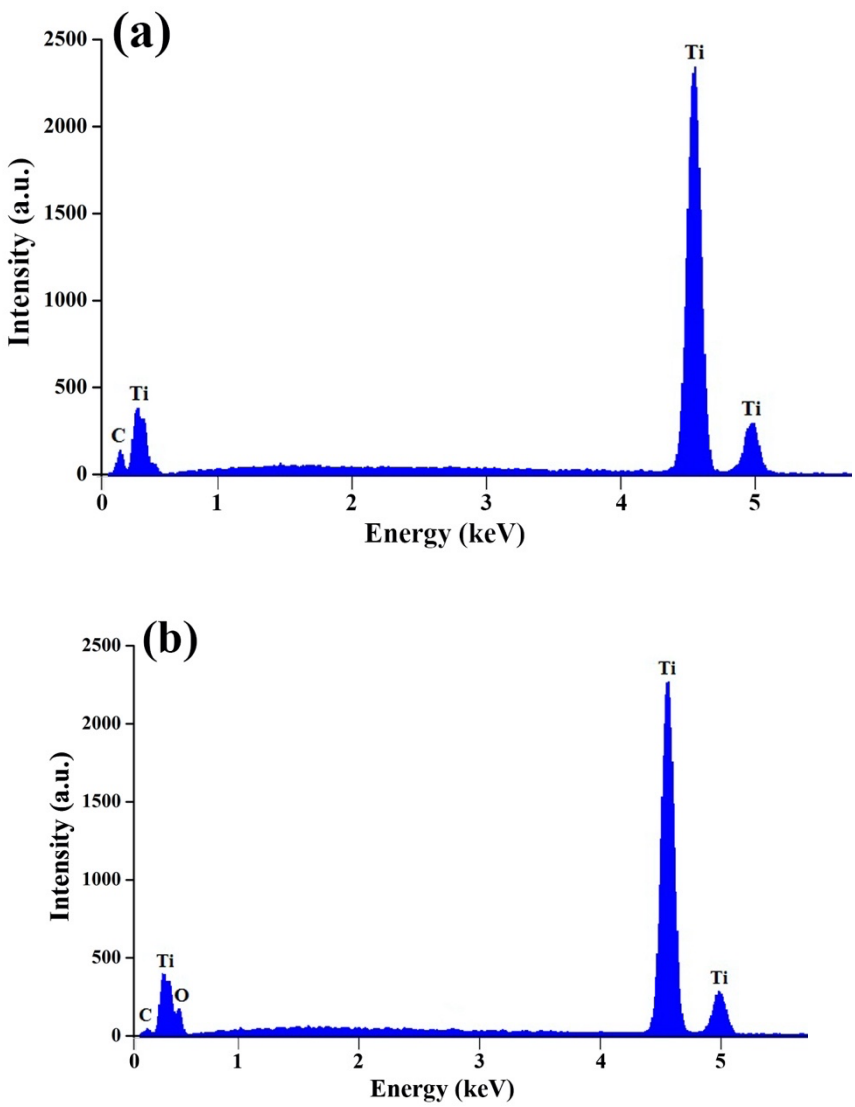

Fig. 4.1. EDS spectrum of **(a)** untreated, **(b)** PES treated for 150 s

Scanning electron micrographs of the PES profiled Ti at different processing time are shown in **Figs. 4.2**. Characteristic hills, valleys, and crater-like features appear across the surface of the PES profiled Ti. These features were a result of local surface melting by high temperature discharge created by PES. Then, the collapse of high energetic plasma at the vicinity of the titanium surface produced shock waves. Subsequently, fast solidification takes place due to the presence of aqueous electrolyte [10][12]. Elias et al. and Guéhennec et al. have reported that crater-like and

pore features on the surface exhibit higher wettability and removal torque after *in-vitro* and *in-vivo* tests, compared to other rough surfaces without these features [103][104].

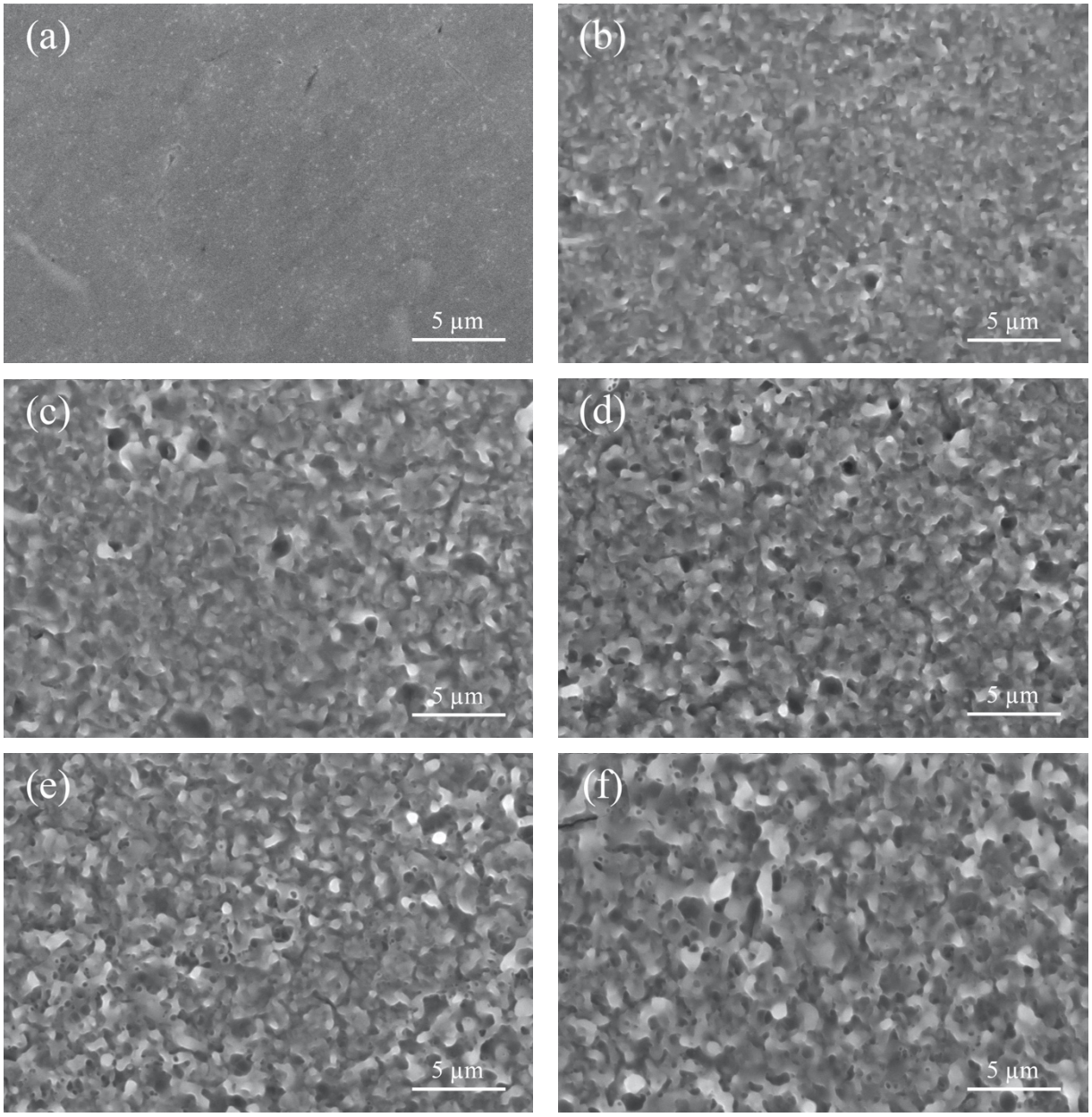

Fig. 4.2. Scanning electron micrograph of PES textured Ti **(a)** untreated; after processing for **(b)** 30 s, **(c)** 60 s, **(d)** 90 s, **(e)** 120 s, and **(f)** 150 s

The SEM images also reveal that the size and number of crater-like features were increased by increasing processing time. The processed surfaces exhibited complex texture such as

protruding and undercutting features for plasma processing at or longer than 90 s. These features are greatly increasing the surface area of the PES profiled Ti. Furthermore, there were submicrometer (80 – 350 nm in diameter) pores embedded in the protruding features. The high surface area and the presence of pores can increase the wettability of the surface by letting the liquid droplet imbibe through those pores. Thus, the wetting state may not solely follow the Wenzel state, where the surface is dry ahead of the contact line, but rather exhibiting film state, where the texture is filled with a liquid film [105]. The condition for droplet imbibition will be discussed in the following section.

4.1.2. Wettability and surface roughness

The wettability of the surface was investigated by CA measurements. An example of a water droplet on an untreated and plasma processed Ti surface is shown in **Fig. 4.3a** and **Fig. 4.3b**, respectively. The CA variation of the Ti samples at different processing times is shown in **Fig. 4.4**. The CA for the unprocessed sample (denoted as 0 s) is also included for comparison. The results revealed that the untreated Ti was hydrophilic with a CA of 38.7°. After plasma processing, the CA decreased significantly (~82%) exhibiting only a small decrease with increasing processing time. It is important to note that even a PES treatment for 30 s produced a surface profile, **Fig. 4.2b**, with a very low CA (~9°). Thus, the wettability of the Ti samples was increased and became superhydrophilic after subjected to PES profiling. The highest wettability (average AC of 5.4°) was observed for the profile produced after 150 s of processing, **Fig. 4.2f**.

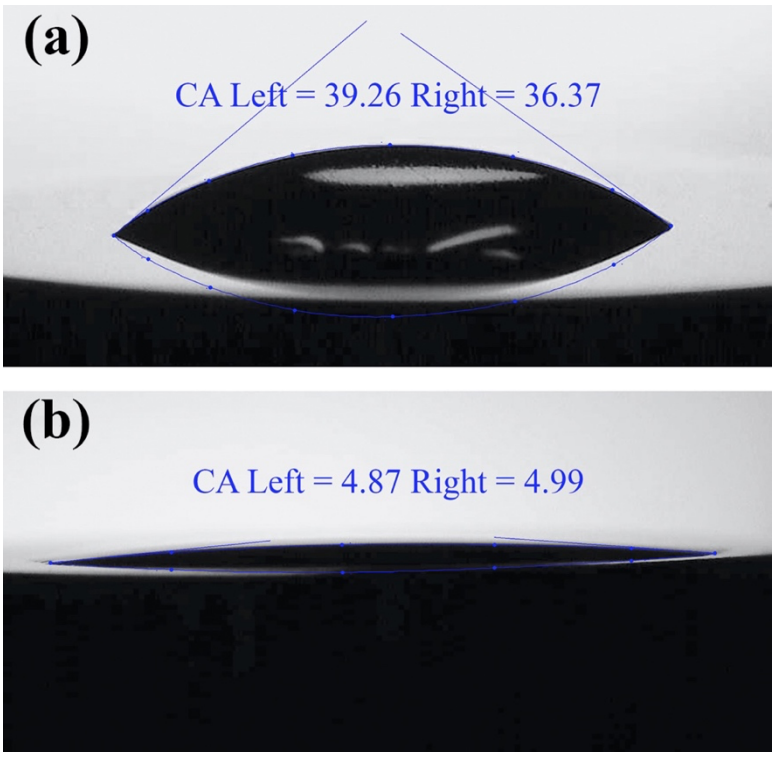

Fig. 4.3. Water droplet on titanium surface **(a)** untreated and **(b)** after PES for 150 s

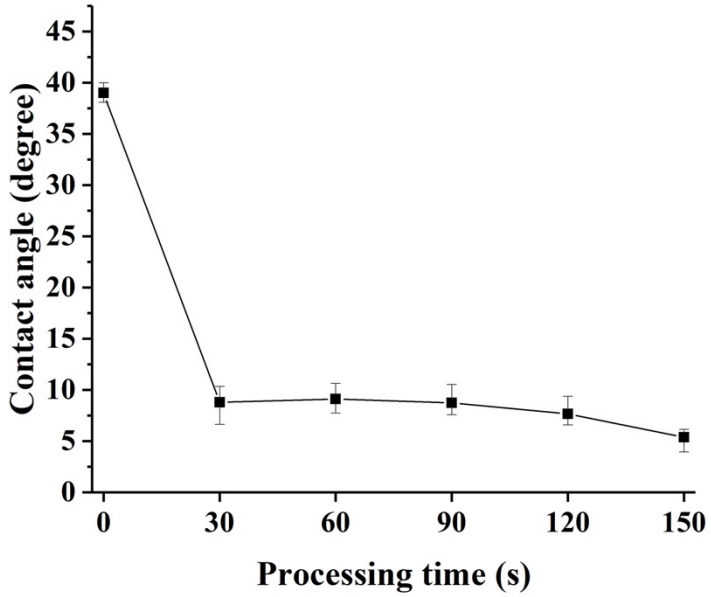

Fig. 4.4. Apparent contact angle as a function of processing time

The results of *Sa* and *Sz* versus processing time are shown in **Fig. 4.5** and **Fig. 4.6**, respectively. The results clearly show that increasing processing time resulted in an increase in roughness parameters. The trend of the increase of *Sa* is almost linear since longer processing time allows plasma processing to produce rough characteristic surface from numerous cycles of local melting and freezing events. Even a 30 s treatment produces a significant increase in *Sa* from 17 nm for the untreated surface to 87 nm. The highest surface roughness was achieved after processing for 150 s exhibiting a value of *Sa* 213 nm. It is important to note that the PES treatment produced a nanoscale roughness with the *Sa* parameter remaining at or below ~200 nm for all treatments. Gui et al. performed PES treatment (cleaning) on 304 stainless steel at different processing time and found a similar trend for the surface roughness, even though it has been analyzed in 2D (*Ra*) [106].

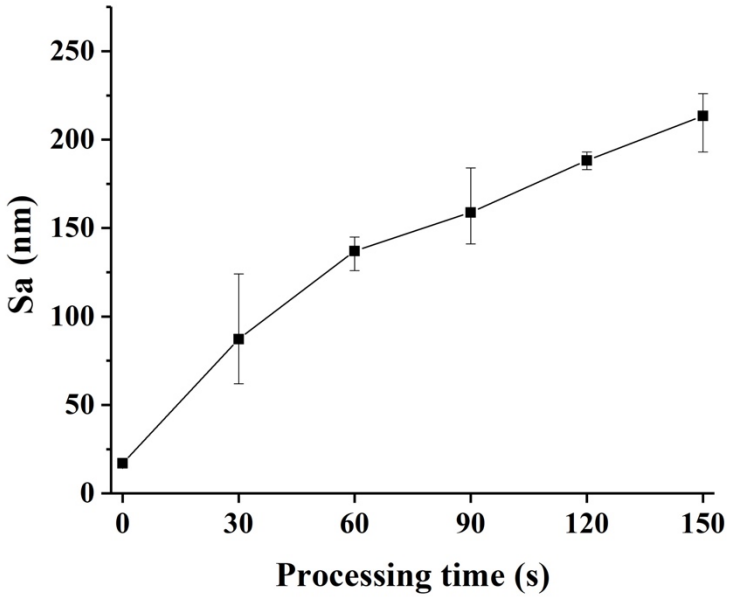

Fig. 4.5. Surface roughness (Sa) as a function of processing time

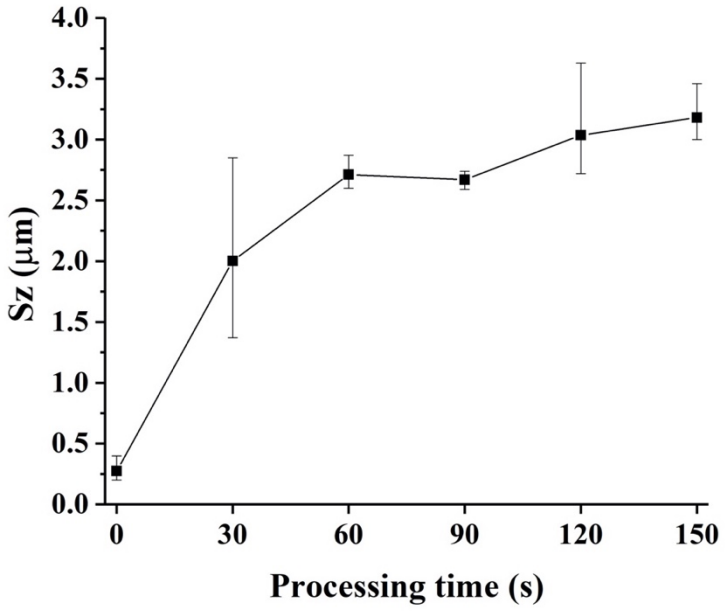

Fig. 4.6. Maximum height from hills to valleys (*Sz*) as a function of processing time

The results of *Sz* present the average variation of the distance between the top of the hill and bottom of the valley features with processing time. The trend of *Sz* with processing time exhibits a sharp increase initially and more of a plateau after 60 s. Furthermore, initially the variation was obviously high which was probably due to insufficient processing for such short duration. Beyond 60 s of treatment, *Sz* seems to stabilize at about 3 μm. Another surface roughness parameter obtained is *Ssk* that is used to evaluate the profile symmetry of the surface about the mean plane. The value of the *Ssk* can be negative, zero, or positive. The negative skew means the bulk of the material is above the mean plane where the positive skew is the opposite. This implies that the negative skew surface mostly comprises deep valleys rather than spikes. The zero skew means the surface is more symmetric [107]. In this study, the untreated sample had a negative skew as seen from the results in the **Fig. 4.7**. This is a result of the presence of scratches from the mechanical grinding process. However, the negative skewness has reduced after subjected to the PES profiling, moreover, it became closer to zero after PES profiling for 90 s and longer. This is

due to the effect by the fine plasma during PES producing a profile with higher *Ssk* uniformity. Thus, the PES has created a new texture on the Ti surface with comparatively equal amounts of spikes and valleys. Furthermore, the results revealed that a type of hierarchical profile was produced composed of ~3 μm spikes (2 μm< *Sz* <3 μm) separate by valleys with nanoscale roughness (100 nm< *Sa* <200 nm).

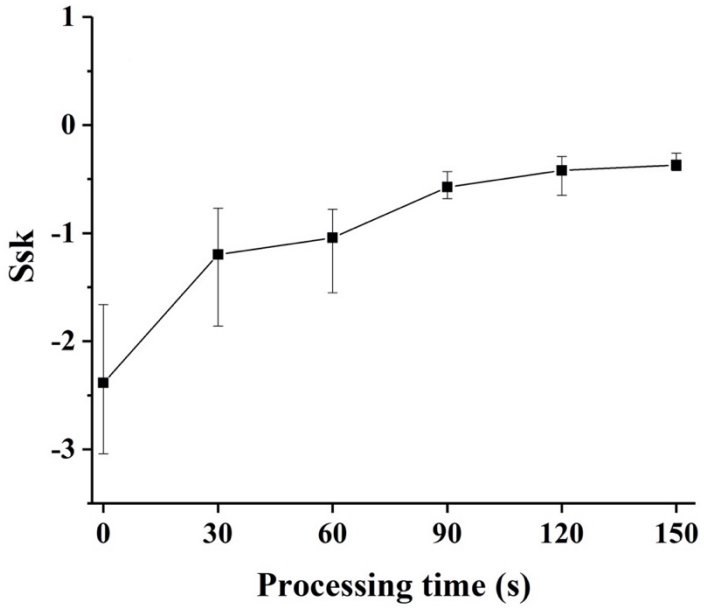

Fig. 4.7. Profile symmetry about mean plane (*Ssk*) as a function of processing time

4.1.3. Surface energy

The CA and surface tension components of the water and diiodomethane droplets are listed in **Table 4.1**. Plugging in the CA, γ_{LV}^{d}, γ_{LV}^{p}, and γ_{LV} value of the water and diiodomethane into Eq. (2-14) yielded two equations, then the γ_{SV}^{p} and γ_{SV}^{d} were solved. The surface energy is the summation of γ_{SV}^{p} and γ_{SV}^{d}. The CA of diiodomethane on the as-polished and PES treated surface was 31° and 18°, respectively. The as-polished Ti and the PES treated for 150 s had the surface

energy of 61.62 mJ/m^2 and 75.2 mJ/m^2, respectively. The increasing of surface energy has been reported to be beneficial for protein adsorption and cell adhesion [83][84].

Table 4.1. Contact angle values and surface energy components of the water and diiodomethane droplets [89]

Liquid Droplets	γ_{LV}^{d} (mJ/m^2)	γ_{LV}^{p} (mJ/m^2)	γ_{LV} (mJ/m^2)	CA (degrees)	
				As-polished	PES 150 s
Water	21.8	51.0	72.8	39	5
Diiodomethane	49.5	1.3	50.8	31	18

4.1.4. Superhydrophilicity of PES profiled surfaces

Prior to discussing how superhydrophilicity was induced on PES profiled surfaces, it is beneficial to give a brief explanation on how superhydrophobic surface is developed since it is the opposite phenomenon. A textured solid surface can become superhydrophobic when the liquid droplet rests between spikes or protrusions. Air must be trapped in the cavities under the liquid droplet. This follows the Cassie-Baxter wetting state as shown in **Fig. 4.8a** [108]. However, the trapping of air is metastable since the liquid droplet will eventually wet the solid surface in the cavity, transition to Wenzel state, due to lower energy state of their interactions.

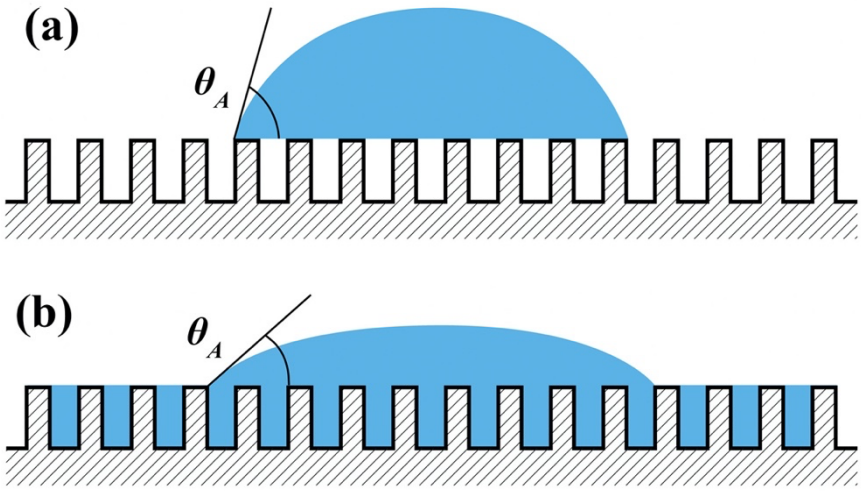

Fig. 4.8. Wetting of a droplet on rough surface **(a)** Cassie-Baxter state and **(b)** film state

Bico et al. applied Young's and Wenzel's equations and reported that the condition for the stability of the liquid droplet on air cavities followed equation (4-1):

$$\cos\theta < \frac{\varphi - 1}{r - \varphi} \qquad (4\text{-}1)$$

where θ, *r, and* φ are Young's contact angle on flat surface, the ratio of the actual surface area to the projected one, and the fraction of solid surface remaining dry, respectively [105].

For the superhydrophilic case, the liquid drop must be *hemi-wicking*, which is the opposite to the pinning of the droplet for the case of superhydrophobic. *Hemi-wicking* is the mechanism that the liquid droplet is intermediate between imbibition and spreading into the cavities of the textured surface. This wetting state has been proposed as film state. **Fig. 4.8b** is the schematic drawing of a liquid droplet on a textured surface representing the film wetting state. Hence, this gives the prerequisite conditions for superhydrophilic surface as follows [105][109]:

$$\cos\theta > \frac{1 - \varphi}{r - \varphi}, \quad \theta < \theta_c \qquad \text{with} \qquad \cos\theta_c = \frac{1 - \varphi}{r - \varphi} \qquad (4\text{-}2)$$

where θ_c is the critical contact angle.

Table 4.1 presents the *r* and φ measurements for all PES processed samples. The surface profiling results revealed that the *r* value increased significantly by increasing processing time in the PES profiling process. The untreated sample had an *r* value of 1.1, then increased to 12.4 after subjected to PES profiling process for only 30 s. Moreover, the *r* value went up to 88.6 after processing for 150 s. This was consistent with the *Sa* and *Sz* results, since rougher surfaces provided larger surface area [110]. In view of equation (4-2), when *r* is comparatively large, the condition for *hemi-wicking* is favored. Thus, the surface of Ti has turned to superhydrophilic after the PES profiling process.

Table 4.2. Values of the ratio of the actual surface area to the projected area (*r*) and fractal area of solid surface remaining dry (φ) as a function of processing time

Parameter	Processing time (s)					
	0	30	60	90	120	150
r	1.10	12.40	23.20	41.20	60.40	88.60
Standard deviation	0.03	9.04	5.93	9.86	14.89	19.79
φ	0	0.031	0.036	0.041	0.042	0.046
Standard deviation	0	0.006	0.004	0.006	0.005	0.004

Representative contour spectral and 2D surface line profiles as a function of treatment time are shown in **Figs. 4.9**. They were used to evaluate and calculate the φ values. As seen from the SEM images in **Figs. 4.2**, the geometry on top of the features of the PES profiled surface was nonuniform since the protrusions were randomly created by the collapse of the plasma. The contour spectral images are representing the distribution of the height over the scanned area. They show that for the clear majority of hills, their height on the profiled surface is at least in the range of about 0.4 μm. In view of equation (4), in a surface with a high value of *r* ($r > 5$) and naturally hydrophilic

(apparent contact angle $\theta < 75°$), water droplets will imbibe and spread to fill up between these protrusions and valleys. This results in wetting of the surface regardless of φ values. The summation of the area on top of each spike above the droplets is the φ value. However, the PES produced features with a variation in height and it is hard to precisely calculate their surface area on the tip of them. Thus, the portion of spikes at and above 0.4 μm was considered as the surface remaining dry since most asperities and valleys are lying below them.

The cross-sectional areas at the height of 0.4 μm and above will be representing the surface remaining dry area of the asperities. These areas appear in saturated red in the contour spectral images of **Figs. 4.9**. ImageJ software was used to determine the sum of the areas in saturated red and extract the φ values that are reported in **Table 4.1**. The PES profiled samples had φ values of 3.1%, 3.6%, 4.1%, 4.2% and 4.6% after processing for 30 s, 60 s, 90 s, 120 s and 150 s, respectively. The 2D surface line results provided additional evidence that the longer processing time produces a higher number of tall spikes and deep valleys. It is important to note that the proposed criterion for surface remaining dry could possibly overestimate the φ values. Nevertheless, these surfaces have sufficiently large r ($r > 12$) and their apparent contact angle on flat surface is small enough ($\theta = 38.7°$) to be able to neglect possible overestimation of φ values.

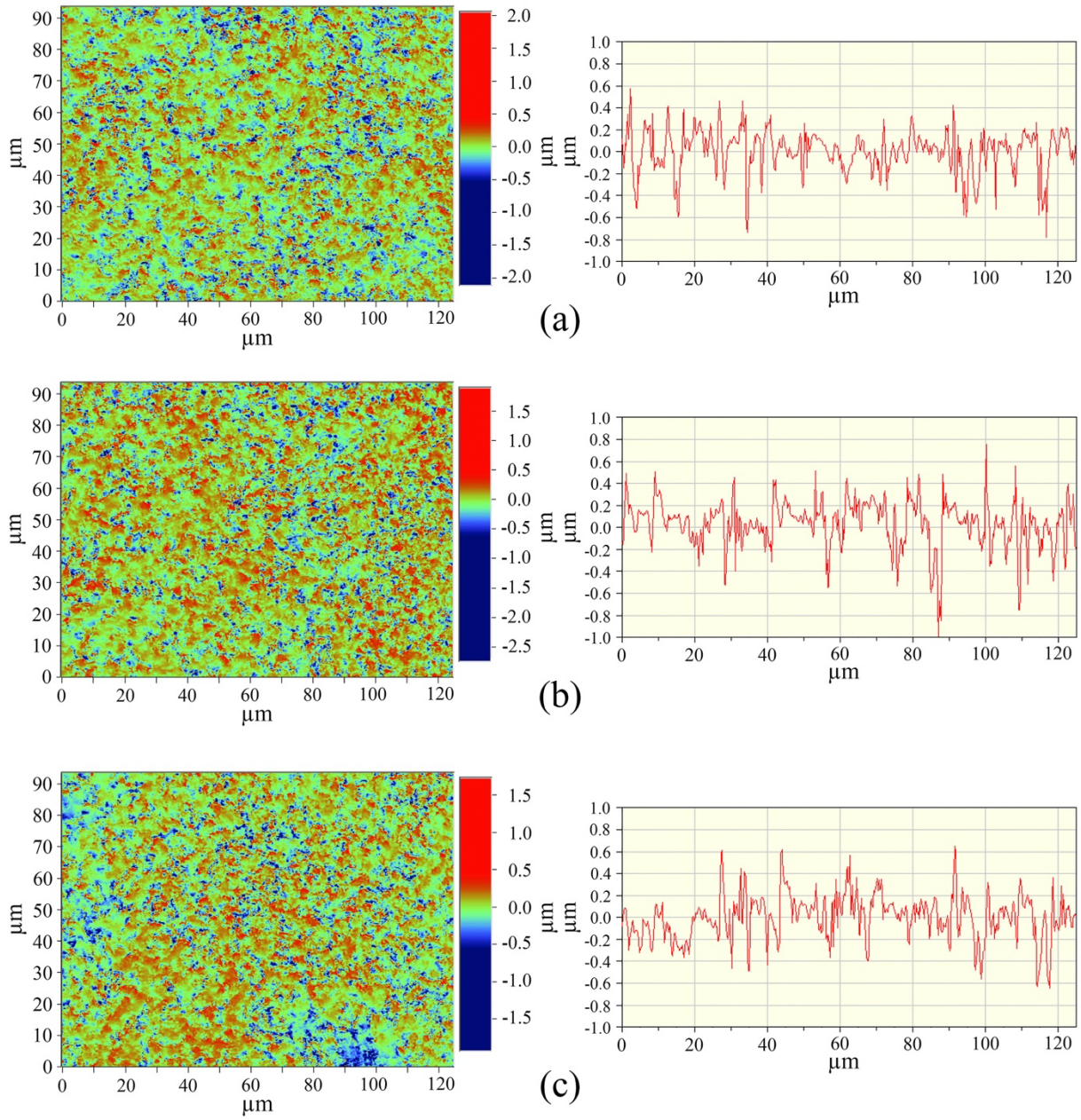

Fig. 4.9. Contour spectral images (left) and 2D line scans (right) of PES profiles after treated for **(a)** 30 s, and **(b)** 60 s, **(c)** 90 s **(d)** 120 s, and **(e)** 150 s

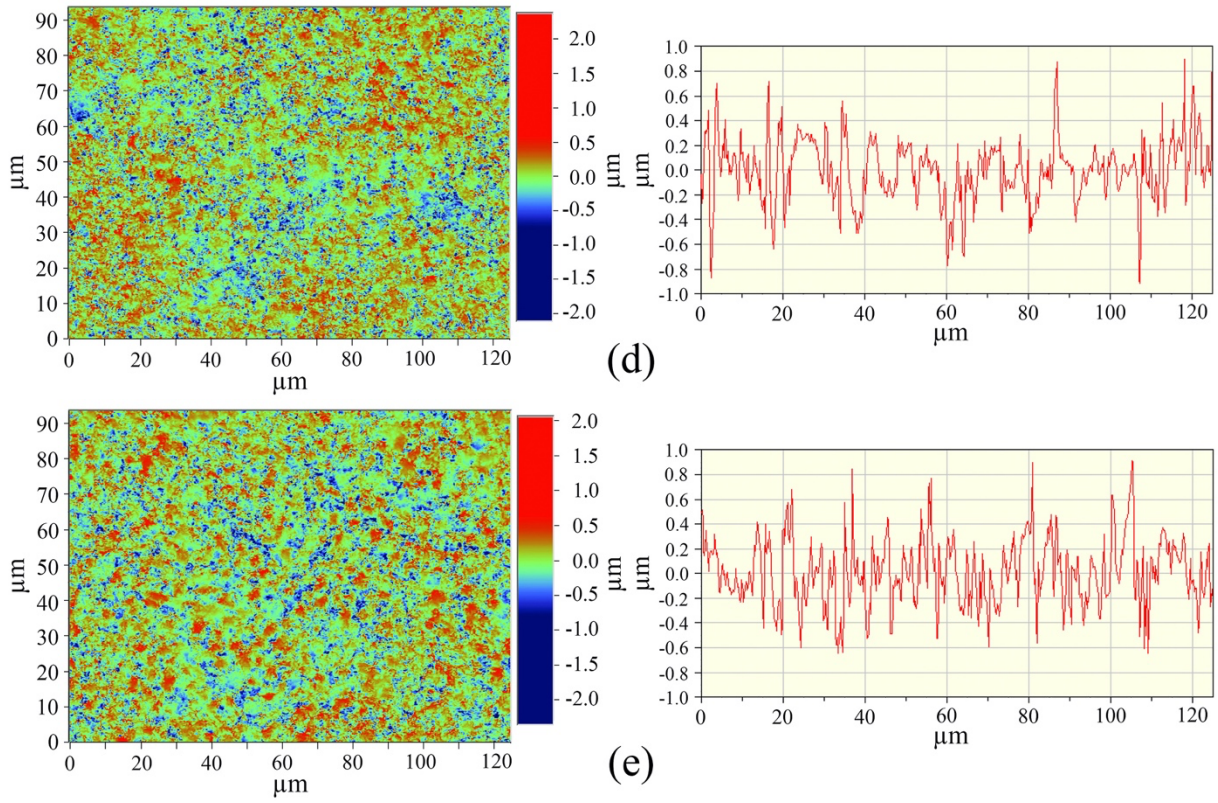

Fig. 4.9. (Cont.)

Figs. 4.10 present the distribution of the area of the solid surface remaining dry for each processing time. The results clearly show that prolonging processing time produced a larger number of smaller size spikes scattered across the surface. The increase in number of small spikes results in a substantial increase in *r*, which is favorable for inducing the *hemi-wicking* mechanism and, finally, lower CA of the droplets. In superhydrophilic and superhydrophobic surface design, line density (i.e., spike or hill density) and asperity height are one of the most important parameters to be considered [111]. The line density in the present study can be determined by dividing the scanned area shown in **Figs. 4.9** with the total number of spikes taller than 4 µm from **Figs. 4.10**.

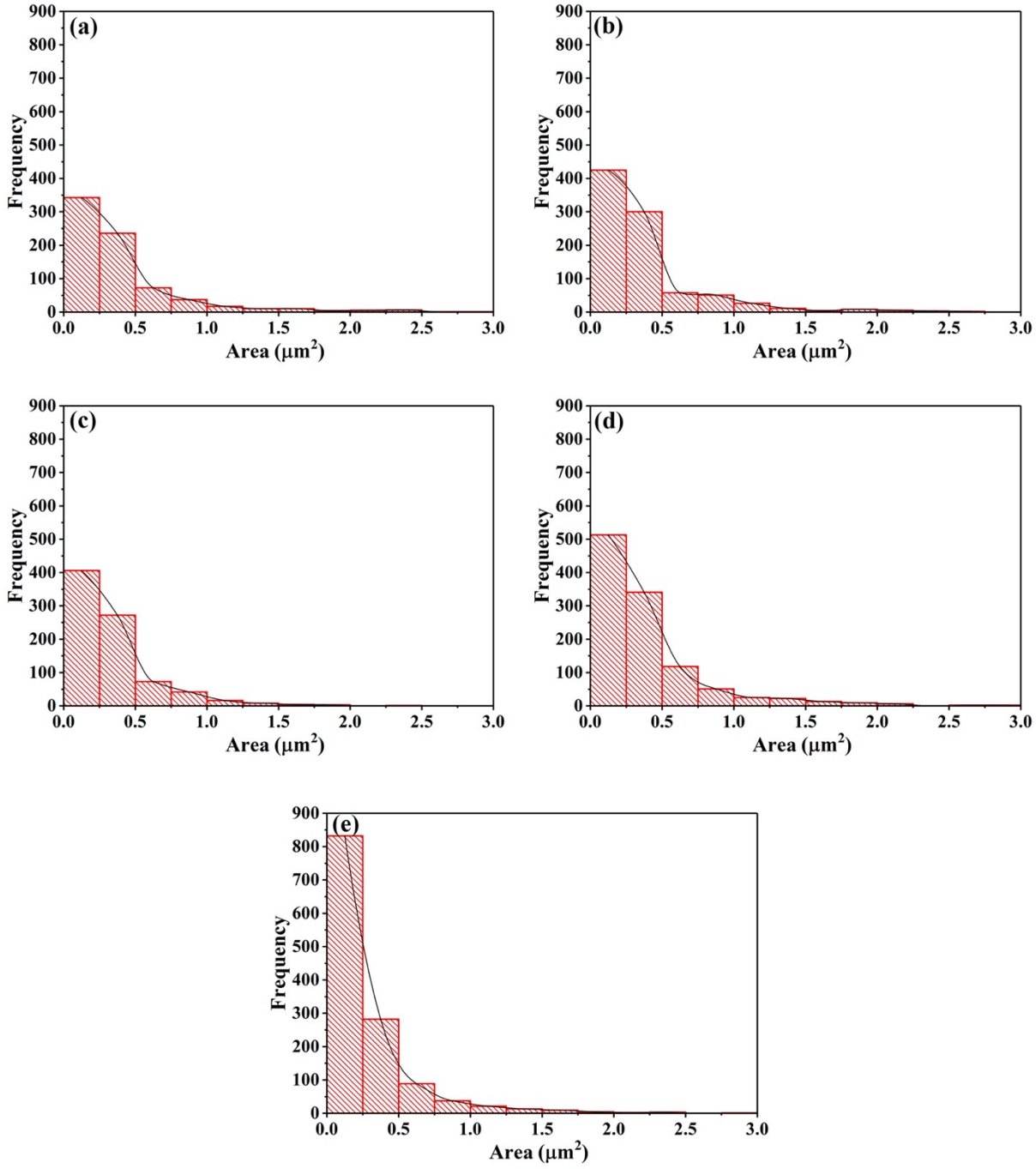

Fig. 4.10. Distribution of cross-sectional area of spikes with a height of at least 0.4 μm, representing surface remaining dry for a PES treatment of **(a)** 30 s, **(b)** 60 s, **(c)** 90 s, **(d)** 120 s, and **(e)** 150 s

For example, for a 150 s treatment, the results show that there is a spike taller than 0.4 μm in every 10 μm^2 of the profiled surface. Such a combination of spike line density and height is expected to be beneficial for the spread of droplets [112].

The critical CAs for the processed samples were calculated following equation (4-2). The apparent and critical CA for each processing time were plotted and shown in **Fig. 4.11**. As mentioned above, when the critical CA is larger than the apparent contact angle, superhydrophilicity will be achieved as a result of the *hemi-wicking*. It can be seen that the surface condition of the untreated sample yielded a critical CA of 24.0° which was smaller than the apparent CA, 38.6°. Thus, it was not able to induce superwetting of the surface. However, after PES profiling, the surfaces yielded critical CA values close to 90°. In other words, the textured created by PES profiling was able to induce superhydrophilicity on the titanium surface.

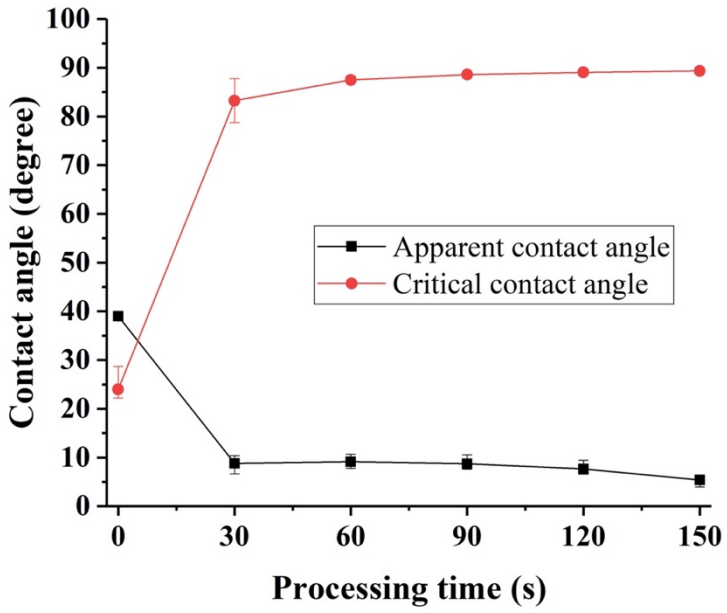

Fig. 4.11. Apparent and critical contact angle as a function of PES treatment duration

Thus far in this section, superwetting mechanism of the PES treated surface has been discussed based on its topography. Our findings showed that wettability mainly depends on *Sz* and *Ssk* (b0th exhibiting a plateau with processing time) and not much on *Sa* (increase in roughness). Another factor affecting wettability is the surface chemistry. As mentioned earlier, the PES produced clean surface with thin TiO_2 layer for all treated samples including the one processed for 30 s. The TiO_2 has been reported to be able to form hydroxyl groups, which may help decreasing the contact angle. However, this would happen when TiO_2 reacts with a liquid at physiological pH values and a certain thickness may be required [102]. Also, the EPP treated samples showed an insignificant amount of carbon contamination on their surface. It is known that a surface with less contamination possesses higher surface free energy [113][114]. Hence, it is readily to reduce its surface free energy by bonding with the water droplets that land on its surface. In addition, the PES profiling surfaces have such large *r* value that satisfying *hemi-wicking* mechanism. It can be concluded that the combinations of surface chemistry and topography yield superwetting characteristic on the PES treated Ti surface.

It is important to note that the PES profiled samples were not able to achieve complete wetting (i.e., CA of 0°). It is noted that Wenzel's equation suggests that rough surface satisfying $cos\theta > 1/r$, corresponding to $dE < 0$ can exhibit complete wetting [112][115]. However, this is not accomplished since the real surface can not completely imbibe the liquid droplet. In addition, superhydrophilic surface is sensitive to contamination as a result of its high surface energy. By exposing the surface to air environment, contamination from airborne can easily reduce the wettability of the surface [71][116]. Nevertheless, the present results show that PES is a promising profiling method to induce superhydrophilicity on titanium surfaces. This is particularly important

for titanium and its alloys since they are biocompatible and widely used materials for biomedical applications.

4.1.5. *In-vitro* study in cell free media

HR-SEM images, **Figs. 4.12**, represent the surface morphologies of Ti samples after immersion in α-MEM for 7, 14, and 21 days. It is clearly seen that both treated and untreated groups were able to induce calcium phosphate nucleation on their surface after 7 days of immersion. This is due to the α-MEM is metastable and supersaturated towards calcium phosphate crystals. It will eventually reduce its energy by forming calcium phosphate crystals when the time and temperature are suitable [117]. However, it can be clearly seen that the PES treated Ti surface showed a higher density of calcium phosphate deposition compared to that of the control group. The PES treated Ti has better hydrophilicity level and larger surface area due to its rougher profile compared to the untreated Ti. An increase of material surface area can lead to better protein adsorption and faster change of local α-MEM composition, thus, a faster calcium phosphate crystal formed on the surface [117][118]. Moreover, a solid surface with high surface energy will provide a better nucleation site for heterogeneous nucleation. Since its interfacial energy with calcium phosphate-nucleus is lower than that of nucleus-solution interface. Hence, calcium phosphate nucleates and grows faster on the PES treated Ti in α-MEM. The results of apatite coverage analyzed in ImageJ software, shown in **Figs. 4.13a-f**, also provide additional evidence that the PES treated Ti surface has higher nucleation rate as we can see from the percentage of apatite coverage. At day 7, the apatite coverage of the untreated and PES treated Ti was at 18.7% (± 2.1%) and 35.0% (± 2.6%), respectively. After immersion for 21 days, the apatite coverage increased to

33.0% (± 3.0%) and 72.3% (± 2.1%) for the untreated and PES treated, respectively. **Fig. 4.14** represents percentage of apatite coverage on the Ti substrates after immersion in α-MEM.

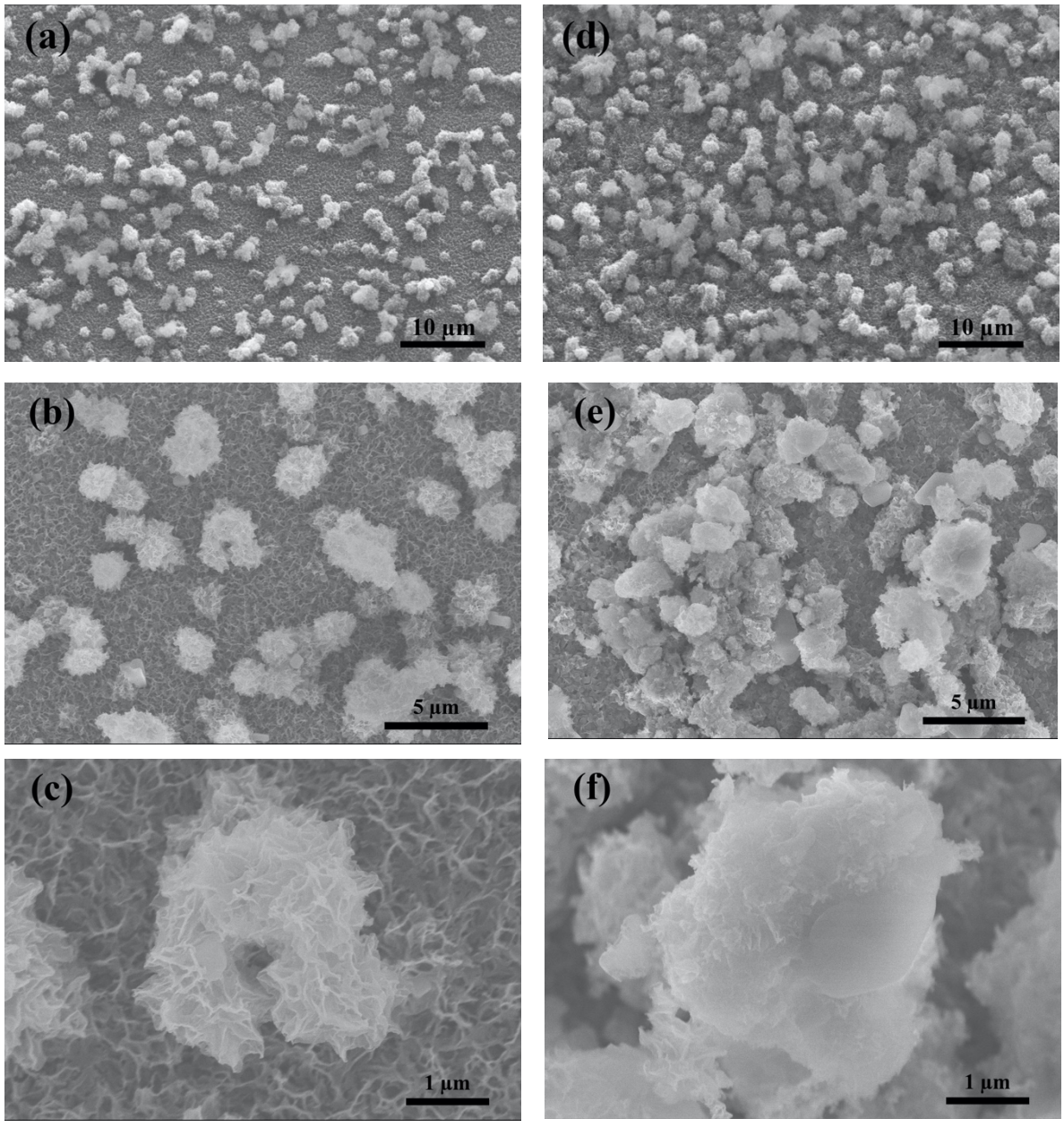

Fig. 4.12. SEM images of untreated Ti after immersed in α-MEM for **(a, b, c)** 7 days, **(g, h, i)** 14 days, **(m, n, o)** 21 days, and PES treated Ti 150 s after immersed in α-MEM for **(d, e, f)** 7 days, **(j, k, l)** 14 days and **(p, q, r)** 21 days

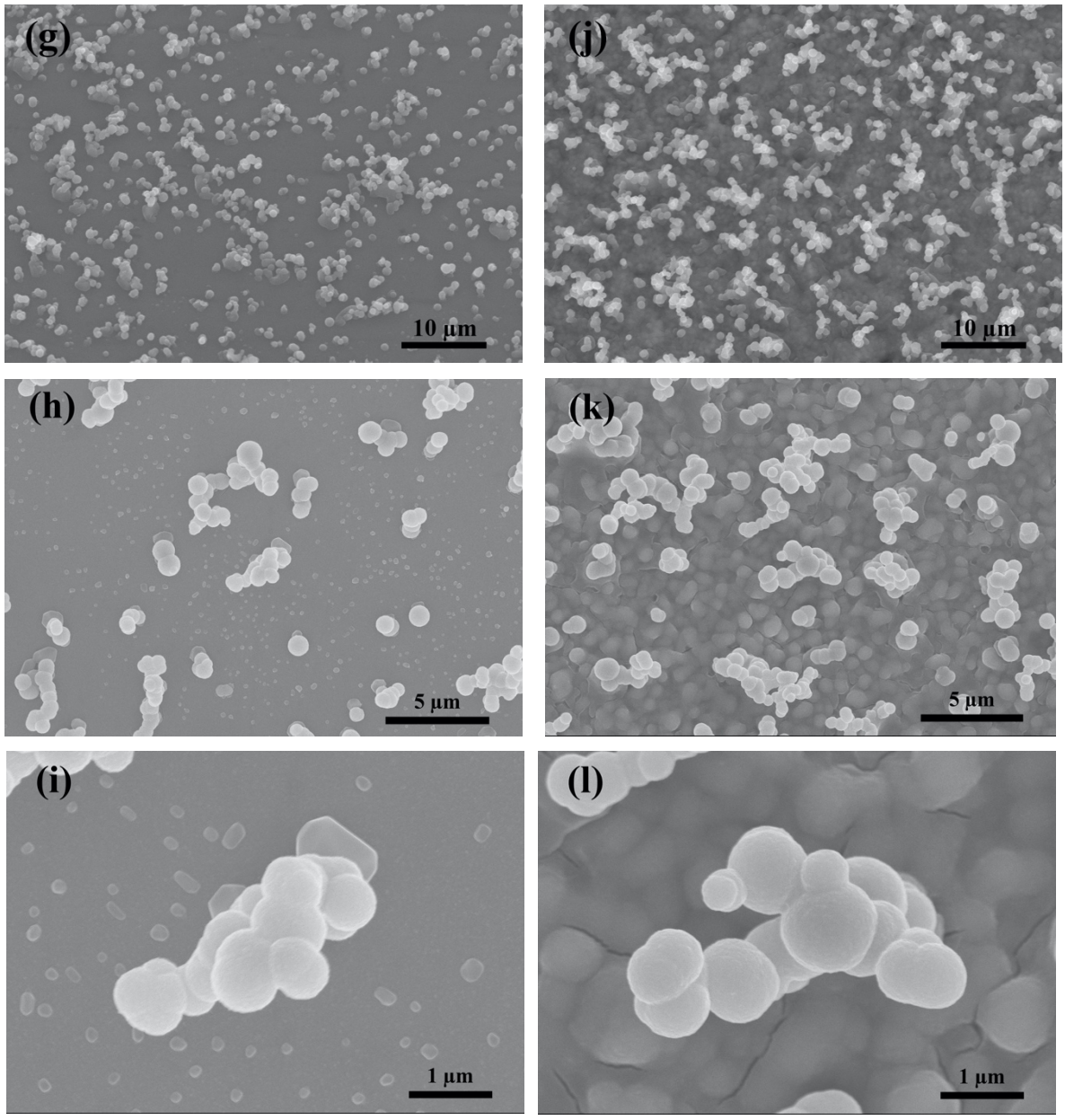

Fig. 4.12. (Cont.)

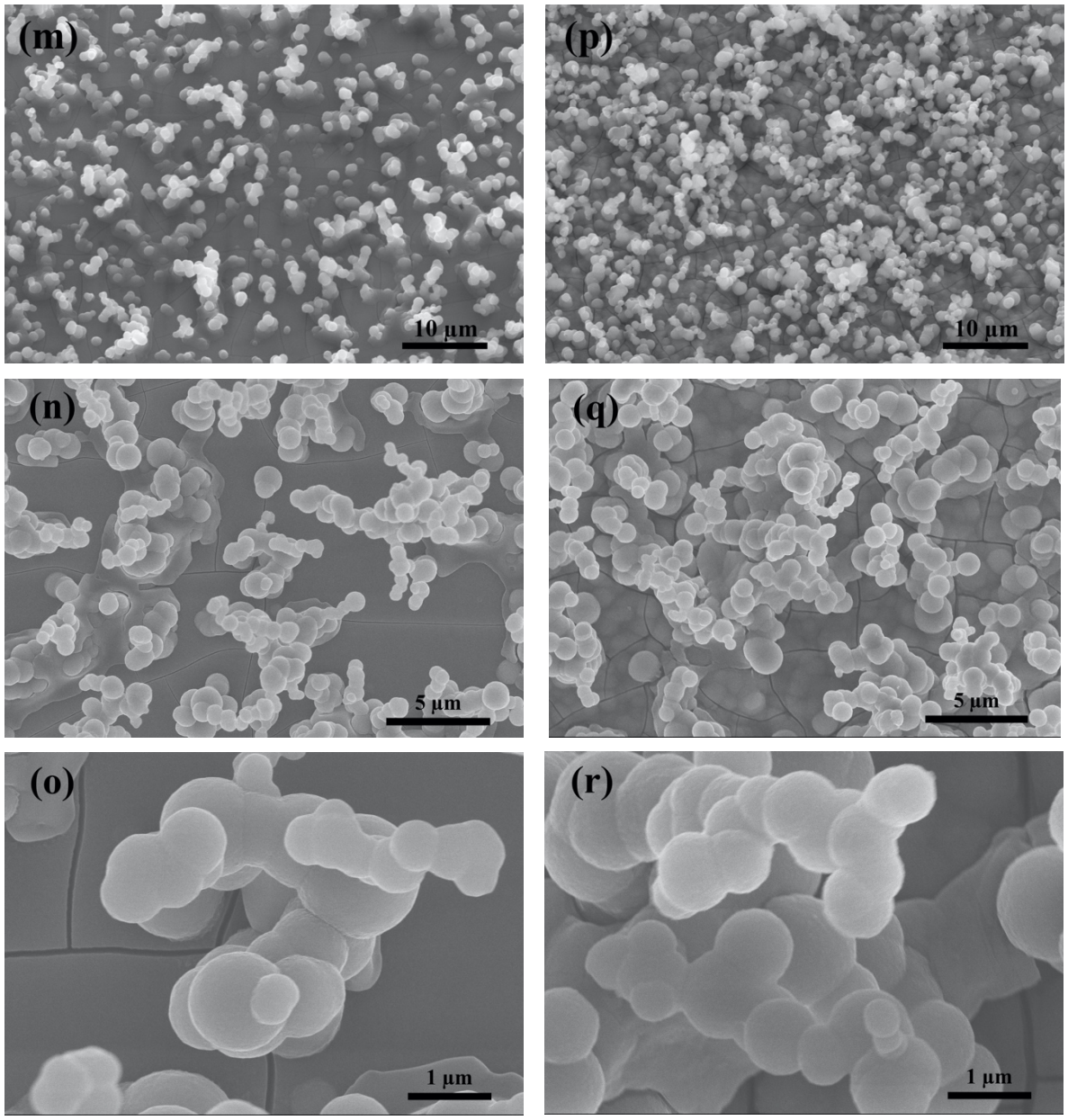

Fig. 4.12. (Cont.)

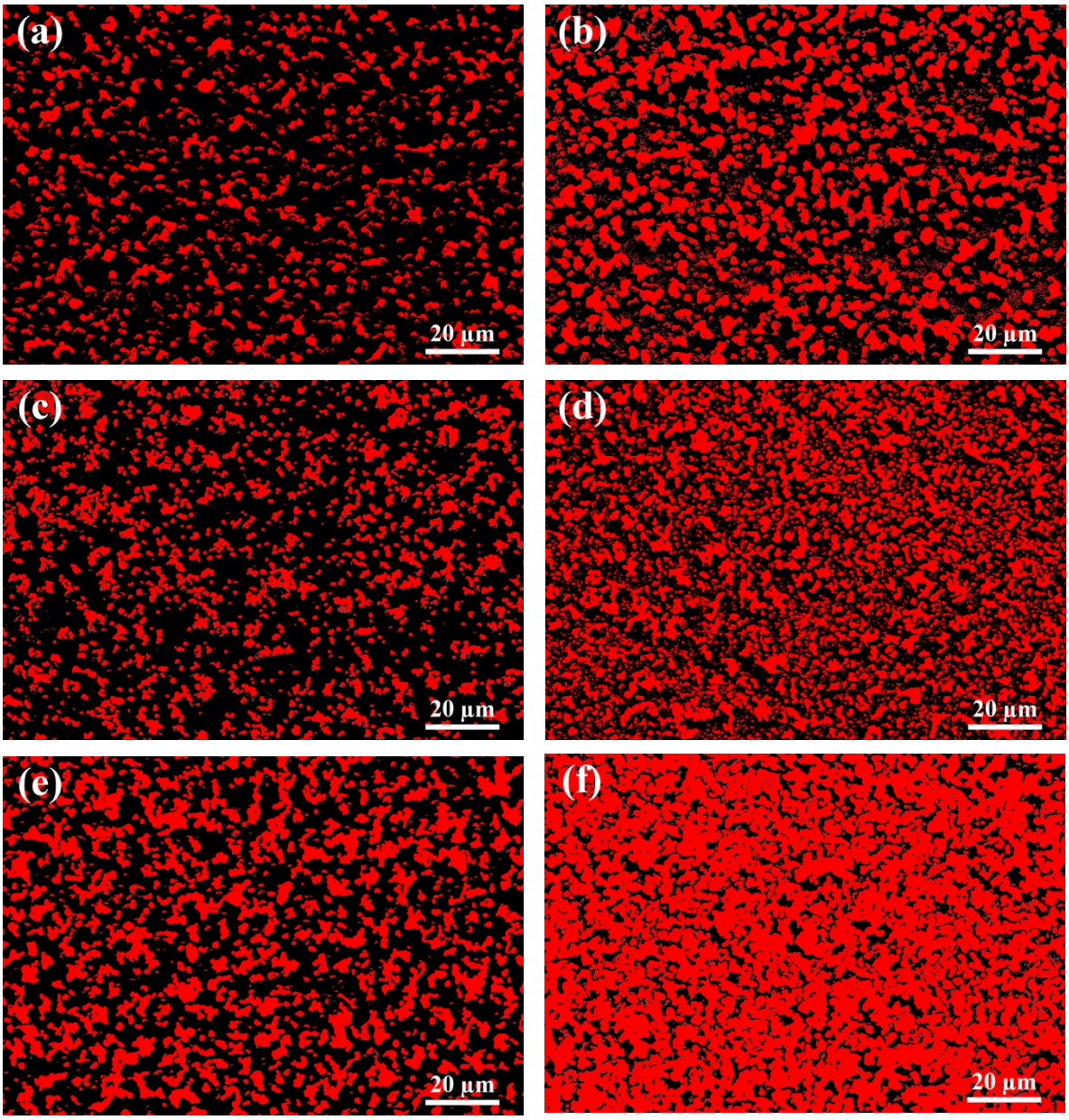

Fig. 4.13. Apatite coverage on untreated Ti after immersion in α-MEM for **(a)** 7, **(c)** 14, **(e)** 21 days, PES treated Ti after immersion in α-MEM for **(b)** 7, **(d)** 14, and **(f)** 21 days

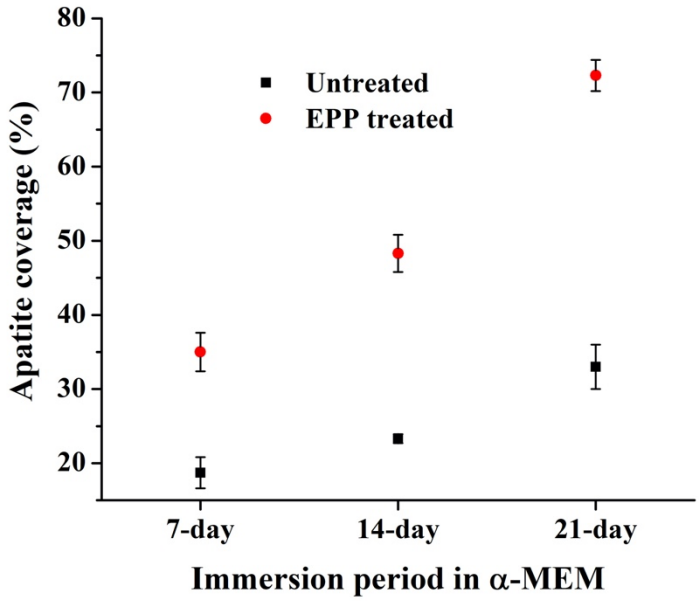

Fig. 4.14. Percentage of apatite coverage on the Ti substrates after immersion in α-MEM

Saruta et al. has reported similar results from their study on osteoconductive of acid etched Ti that has surface features close to that found on PES treated Ti for 150 s [119]. They found that the Ti with sub-micro-scale topography, having pit size in the range of 0.1 – 0.5 μm, had better calcium deposition and expression of osteoblastic compared to the group without such compartmental structure. Furthermore, there has also been reported that Ti with surface texture prepared by various techniques, such as blasting, selective laser melting and anodic oxidation, exhibit better osteoconductive/osteointegration compared to flat surface [56][114][120]. Thus, it is important to note that surface topography and hydrophilicity play an important role on bioactivity level of Ti implants.

EDS analysis showed that Ca/P ratio increased with increasing immersion time. The Ca/P ratio of the PES treated Ti after immersed in α-MEM for 7, 14 and 21 days was 1.33 (± 0.08), 1.47 (± 0.05) and 1.68 (± 0.02), respectively. **Fig. 4.15** represents the Ca/P atomic ratio of the

stoichiometric HA and the PES treated Ti after immersion in α-MEM at different duration. At early stage, octacalcium phosphate (OCP, stoichiometric Ca/P ratio = 1.33), was formed after immersion in α-MEM for 7 days. This was in a good agreement to the results that Awad et al. found when immersed Ti6Al4V alloy in α-MEM for 7 days [91]. The OCP morphologies are shown in **Figs. 4.12a-f**. As immersion continued, the plate like morphology of OCP precipitation has developed to dense tricalcium phosphate (TCP, stoichiometric Ca/P ratio = 1.50) after immersed in α-MEM for 14 days. Wang et al. also reported that at early stage of *in vivo* implantation dicalcium phosphate, OCP and TCP tend to form before HA [121]. It is worth mentioning that OCP and TCP are thermodynamically metastable phases, the formation of them at early stage is kinetically favored. Eventually, HA (stoichiometric Ca/P ratio = 1.67) was found after immersion in α-MEM for 21 days. The formation of HA is probably due to the hydrolysis of OCP as shown in equation (4-3) [122]:

$$Ca_8H_2(PO_4)_6 \cdot 5H_2O + 2Ca^{2+} \rightarrow Ca_{10}(PO_4)_6(OH)_2 + 4H^+ \qquad (4\text{-}3)$$

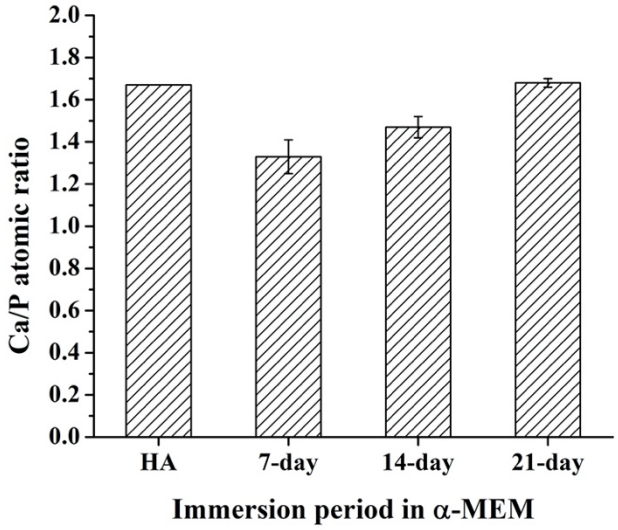

Fig. 4.15. Ca/P atomic ratio of stoichiometric HA and PES treated Ti after immersion in α-MEM

HA is the most stable form of calcium phosphate in physiological environment. It has been reported that HA is able to bond better with surrounding bone rather than dissolve like other unstable calcium phosphate phases *in-vivo* [121][122].

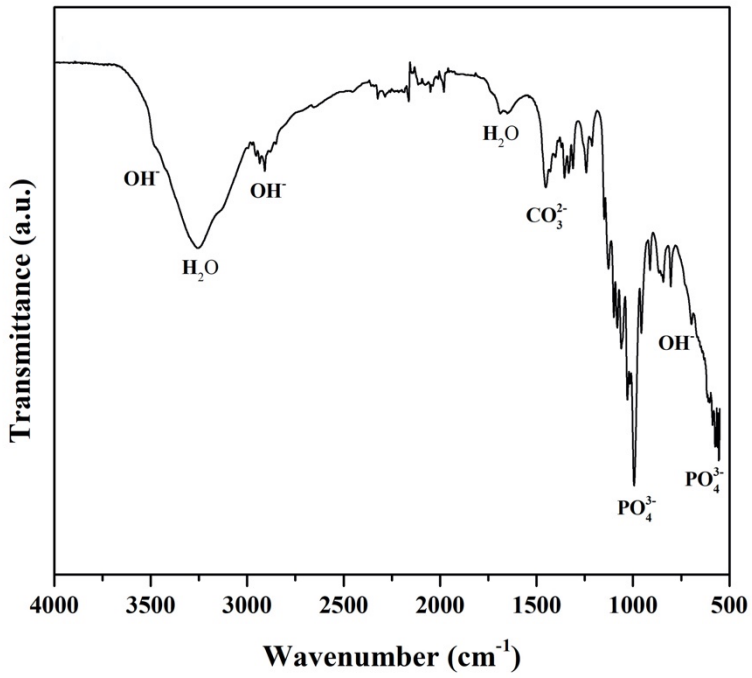

Fig. 4.16. FTIR spectrum of PES treated Ti for 150 s after immersion in α-MEM for 21 days.

FTIR spectrum of PES treated Ti after immersion in α-MEM for 21 days, **Fig. 4.16**, is the evidence that HA has precipitated on the surface. The FTIR spectrum is similar to that of HA powders reported by other studies [123][20][124]. The absorption peaks of PO_4^{3-} at 900 – 1200 and 570 cm^{-1} are attributed to the formation of HA. The shoulder peaks at 3560, 2800, and 600 cm^{-1} are due to the OH stretching of HA. XRD results also confirmed the formation of HA with the presence of HA (211) and HA (203) peaks at 2θ = 31.77º and 45.31º, respectively (JCPDS #09-0432). The XRD pattern of PES treated Ti after immersion in α-MEM for 21 days is shown in **Fig. 4.17**. It is important to note that, even though the SBF or α-MEM are not able to mimic the

ability of living physiological system, i.e., maintaining stable range of pH level over time. However, at present both provide a useful tool to predict the bioactivity of a material before its implantation *in-vivo* [125].

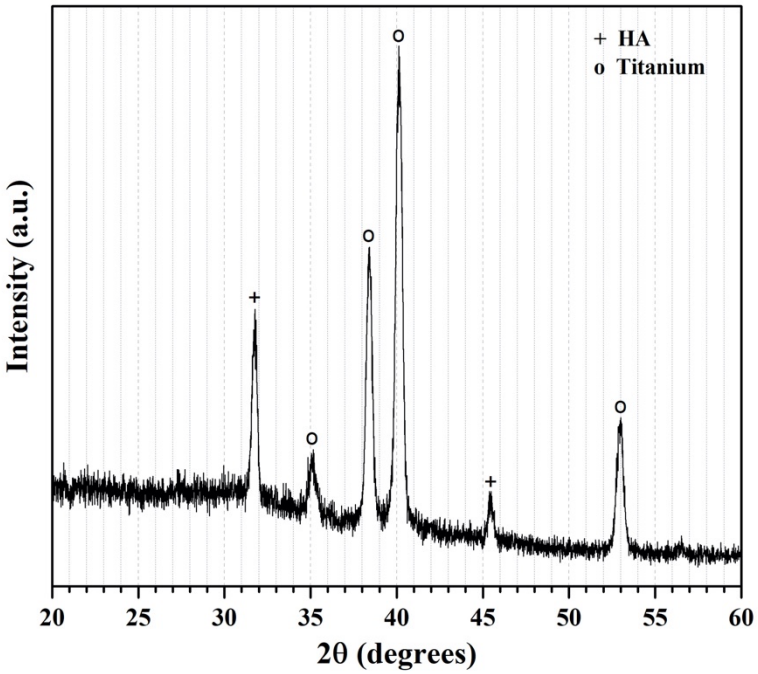

Fig. 4.17. XRD of PES treated Ti for 150 s after immersion in α-MEM for 21 days

4.1.6. *In-vitro* study with MC3T3 cell culture

In-vitro cell culture studies were performed to evaluate the cells' attachment, proliferation, and viability on the EPP treated Ti surface. **Figs. 4.18a-d** present fluorescent images of live cells (green) attachment and growth on the Ti surfaces. It can be clearly noticed that the cell attachment and viability are significantly higher on the PES treated Ti surface, i.e., **Fig. 4.18b** and **4.18d** compared to the untreated surface **Fig. 4.18a** and **4.18c** after 24 and 48 hr, respectively. For quantitative analysis, the fluorescence images were further used to count the exact number of cells on each sample, the data are presented as box plots in **Fig. 4.19a**.

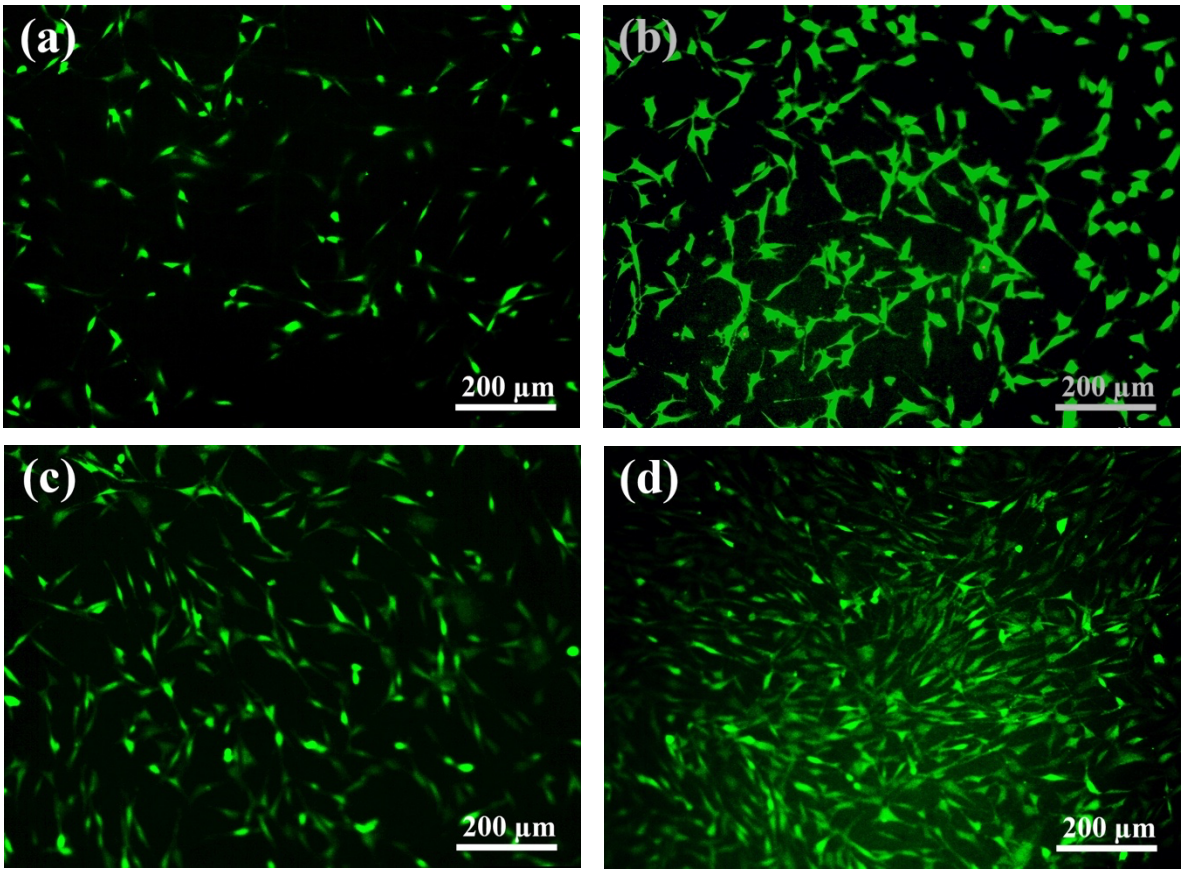

Fig. 4.18. Cells attachment and viability on the Ti-surfaces, **(a)** and **(c)** show the live cells on the untreated Ti surface after 24 and 48 hr, **(b)** and **(d)** show the live cells on the PES treated Ti surface after 24 and 48 hr, respectively.

The number of cells was significantly higher on EPP treated surface (236 ± 45 and 362 ± 80, at 24 and 48 hr, respectively) compared to the untreated surface (176 ± 39 and 244 ± 74, at 24 and 48 hr, respectively) with significance degree of *** $p < 0.001$. Furthermore, MTS assay was used for quantitative analysis of the cells' proliferation and growth after 24 and 48 hr as indicated in **Fig. 4.19b**. The MTS assay findings confirmed the results obtained from the live cell's count indicating a higher cell's attachment and proliferation on the EPP treated surface compared to the untreated Ti surface. Tissue culture plate was used as a positive control for the MTS study.

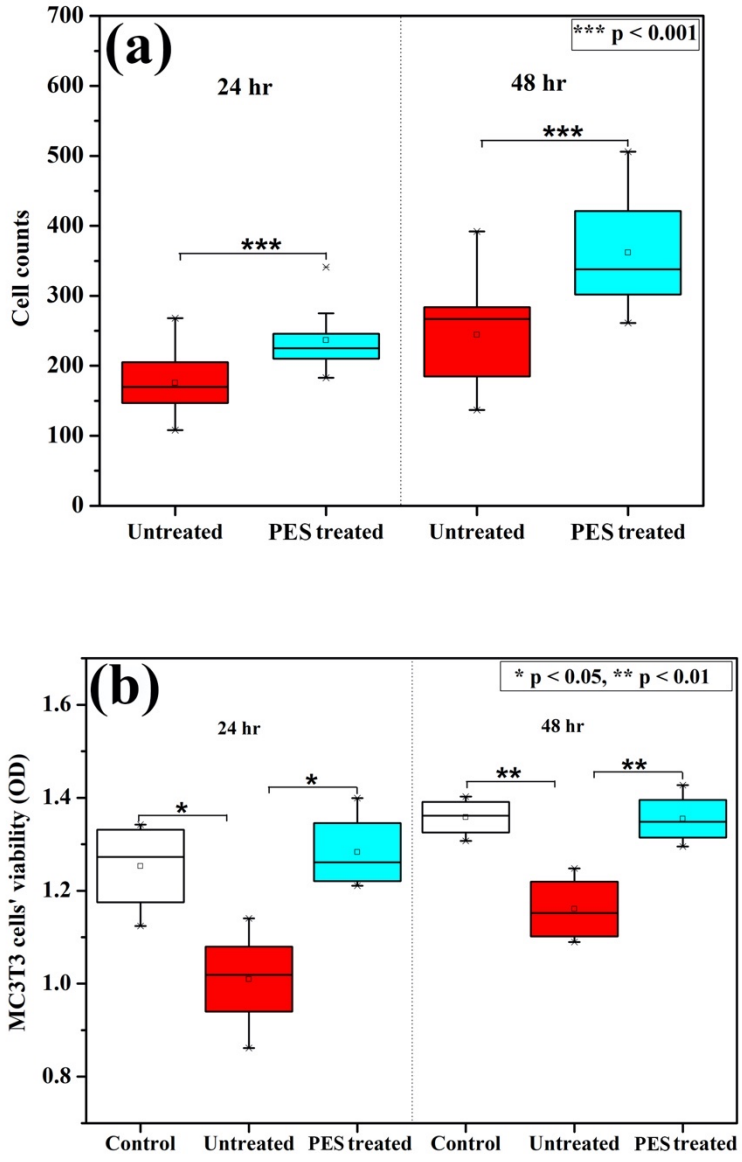

Fig. 4.19. (a) Cell counts and **(b)** MTS assay results after 24 and 48 hr

It is important to note that there was no significant difference in the cell's viability between the EPP treated Ti surface compared to the positive control. While both positive control and EPP treated surfaces were significantly higher in the cell's viability compared to the untreated surface at 24 and 48 hr with significance degree of *p < 0.05 and ** p < 0.01. These data concluded that

the EPP treated surface could enhance the cells' viability and proliferation without any cytotoxicity effects.

4.2. Plasma electrolytic oxidation

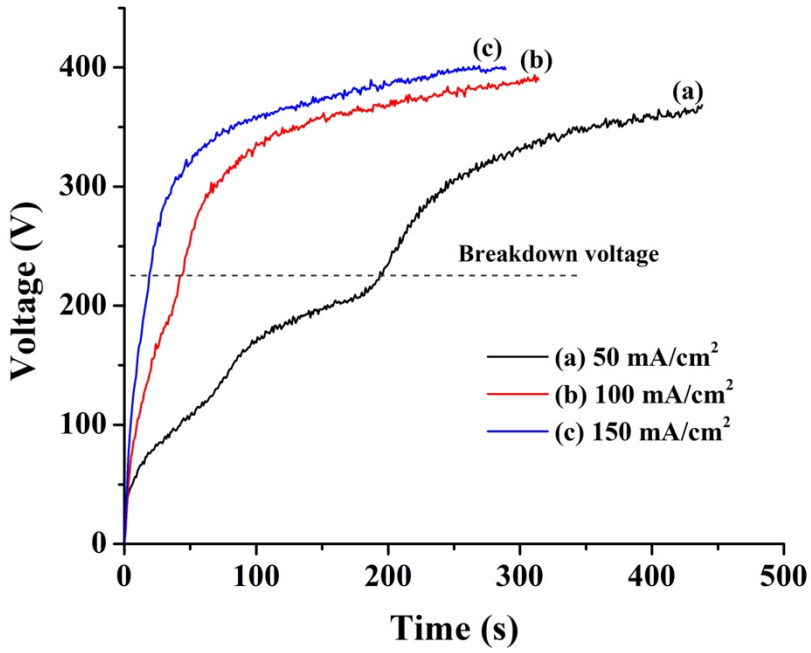

Fig. 4.20. Voltage – time response of PEO at different applied current density

The characteristics of PEO process are dependent on processing parameters. The applied current density affects the rate of voltage response as can be seen from **Fig. 4.20**. However, it was observed in this study that changing the applied current density alone did not result in shifting the dielectric breakdown voltage. Fine plasma started to occur at about 220 V for all applied current density levels, but the voltage increased at a faster rate when a higher current density was used. This is due to a stronger electric field applied on the electrodes. The anodic and cathodic reaction took place more rapidly. The oxide built up at faster rate on the anodic surface, thus, critical thickness for the dielectric breakdown was achieved in 20 and 40 s for the PEO treatments at 150

and 100 mA/cm^2, respectively. While the PEO treatment at 50 mA/cm^2 took 180 s to reach the dielectric breakdown voltage.

4.2.1. Chemical composition and surface morphology

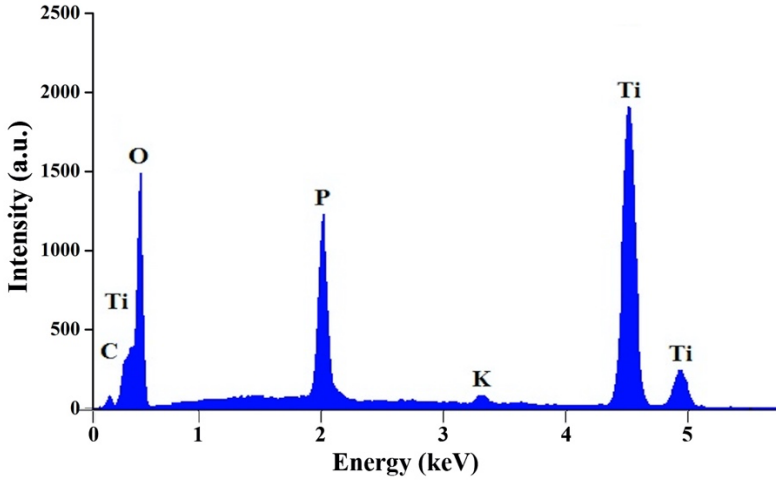

Fig. 4.21. An EDS spectrum of PEO treated Ti

EDS analysis revealed that the PEO treated samples contained O, P, K, and Ti, which are the constituent elements in the electrolytic bath and the underlying substrate. A typical EDS spectrum of a PEO treated sample is shown in **Fig. 4.21**. Oxygen was the main element on the surface due to the presence of the TiO_2 layer that forms during the treatment. **Table 4.2** summarizes the O, P, and K content of the PEO treated Ti at different current density and treatment duration. The O, P, and K were in the range of 46.3 – 50.3, 5.8 – 9.1, and 0.2 – 0.7 at. %, respectively. The P slightly decreased when the processing time was increased.

Table 4.3. EDS analysis of PEO treated Ti

Treatment duration (s)	Applied current density (mA/cm^2)	Elemental percentage (atomic %)		
		O (SD)	P (SD)	K (SD)
90	50	49.6 (2.6)	9.1 (1.1)	0.2 (0.1)
	100	50.3 (1.0)	7.9 (0.7)	0.4 (0.2)
	150	48.9 (3.1)	6.7 (2.3)	0.3 (0.2)
270	50	46.3 (4.6)	8.3 (1.0)	0.5 (0.5)
	100	50.1 (2.5)	6.4 (0.6)	0.7 (0.5)
	150	46.9 (3.3)	5.8 (2.0)	0.7 (0.3)

SEM analysis was performed to examine the surface morphology of the PEO produced layers on Ti. **Figs. 4.22** presents the surface morphology of the PEO coatings on Ti. A pore structure is evident in all PEO coatings. This was the result of highly localized electric field that initiated micro discharge channels on the Ti surface [12]. It is interesting to note that a larger number of fine pores were produced in treatments conducted at lower current densities. This is because a PEO treatment at low current density results in the development of a greater number of fine plasma discharge [16]. The size and number of pores were analyzed using ImageJ software and their distribution is shown in **Fig. 4.23**. Processing at higher current densities and for longer durations reduced the number of fine pores due to the formation of larger discharge channels at higher voltage and a sealing effect occurring on the pores. Furthermore, processing up to 270 s resulted in an agglomeration of pores, creating a complex pore structure, as can be seen from the morphology in **Fig. 4.22d-f**.

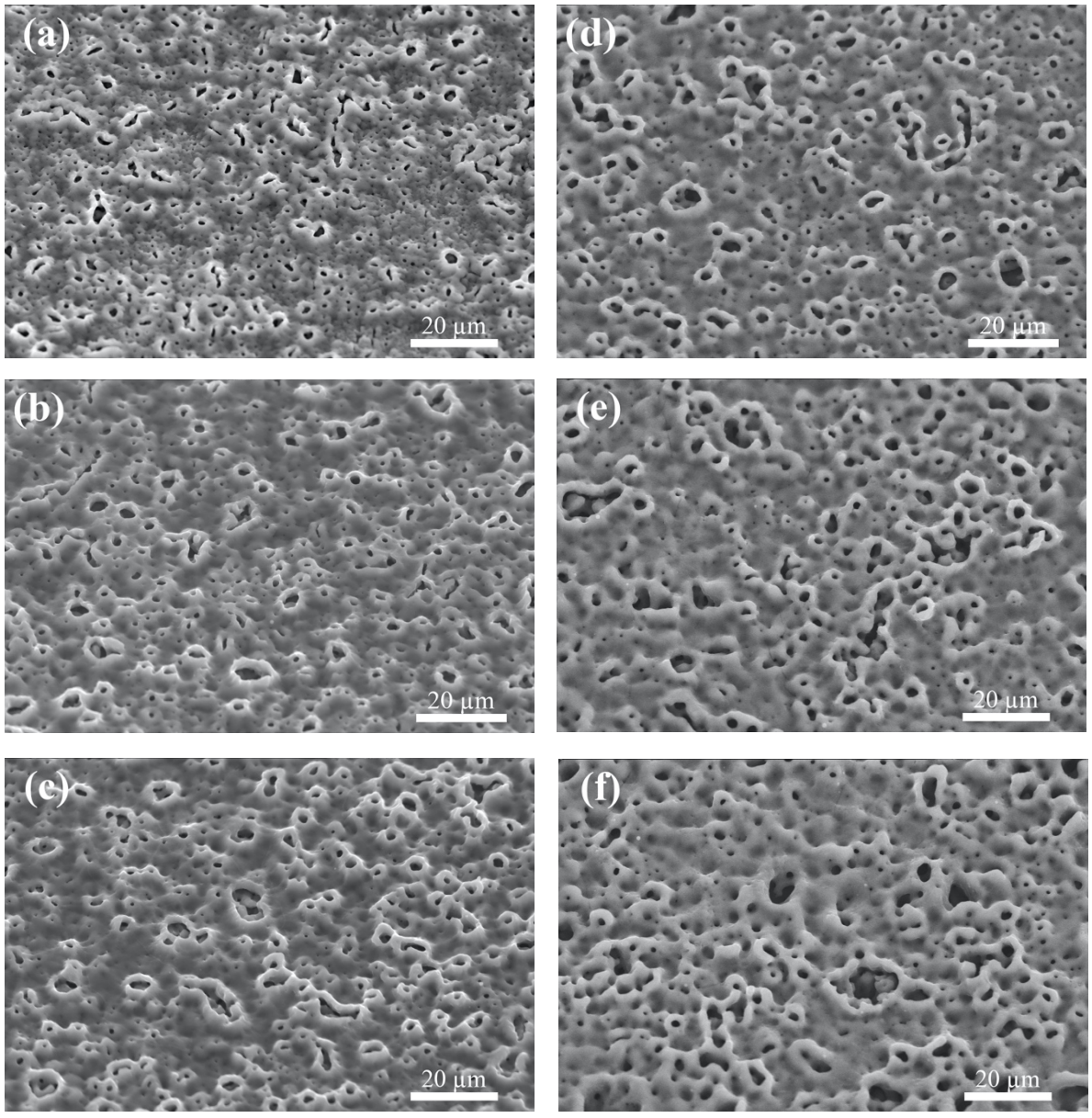

Fig. 4.22. SEM images of PEO treated for 90 s at **(a)** 50 mA/cm^2, **(b)** 100 mA/cm^2, and **(c)** 150 mA/cm^2, 270 s at **(d)** 50 mA/cm^2, **(e)** 100 mA/cm^2, and **(f)** 150 mA/cm^2

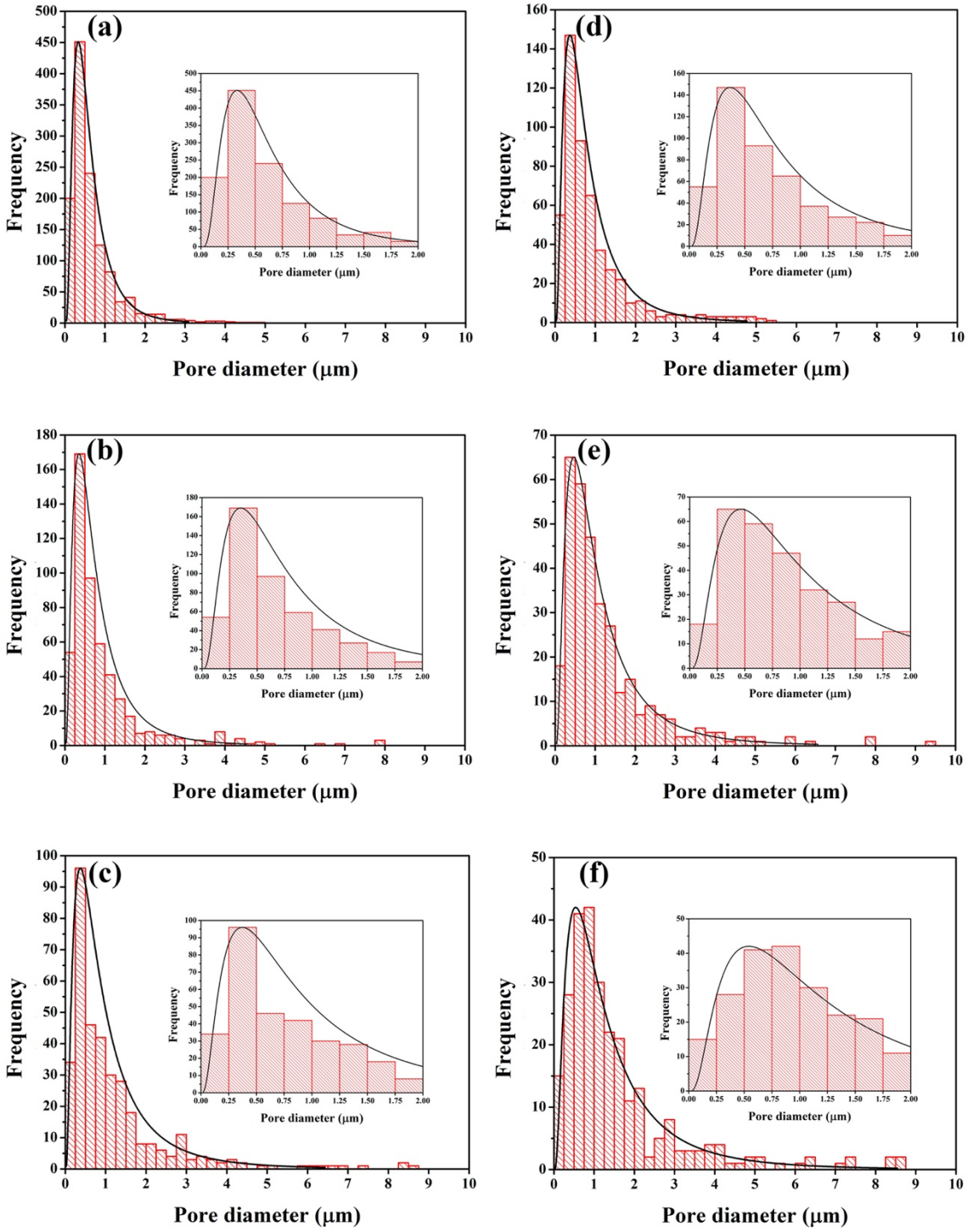

Fig. 4.23. Pore distribution of PEO treated for 90 s at **(a)** 50 mA/cm^2, **(b)** 100 mA/cm^2, and **(c)** 150 mA/cm^2, 270 s at **(d)** 50 mA/cm^2, **(e)** 100 mA/cm^2, and **(f)** 150 mA/cm^2

FTIR studies of the PEO coatings showed the existence of phosphate (PO_4^{3-}) stretching modes in the range of 1025 – 1030 cm^{-1}, and the presence of (Ti-O) bending vibration of TiO_2 [69]. **Fig. 4.24** presents the FTIR spectra of the PEO treated Ti at various current densities and durations. The transmittance of (PO_4^{3-}) slightly increased when performing PEO at higher current densities. It is possible that at higher current densities O atoms tend to bond with Ti to form TiO_2 rather than forming phosphate group as we have seen the declining of P in the EDS analysis.

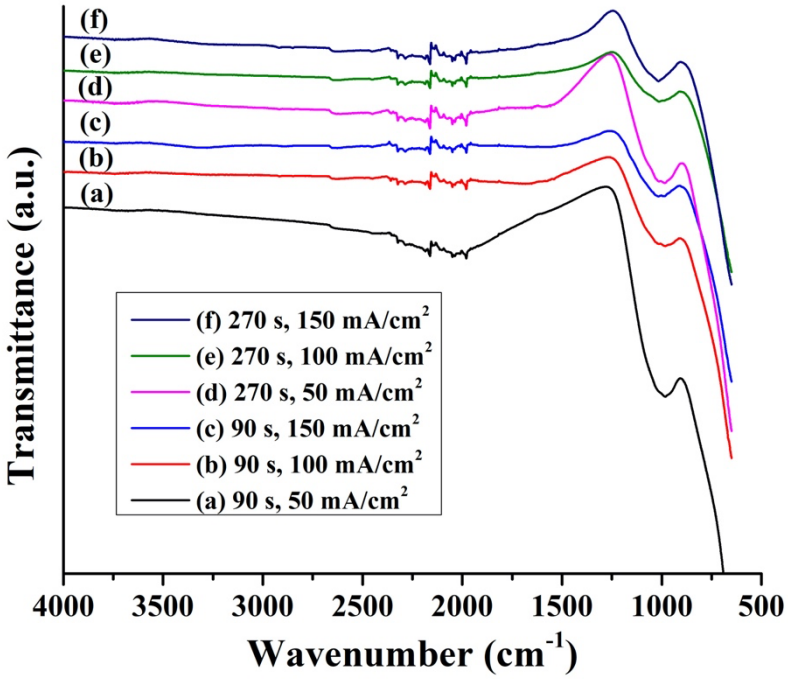

Fig. 4.24. FTIR spectrum of PEO at different processing duration and current densities

4.2.2. Surface roughness and wettability

To further investigate surface topography of the produced oxide layers, surface roughness and other roughness parameters were obtained by optical profilometry. The values of *Sa*, *Sz*, *Ssk*, and *r* are presented in **Table 4.3**. The results showed a general trend indicating that increasing current density and treatment duration led to an increasing of *Sa*. However, the roughness of all

PEO groups is similar and remains at low levels *Sa* 500 – 1,000 nm [5]. The *Sz* seemed to stabilize at around 10.1 – 11.0 μm except for the sample treated at 50 mA/cm^2 for 90 s, which exhibited *Sz* of 8.6 μm. For such low current density and short processing time, fine discharge channels were dominant and as a result smaller pore structures were developed. The results also showed a general trend indicating that increasing current density and treatment duration led to a decreasing of *Ssk* and *r*. The distribution of hills and valleys became more uniform as indicated by the *Ssk* values changing from –1.1 to –0.3. The decreasing of *r* was due to the reduction of the number of fine pores as shown in **Figs. 4.23**.

Table 4.4. Roughness parameters of PEO treated Ti

Treatment duration (s)	Applied current density (mA/cm^2)	Roughness parameters			
		***Sa* (SD) [nm]**	***Sz* (SD) [μm]**	***Ssk* (SD)**	***r* (SD)**
90	50	636 (4)	8.6 (0.1)	-1.1 (0.1)	427 (14)
	100	659 (13)	10.1 (0.5)	-1.0 (0.1)	391 (16)
	150	708 (23)	11.0 (1.1)	-0.7 (0.1)	315 (7)
270	50	722 (37)	10.4 (0.6)	-0.5 (0.1)	252 (7)
	100	873 (27)	10.4 (0.5)	-0.3 (0.1)	204 (6)
	150	929 (20)	10.8 (0.7)	-0.5 (0.1)	199 (5)

All PEO treated Ti exhibited superwetting characteristics with a contact angle <1^o while the as-polished Ti exhibited a contact angle of 39^o. **Fig. 4.25** presents a typical water droplet spreading on a PEO treated Ti surface. Due to the large surface area produced by the PEO treatment, as indicated by the *r* value, *hemi-wicking* occurred and superhydrophilic behavior was developed. The mechanism of superwetting surface has already been described in another report [126]. It should be noted that the *r* values of the PEO treated surface are much larger compared to that of the as-polished Ti. Moreover, the presence of surface charges from (PO_4^{3-}) has also facilitated the formation of hydroxyl groups. These hydroxyl groups are beneficial for water droplet spreading [127]. Thus, the combination of surface topography and chemistry of the PEO

treated Ti yielded a superhydrophilic surface. It has been reported that a superwetting surface exhibits better osteoconduction, osseointegration, and cellular response both *in-vitro* and *in-vivo* compared to a surface with lower hydrophilicity level [6][8][103][7].

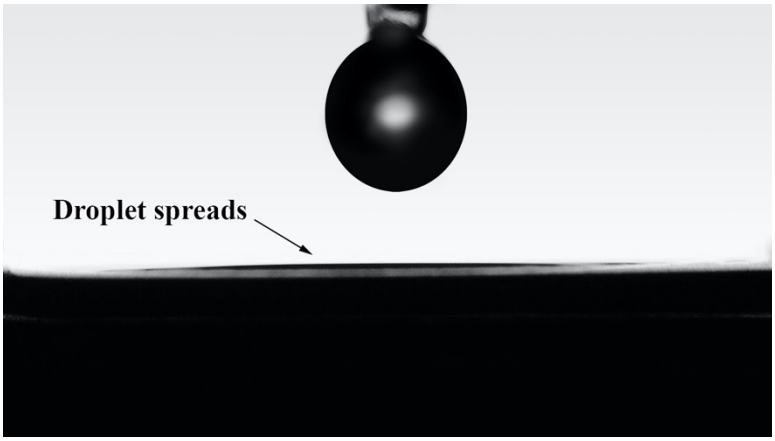

Fig. 4.25. A water droplet spreads on PEO treated Ti

4.2.3. Surface energy

Eq. (2-14) was also used to determine surface energy of the PEO treated surface. The surface tension components of the water and diiodomethane droplets are listed in **Table 4.1** The CA of the diiodomethane on the as-polished and PEO treated was 31° and 13°, respectively. The as-polished Ti and the PEO treated had the surface energy of 61.62 mJ/m^2 and 75.8 mJ/m^2, respectively. The PEO treated surface exhibited higher surface energy compared to that of the as-polished surface.

4.2.4. XRD analysis

Fig. 4.26. presents the XRD patterns of the PEO treated Ti at various current densities and treatment durations. The XRD analysis revealed TiO_2 and Ti peaks for all treatment conditions. Two TiO_2 phases were detected in the coatings, namely anatase and rutile. Anatase was formed in

all coatings, while rutile formed only in the coatings produced at 100 and 150 mA/cm^2. Anatase is a metastable phase, that eventually transforms to the stable TiO_2 phase of rutile, in the presence of sufficient energy and time. Anatase was detected at 2θ angles of 25.3°, 36.9°, 37.8°, 48.0°, 53.9°, and 55.1° corresponding to the (101), (103), (001), (100), (105), and (211) planes, respectively (JCPDS #21-1272). Anatase was formed in all PEO coatings since it is kinetically favored. As shown earlier, the response of the electrode potential during PEO is dependent on the level of the applied current density. At high current densities, the potential rose at a faster rate, producing stronger plasma and larger discharge channels. Hence, at 100 and 150 mA/cm^2, the coatings had sufficient energy to transform anatase to rutile. Nonetheless, it is important to note that when the Ti was treated for 90 s, the intensity of the rutile peaks was relatively low and almost undetectable in the coatings prepared at 100 mA/cm^2. The anatase to rutile transformation may be limited for such a short processing period. The XRD results showed the peaks of rutile at 2θ angles of 27.4°, 36.1°, and 41.2° corresponding to the (110), (101), and (111) planes, respectively (JCPDS #65-0191). The broad peak around $2\theta = 20 – 35°$ observed in all samples corresponds to the formation of an amorphous phase. The broad peak found in the PEO coatings using KOH and $K4P_2O_7$ electrolytes was reported to be attributed to a P containing phase [16].

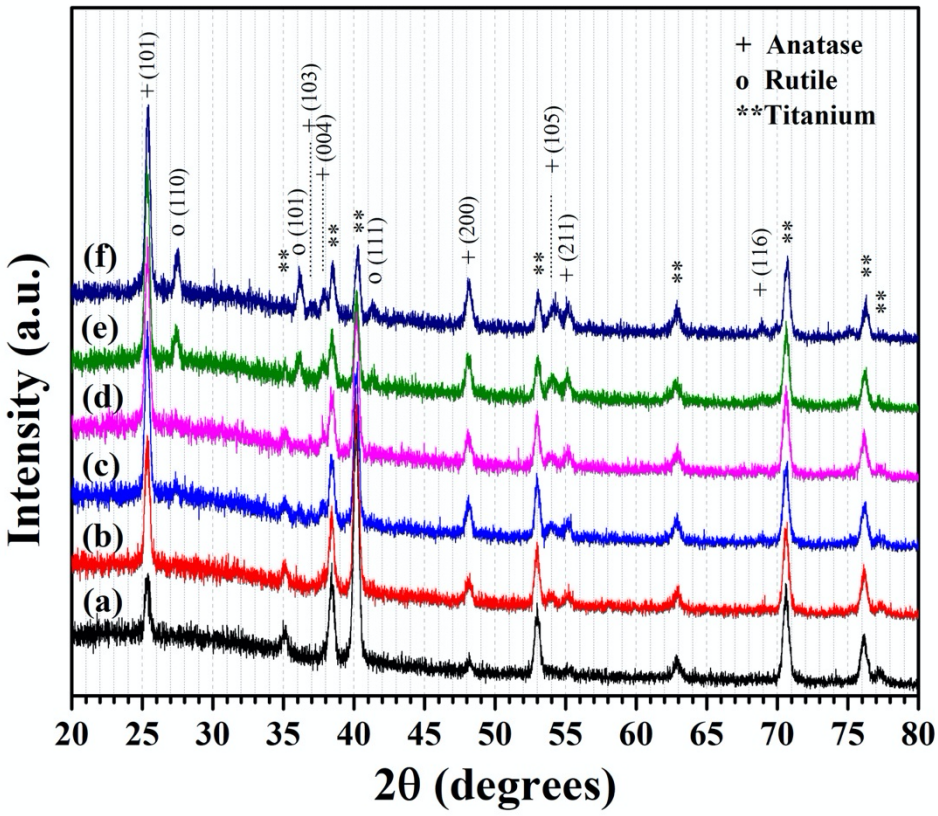

Fig. 4.26. XRD results of PEO coatings for 90 s at (a) 50 , (b) 100, and (c) 150 mA/cm^2, and for 270 s at (d) 50, (e) 100, and (f) 150 mA/cm^2

It has been reported that anatase (100) and rutile (101) planes have the ability to form biomimetic apatite in SBF because they match well with the structure of HA (0004) and (0001), respectively [31][128][129]. However, there is a contradiction in these report on which phase of TiO_2 has shown better bioactivity. The PEO coatings in this study comprised various anatase and rutile phases. The ability to form the biomimetic apatite in cell free media as well as cellular response is reported in the following section.

4.2.5. *In-vitro* studies

Biomimetic apatite formation in cell free media

Fig. 4.27 presents the untreated Ti and PEO treated surfaces after immersion in α-MEM for different time periods. It is clearly seen that, after 21 days, the treated samples have a higher amount of biomimetic apatite formation compared to the untreated Ti. This is in a good agreement with other reports that a surface with rougher profile and better wettability exhibits better biomimetic apatite formation in SBF [126]. It is important to note that there is no significant difference of biomimetic apatite deposition among the PEO treated groups. This is because all PEO treated groups are superhydrophilic and exhibit a similar surface roughness. The present results also reveal that the presence of the two different TiO_2 phases is not influence the ability to induce biomimetic apatite formation when the surface has the same wettability level and roughness range.

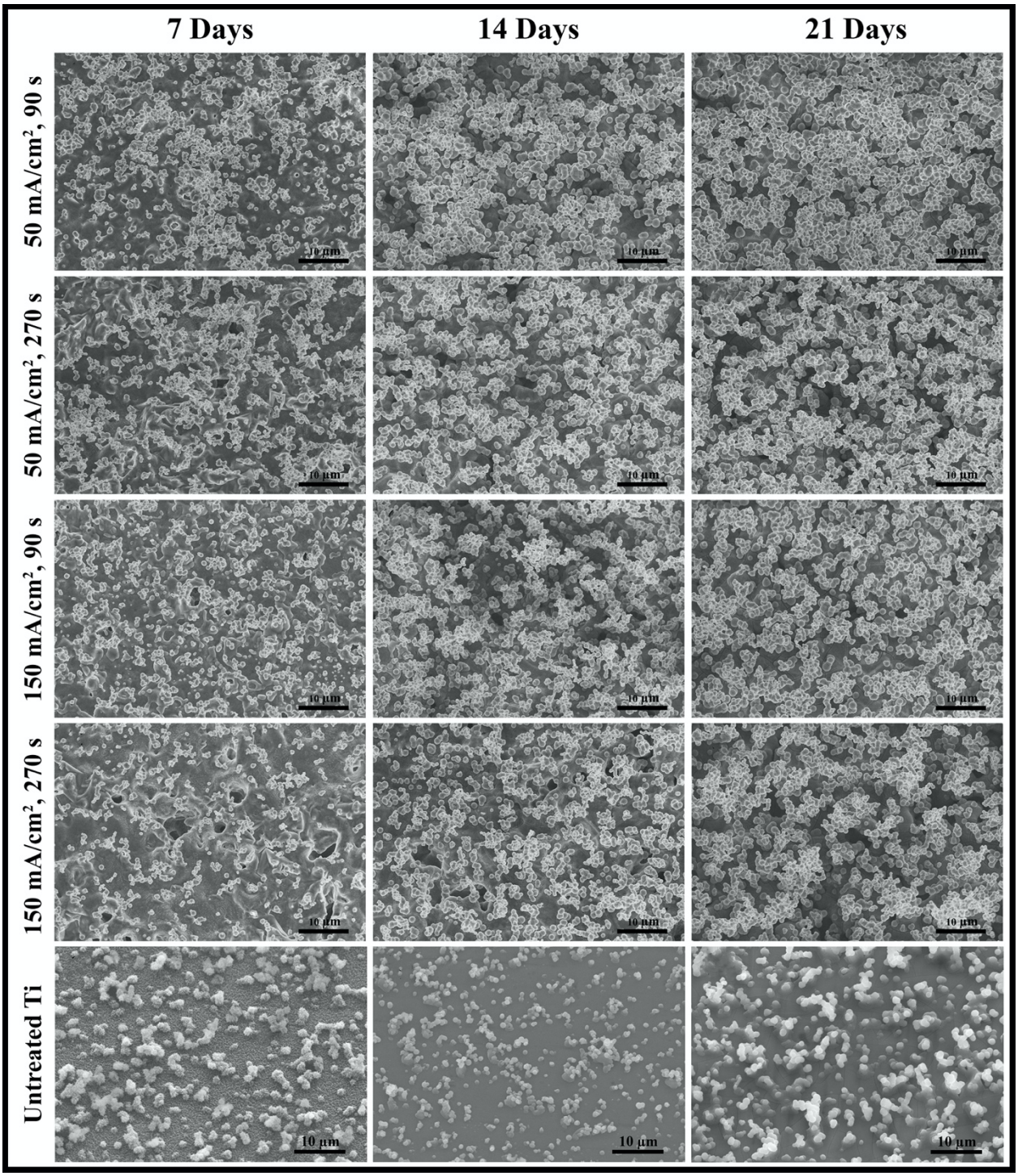

Fig. 4.27. Calcium phosphate precipitation after immersed in α-MEM

The EDS analysis shows that Ca/P ratio of the precipitated biomimetic apatite on PEO treated Ti increased as immersion duration increased. The Ca/P ratio of the biomimetic apatite on the treated Ti was 1.48 (± 0.08), 1.64 (± 0.05), and 1.70 (± 0.06) after 7, 14, and 21 days of immersion, respectively. Dense tricalcium phosphate (TCP, stoichiometric Ca/P ratio = 1.50) was formed after 7 days of immersion, then it developed to HA (stoichiometric Ca/P ratio = 1.67) when the immersion time reached 14 days. It is important to note that HA is the most stable phase of calcium phosphate. The other calcium phosphate phases, such as dicalcium phosphate, octacalcium phosphate (OCP, stoichiometric Ca/P ratio = 1.33), and TCP tend to dissolve in the biological system. The Ca/P ratio of the biomimetic apatite on the untreated Ti was 1.29 (± 0.04), 1.41 (± 0.03), and 1.50 (± 0.09) after 7, 14, and 21 days of immersion, respectively. After the first week of immersion, the morphology of the precipitation on the untreated Ti was different from the PEO treated groups. The flower like structure that loosely formed is characteristic of OCP. High resolution SEM micrographs of the OCP have been published in the previous report [126]. The OCP will eventually dissolve and form denser and more compact structure of calcium phosphate phases, such as HA, as we can see from the SEM images of the untreated Ti after immersion in α-MEM for 14 and 21 days in **Fig. 4.27** [121]. The transformation of OCP to HA is probably occurred by the hydrolysis of OCP as shown in Eq. (1) [122]. The transformation of OCP to HA is probably occurred by the hydrolysis of OCP as shown earlier in Eq. (4-3) [122].

The biomimetic apatite precipitation on the PEO treated Ti was confirmed to be HA by XRD and FTIR analysis. **Fig. 4.28** is the XRD pattern of the PEO treated Ti at 50 mA/cm^2 for 90 s after immersion in α-MEM for 21 days. HA (211) and (203) diffractions were observed at 2θ = 31.77° and 45.31°, respectively (JCPDS #09-0432). The FTIR results shown in **Fig. 4.29** also confirmed the formation of HA on the PEO treated samples. The peaks of PO_4^{3-} at 1020 and

570 cm^{-1} and the shoulder peaks of OH stretching at 3500 and 2800 are attributed to the formation of HA.

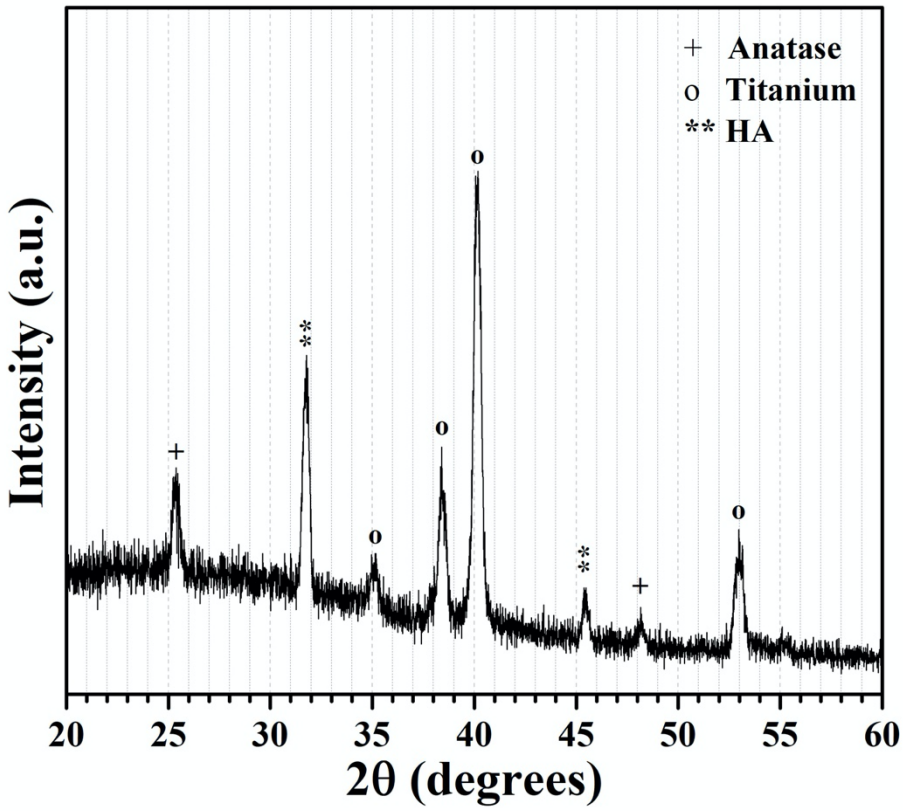

Fig. 4.28. XRD peaks of PEO treated Ti after immersed in α-MEM for 21 days

MSCs in-vitro cytotoxicity studies

The effect of the PEO treatment on the cellular behavior (i.e., cytotoxicity, cell's adhesion, and viability) were also evaluated using human MSCs compared to the untreated Ti (as-polished) surface as a control. MSCs are typically used in the field of tissue engineering applications due to their ability for self-renewal, capability to proliferate and then differentiate into different cell-type such as bone [95,96], ligament [97], adipose [98], cartilage [99,100], and muscle [101] tissues based on the type of conditioned cell culture media being used. Here, cells proliferation

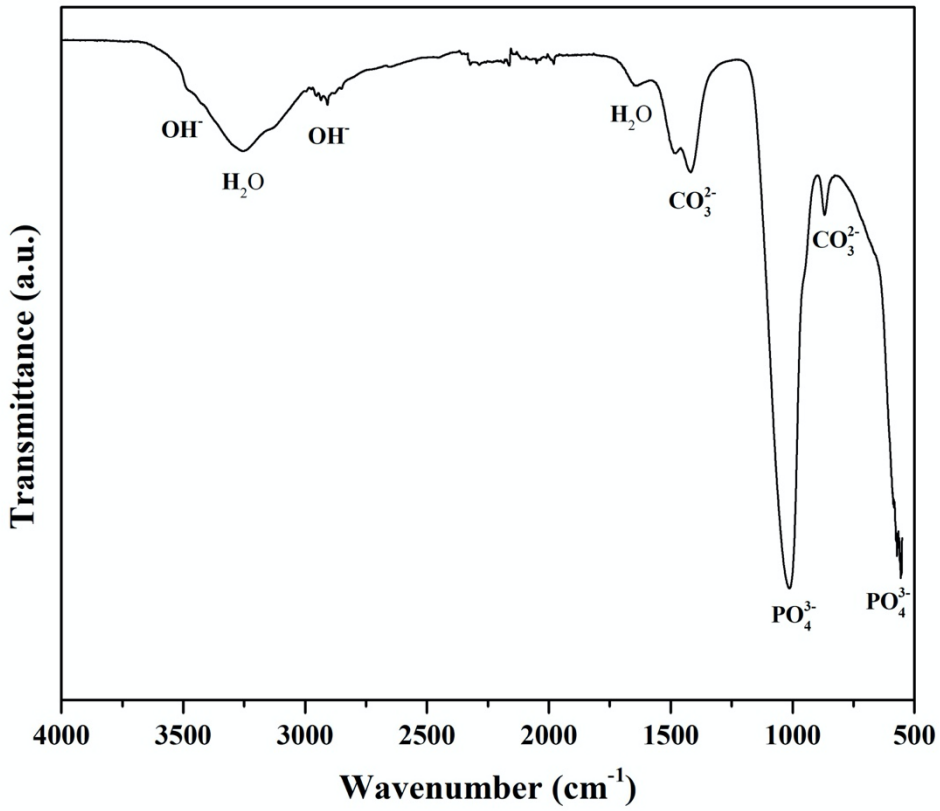

Fig. 4.29. FTIR spectrum of the PEO treated Ti after immersed in α-MEM for 21 days

was quantified by an MTS assay (quantitative cytotoxicity assay) while cell viability was further assessed by live/dead staining (qualitative cytotoxicity assay). **Fig. 4.30a** shows the MTS assay cell viability results after 24 and 72 hrs of MSCs proliferation on the tested surfaces, respectively. Data are presented in a boxplot with the standard deviation and the mean of each group. Although the MTS results indicated that the PEO treated groups have higher cells proliferation, significant differences were not observed.

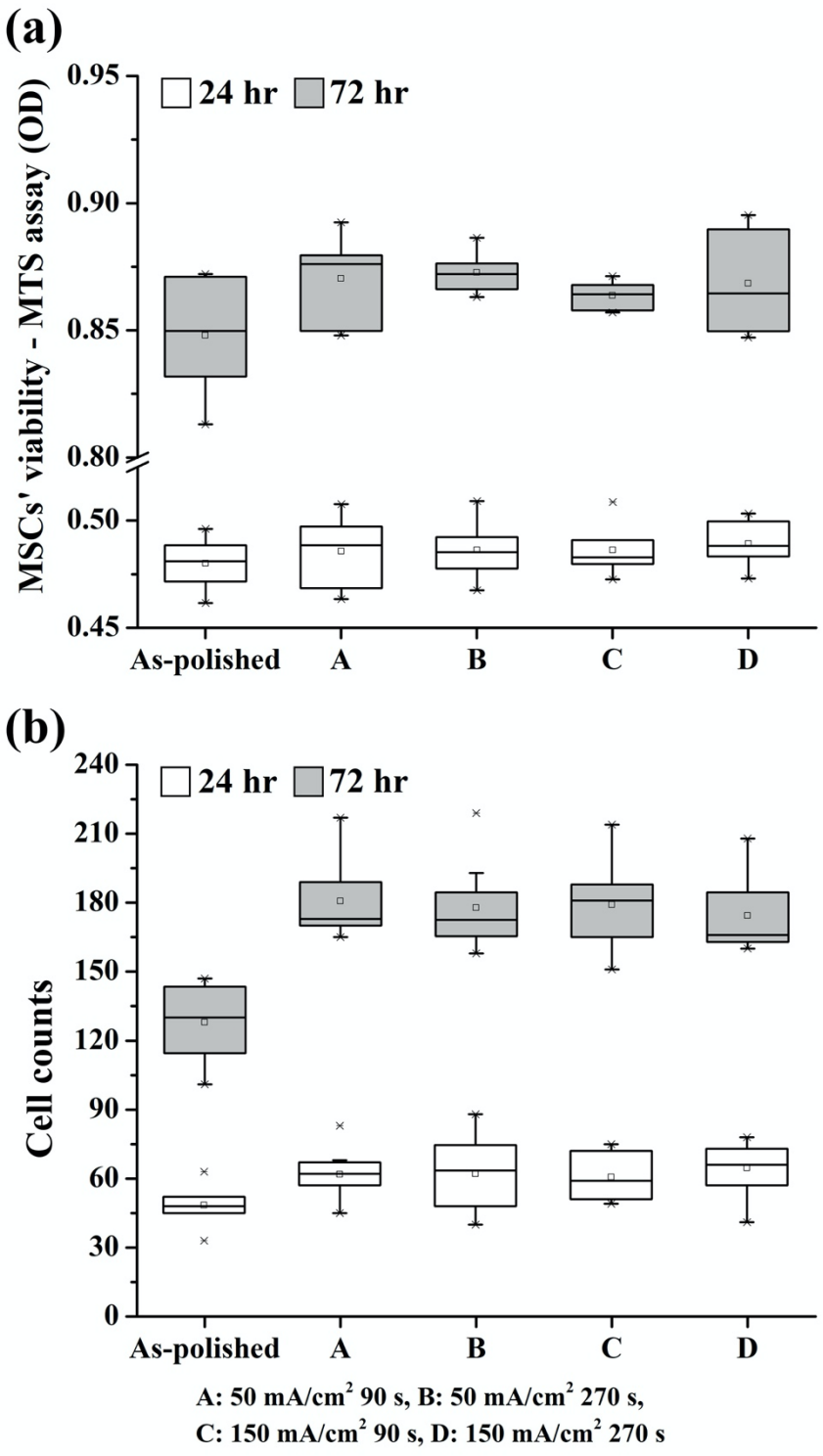

Fig. 4.30. MSCs' viability and proliferation after 24 and 72 hrs of culture (a) MTS assay and (b) live cell counts

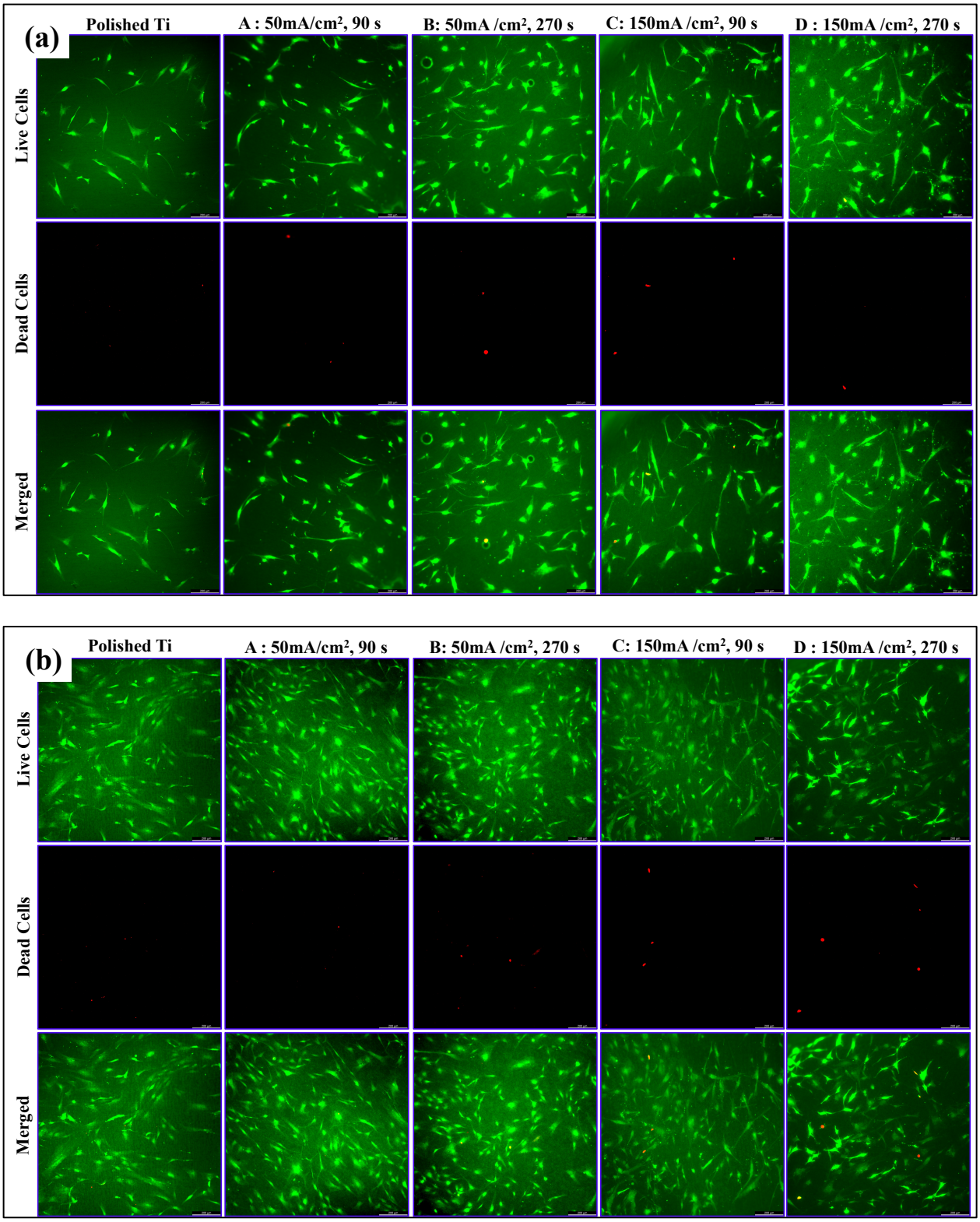

Fig. 4.31. Fluorescence images of live cells and dead cells after culture for (a) 24 and (b) 72 hrs

Fluorescence images in **Fig. 4.31** show the live cells (green) and dead cells (red) on the different tested surfaces which indicated good cell adhesion and spread on the surfaces. Almost no red stained cells were observed meaning there is not cytotoxic effect on the PEO treated surfaces as well as the as-polished Ti after 24 and 72 hr. Green stained cells (live) indicated a good cell's adhesion and normal morphology on the surfaces at 24 and 72 hr. The results of live cell counts are presented in **Fig. 4.30b**. The PEO treated surfaces have higher live cell counts compared to the as-polished with significant level of $p < 0.001$. However, no significant difference was observed among the PEO treated groups. This indicates that cell adhesion depends on surface topography and wettability rather than the presence of the different TiO_2 phase structures. It is good to note that the number of dead cells has no significant difference for all groups. These data present evidence that the PEO treatment of Ti in KOH + $K_4P_2O_7$ electrolyte can enhance biomimetic apatite formation as well as cell viability without any cytotoxic effect.

Chapter 5 Conclusions

5.1. Plasma electrolytic saturation (PES)

– PES of Ti produced a characteristic hierarchical surface profile comprised 2-3 μm height hills and valleys with nanoscale roughness. The roughness increased with processing time, but it remained below 200 nm. Analysis of PES profile parameters showed the development of several beneficial profile characteristics including a major increase in the ratio of the actual surface area to projection area.

– The studies give the fundamental understanding that PES produced profile with very large actual surface area, *r*, resulted in high critical contact angle values inducing *hemi-wicking* and significant reduction in the droplet contact angle. The PES treatment was able to produce desirable profile characteristics on pure Ti surface resulting in superhydrophilic behavior.

– Its superhydrophilic surface was able to induce HA formation after immersed in an alternative SBF (α-MEM) for 21 days. *In-vitro* cell culture studies using MC3T3 pre-osteoblast cells indicated the significant enhancement in the cells' viability and proliferation on the PES treated Ti surface compared to the untreated Ti.

5.2. Plasma electrolytic oxidation (PEO)

- PEO of Ti in potassium - phosphate electrolyte produced TiO_2 coatings with a micropore structures. The total number of pores decreased, and their size increased with increasing the applied current density and treatment duration. Although the roughness increased with applied

current density and treatment duration, the roughness of all PEO treated Ti groups remained at low levels, *Sa* 630 – 930 nm.

– The ratio of actual surface area to the projected area (*r*) decreased as increased current density and treatment duration. However, the *r* values in all PEO coatings are much larger than that of the PES treated Ti. The presence of negatively charge PO_4^{3-} and high *r* values of the PEO coatings were responsible for the superhydrophilic characteristic, contact angle smaller than 1°.

– The treated Ti groups were able to induce biomimetic apatite formation after immersion in α-MEM. *In-vitro* cell culture studies using human MSCs indicated the significant enhancement in the cells' viability on the PEO treated groups without any cytotoxic effect.

– The results in this study provide an evidence that anatase and rutile show no significant difference in terms of biomimetic apatite formation ability, cell proliferation, and cell viability.

References

[1] V. Vijayaraghavan, A. V. Sabane, K. Tejas, Hypersensitivity to titanium: A less explored area of research, J. Indian Prosthodont. Soc. 12 (2012) 201–207. https://doi.org/10.1007/s13191-012-0139-4.

[2] D.D. Bosshardt, V. Chappuis, D. Buser, Osseointegration of titanium, titanium alloy and zirconia dental implants: current knowledge and open questions, Periodontol. 2000. 73 (2017) 22–40. https://doi.org/10.1111/prd.12179.

[3] E. Mohseni, E. Zalnezhad, A.R. Bushroa, Comparative investigation on the adhesion of hydroxyapatite coating on Ti-6Al-4V implant: A review paper, Int. J. Adhes. Adhes. 48 (2014) 238–257. https://doi.org/10.1016/j.ijadhadh.2013.09.030.

[4] X. Zheng, M. Huang, C. Ding, Bond strength of plasma-sprayed hydroxyapatite/Ti composite coatings, Biomaterials. 21 (2000) 841–849. https://doi.org/10.1016/S0142-9612(99)00255-0.

[5] A. Wennerberg, T. Albrektsson, Effects of titanium surface topography on bone integration: A systematic review, Clin. Oral Implants Res. 20 (2009) 172–184. https://doi.org/10.1111/j.1600-0501.2009.01775.x.

[6] A. Wennerberg, R. Jimbo, S. Stübinger, M. Obrecht, M. Dard, S. Berner, Nanostructures and hydrophilicity influence osseointegration: A biomechanical study in the rabbit tibia, Clin. Oral Implants Res. 25 (2014) 1041–1050. https://doi.org/10.1111/clr.12213.

[7] K.M. Hotchkiss, G.B. Reddy, S.L. Hyzy, Z. Schwartz, B.D. Boyan, R. Olivares-Navarrete, Titanium surface characteristics, including topography and wettability, alter macrophage activation, Acta Biomater. 31 (2016) 425–434.

https://doi.org/10.1016/j.actbio.2015.12.003.

[8] M.Z. Jorge, J.M. Granjeiro, S.C. Sartoretto, M.D. Calasans-Maia, A.T.N.N. Alves, L. Zarranz, Hydrophilic surface of Ti6Al4V-ELI alloy improves the early bone apposition of sheep tibia, Clin. Oral Implants Res. 28 (2016) 893–901. https://doi.org/10.1111/clr.12894.

[9] E.M. Lotz, R. Olivares-Navarrete, S. Berner, B.D. Boyan, Z. Schwartz, Osteogenic response of human MSCs and osteoblasts to hydrophilic and hydrophobic nanostructured titanium implant surfaces, J. Biomed. Mater. Res. - Part A. 104 (2016) 3137–3148. https://doi.org/10.1002/jbm.a.35852.

[10] A. Smith, R. Kelton, E.I. Meletis, Deposition of Ni Coatings by Electrolytic Plasma Processing, Plasma Chem. Plasma Process. 35 (2015) 963–978. https://doi.org/10.1007/s11090-015-9642-9.

[11] M. Aliofkhazraei, A.S. Rouhaghdam, P. Gupta, Nano-fabrication by cathodic plasma electrolysis, Crit. Rev. Solid State Mater. Sci. 36 (2011) 174–190. https://doi.org/10.1080/10408436.2011.593269.

[12] E.I. Meletis, X. Nie, F.L. Wang, J.C. Jiang, Electrolytic plasma processing for cleaning and metal-coating of steel surfaces, Surf. Coat. Technol. 150 (2002) 246–256. https://doi.org/10.1016/S0257-8972(01)01521-3.

[13] A.R. Rafieerad, M.R. Ashra, R. Mahmoodian, A.R. Bushroa, Surface characterization and corrosion behavior of calcium phosphate-base composite layer on titanium and its alloys via plasma electrolytic oxidation: A review paper, Mater. Sci. Eng. C. 57 (2015) 397–413. https://doi.org/10.1016/j.msec.2015.07.058.

[14] M. Qadir, Y. Li, K. Munir, C. Wen, Calcium Phosphate-Based Composite Coating by

Micro-Arc Oxidation (MAO) for Biomedical Application: A Review, Crit. Rev. Solid State Mater. Sci. 43 (2018) 392–416. https://doi.org/10.1080/10408436.2017.1358148.

[15] Y. Wang, H. Yu, C. Chen, Z. Zhao, Review of the biocompatibility of micro-arc oxidation coated titanium alloys, Mater. Des. 85 (2015) 640–652. https://doi.org/10.1016/j.matdes.2015.07.086.

[16] G. Mortazavi, J. Jiang, E.I. Meletis, Investigation of the plasma electrolytic oxidation mechanism of titanium, Appl. Surf. Sci. 488 (2019) 370–382. https://doi.org/10.1016/j.apsusc.2019.05.250.

[17] X. Liu, P.K. Chu, C. Ding, Surface modification of titanium, titanium alloys, and related materials for biomedical applications, Mater. Sci. Eng. R Reports. 47 (2004) 49–121. https://doi.org/10.1016/j.mser.2004.11.001.

[18] C. Oldani, A. Dominguez, Titanium as a Biomaterial for Implants, in: Recent Adv. Arthroplast., InTech, 2012. https://doi.org/10.5772/27413.

[19] M. Long, H.J. Rack, Titanium alloys in total joint replacement-a materials science perspective, Biomaterials. 19 (1998) 1621–1639. https://ac-els-cdn-com.ezproxy.uta.edu/S0142961297001464/1-s2.0-S0142961297001464-main.pdf?_tid=7f9b9213-fc4d-4864-82f9-cfc153464254&acdnat=1551136660_97cd0a6118691df0731a33ecce80c7fb (accessed February 25, 2019).

[20] R. Junker, A. Dimakis, M. Thoneick, J.A. Jansen, Effects of implant surface coatings and composition on bone integration: A systematic review, Clin. Oral Implants Res. 20 (2009) 185–206. https://doi.org/10.1111/j.1600-0501.2009.01777.x.

[21] A. Alenezi, Y. Naito, M. Andersson, B.R. Chrcanovic, A. Wennerberg, R. Jimbo,

Characteristics of 2 Different Commercially Available Implants with or without Nanotopography, Int. J. Dent. 2013 (2013) 1–8. https://doi.org/10.1155/2013/769768.

[22] X.Z. Ding, X.H. Liu, Y.Z. He, Grain size dependence of anatase-to-rutile structural transformation in gel-derived nanocrystalline titania powders, J. Mater. Sci. Lett. 15 (1996) 1789–1791. https://doi.org/10.1007/BF00275343.

[23] A. Beltrán, L. Gracia, J. Andrés, Density functional theory study of the brookite surfaces and phase transitions between natural titania polymorphs, J. Phys. Chem. B. 110 (2006) 23417–23423. https://doi.org/10.1021/jp0643000.

[24] H. Zhang, J.F. Banfield, Thermodynamic analysis of phase stability of nanocrystalline titania, J. Mater. Chem. 8 (1998) 2073–2076. https://doi.org/10.1039/a802619j.

[25] F. Lindberg, J. Heinrichs, F. Ericson, P. Thomsen, H. Engqvist, Hydroxylapatite growth on single-crystal rutile substrates, Biomaterials. 29 (2008) 3317–3323. https://doi.org/10.1016/j.biomaterials.2008.04.034.

[26] N. Moritz, S. Areva, J. Wolke, T. Peltola, TF-XRD examination of surface-reactive TiO2 coatings produced by heat treatment and CO2 laser treatment, Biomaterials. 26 (2005) 4460–4467. https://doi.org/10.1016/j.biomaterials.2004.11.020.

[27] B. Yang, M. Uchida, H.M. Kim, X. Zhang, T. Kokubo, Preparation of bioactive titanium metal via anodic oxidation treatment, Biomaterials. 25 (2004) 1003–1010. https://doi.org/10.1016/S0142-9612(03)00626-4.

[28] M. Uchida, H.M. Kim, T. Kokubo, S. Fujibayashi, T. Nakamura, Structural dependence of apatite formation on titania gels in a simulated body fluid, J. Biomed. Mater. Res. - Part A. 64A (2003) 164–170. https://doi.org/10.1002/jbm.a.10414.

[29] C.M. Lin, S.K. Yen, Biomimetic growth of apatite on electrolytic TiO2 coatings in

simulated body fluid, Mater. Sci. Eng. C. 26 (2006) 54–64. https://doi.org/10.1016/j.msec.2005.06.048.

[30] K.R. Shin, Y.G. Ko, D.H. Shin, Effect of electrolyte on surface properties of pure titanium coated by plasma electrolytic oxidation, J. Alloys Compd. 509S (2011) S478–S481. https://doi.org/10.1016/j.jallcom.2011.02.056.

[31] X. Cui, H.M. Kim, M. Kawashita, L. Wang, T. Xiong, T. Kokubo, T. Nakamura, Preparation of bioactive titania films on titanium metal via anodic oxidation, Dent. Mater. 25 (2009) 80–86. https://doi.org/10.1016/j.dental.2008.04.012.

[32] M. Kaseem, S. Fatimah, N. Nashrah, Y.G. Ko, Recent progress in surface modification of metals coated by plasma electrolytic oxidation: Principle, structure, and performance, Prog. Mater. Sci. (2020) Article in Press. https://doi.org/10.1016/j.pmatsci.2020.100735.

[33] P. Fauchais, Understanding plasma spraying, J. Phys. D. Appl. Phys. 37 (2004) R86–R108. https://doi.org/10.1088/0022-3727/37/9/R02.

[34] T.J. Levingstone, M. Ardhaoui, K. Benyounis, L. Looney, J.T. Stokes, Plasma sprayed hydroxyapatite coatings: Understanding process relationships using design of experiment analysis, Surf. Coat. Technol. 283 (2015) 29–36. https://doi.org/10.1016/j.surfcoat.2015.10.044.

[35] K.Y. Hung, S.C. Lo, C.S. Shih, Y.C. Yang, H.P. Feng, Y.C. Lin, Titanium surface modified by hydroxyapatite coating for dental implants, Surf. Coat. Technol. 231 (2013) 337–345. https://doi.org/10.1016/j.surfcoat.2012.03.037.

[36] L.G. Ellies, D.G.A. Nelson, J.D.B. Featherstone, Crystallographic changes in calcium phosphates during plasma-spraying, Biomaterials. 13 (1992) 313–316. https://doi.org/10.1016/0142-9612(92)90055-S.

[37] Y.C. Tsui, C. Doyle, T.W. Clyne, Plasma sprayed hydroxyapatite coatings on titanium substrates. Part 1: Mechanical properties and residual stress levels, Biomaterials. 19 (1998) 2015–2029. https://doi.org/10.1016/S0142-9612(98)00103-3.

[38] T.F. Stoica, C. Morosanu, A. Slav, T. Stoica, P. Osiceanu, C. Anastasescu, M. Gartner, M. Zaharescu, Hydroxyapatite films obtained by sol-gel and sputtering, Thin Solid Films. 516 (2008) 8112–8116. https://doi.org/10.1016/j.tsf.2008.04.071.

[39] J.A. Lenis, F.M. Hurtado, M.A. Gómez, F.J. Bolívar, Effect of thermal treatment on structure, phase and mechanical properties of hydroxyapatite thin films grown by RF magnetron sputtering, Thin Solid Films. 669 (2019) 571–578. https://doi.org/10.1016/j.tsf.2018.11.045.

[40] W. Boonrawd, M. Hamdi, A. Shukor, T.C. Yong, Radio Frequency Magnetron Sputtering HA / Ti Coatings Deposited Using Double-Layered Target: Phase Composition and Film Adherence of Heat-Treated Coatings, in: 11th Asia Pacific Ind. Eng. Manag. Syst. Conf., Melaka, Malaysia, 2010: pp. 7–10. https://www.researchgate.net/publication/228503304.

[41] C.J. Brinker, C.S. Ashley, R.A. Cairncross, K.S. Chen, A.J. Hurd, S.T. Reed, J. Samuel, P.R. Schunk, R.W. Schwartz, C.S. Scotto, Sol—gel derived ceramic films — fundamentals and applications, in: Metall. Ceram. Prot. Coatings, Springer Netherlands, Dordrecht, 1996: pp. 112–151. https://doi.org/10.1007/978-94-009-1501-5_6.

[42] T. Olding, M. Sayer, D. Barrow, Ceramic sol–gel composite coatings for electrical insulation, Thin Solid Films. 398–399 (2001) 581–586. https://doi.org/10.1016/S0040-6090(01)01322-0.

[43] K.A. Gross, C.S. Chai, G.S.K. Kannangara, B. Ben-Nissan, L. Hanley, Thin hydroxyapatite coatings via sol–gel synthesis, J. Mater. Sci. Mater. Med. 9 (1998) 839–

843. https://doi.org/10.1023/A:1008948228880.

[44] P. Layrolle, A. Ito, T. Tateishi, Sol-Gel Synthesis of Amorphous Calcium Phosphate and Sintering into Microporous Hydroxyapatite Bioceramics, J. Am. Ceram. Soc. 81 (2005) 1421–1428. https://doi.org/10.1111/j.1151-2916.1998.tb02499.x.

[45] M.-F. Hsieh, L.-H. Perng, T.-S. Chin, H.-G. Perng, Phase purity of sol–gel-derived hydroxyapatite ceramic, Biomaterials. 22 (2001) 2601–2607. https://doi.org/10.1016/S0142-9612(00)00448-8.

[46] T. Kokubo, S. Yamaguchi, Bioactive Ti metal and its alloys prepared by chemical treatments: State-of-the-art and future trends, Adv. Eng. Mater. 10 (2010) B579–B591. https://doi.org/10.1002/adem.201080087.

[47] H.M. Kim, F. Miyaji, T. Kokubo, T. Nakamura, Preparation of bioactive Ti and its alloys via simple chemical surface treatment, J. Biomed. Mater. Res. 32 (1996) 409–417. https://doi.org/10.1002/(SICI)1097-4636(199611)32:3<409::AID-JBM14>3.0.CO;2-B.

[48] H.M. Kim, T. Kokubo, S. Fujibayashi, S. Nishiguchi, T. Nakamura, Bioactive macroporous titanium surface layer on titanium substrate, J. Biomed. Mater. Res. 52 (2000) 553–557. https://doi.org/10.1002/1097-4636(20001205)52:3<553::AID-JBM14>3.0.CO;2-X.

[49] S.I. Tanaka, H. Tobimatsu, Y. Maruyama, T. Tanaki, G. Jerkiewicz, Preparation and characterization of microporous layers on titanium, ACS Appl. Mater. Interfaces. 1 (2009) 2312–2319. https://doi.org/10.1021/am900474h.

[50] S. Ban, Effect of alkaline treatment of pure titanium and its alloys on the bonding strength of dental veneering resins, J. Biomed. Mater. Res. - Part A. 66A (2003) 138–145. https://doi.org/10.1002/jbm.a.10566.

[51] T. Kokubo, H.M. Kim, M. Kawashita, T. Nakamura, Bioactive metals: Preparation and properties, J. Mater. Sci. Mater. Med. 15 (2004) 99–107. https://doi.org/10.1023/B:JMSM.0000011809.36275.0c.

[52] T. Kokubo, H.M. Kim, M. Kawashita, Novel bioactive materials with different mechanical properties, Biomaterials. 24 (2003) 2161–2175. https://doi.org/10.1016/S0142-9612(03)00044-9.

[53] T. Kawai, T. Kizuki, H. Takadama, T. Matsushita, H. Unuma, T. Nakamura, T. Kokubo, Apatite formation on surface titanate layer with different Na content on Ti metal, J. Ceram. Soc. Japan. 118 (2010) 19–24. https://doi.org/10.2109/jcersj2.118.19.

[54] M. Wei, H.M. Kim, T. Kokubo, J.H. Evans, Optimising the bioactivity of alkaline-treated titanium alloy, Mater. Sci. Eng. C. 20 (2002) 125–134. https://doi.org/10.1016/S0928-4931(02)00022-X.

[55] L.F. Cooper, A role for surface topography in creating and maintaining bone at titanium endosseous implants, J. Prosthet. Dent. 84 (2000) 522–534. https://doi.org/10.1067/mpr.2000.111966.

[56] M.L.R. Schwarz, M. Kowarsch, S. Rose, K. Becker, L. Jani, L. Jani, Effect of surface roughness, porosity, and a resorbable calcium phosphate coating on osseointegration of titanium in a minipig model, J. Biomed. Mater. Res. Part A. 89A (2008) 667–678. https://doi.org/10.1002/jbm.a.32000.

[57] Y. Liu, J. Wang, X. Chen, F. Deng, C. Zhang, J. Xu, Improved bioactivity of selective laser melting titanium: Surface modification with micro-/nano-textured hierarchical topography and bone regeneration performance evaluation, Mater. Sci. Eng. C. 68 (2016) 229–240. https://doi.org/10.1016/j.msec.2016.05.096.

[58] A.L. Yerokhin, X. Nie, A. Leyland, A. Matthews, S.J. Dowey, Plasma electrolysis for surface engineering, Surf. Coat. Technol. 122 (1999) 73–93. https://doi.org/10.1016/S0257-8972(99)00441-7.

[59] C. Cionea, Microstructualral Evolution of Surface Layers During Electrolytic Plasma Processing, The University of Texas at Arlington, 2010.

[60] S. Liu, B. Li, C. Liang, H. Wang, Z. Qiao, Formation mechanism and adhesive strength of a hydroxyapatite/TiO2 composite coating on a titanium surface prepared by micro-arc oxidation, Appl. Surf. Sci. 362 (2016) 109–114. https://doi.org/10.1016/j.apsusc.2015.11.086.

[61] M. Petković, S. Stojadinović, R. Vasilić, L. Zeković, Characterization of oxide coatings formed on tantalum by plasma electrolytic oxidation in 12-tungstosilicic acid, Appl. Surf. Sci. 257 (2011) 10590–10594. https://doi.org/10.1016/j.apsusc.2011.07.055.

[62] R.O. Hussein, X. Nie, D.O. Northwood, A. Yerokhin, A. Matthews, Spectroscopic study of electrolytic plasma and discharging behaviour during the plasma electrolytic oxidation (PEO) process, J. Phys. D. Appl. Phys. 43 (2010) 105203. https://doi.org/10.1088/0022-3727/43/10/105203.

[63] G. Lv, W. Gu, H. Chen, W. Feng, M.L. Khosa, L. Li, E. Niu, G. Zhang, S.Z. Yang, Characteristic of ceramic coatings on aluminum by plasma electrolytic oxidation in silicate and phosphate electrolyte, Appl. Surf. Sci. 253 (2006) 2947–2952. https://doi.org/10.1016/j.apsusc.2006.06.036.

[64] H. Duan, C. Yan, F. Wang, Growth process of plasma electrolytic oxidation films formed on magnesium alloy AZ91D in silicate solution, Electrochim. Acta. 52 (2007) 5002–5009. https://doi.org/10.1016/j.electacta.2007.02.021.

[65] R.O. Hussein, X. Nie, D.O. Northwood, An investigation of ceramic coating growth mechanisms in plasma electrolytic oxidation (PEO) processing, Electrochim. Acta. 112 (2013) 111–119. https://doi.org/10.1016/j.electacta.2013.08.137.

[66] B.L. Jiang, Y.M. Wang, Plasma electrolytic oxidation treatment of aluminium and titanium alloys, in: H. Dong (Ed.), Surf. Eng. Light Alloy. Alum. Magnes. Titan. Alloy., Woodhead Publishing Limted, Cambridge, 2010. https://doi.org/10.1533/9781845699451.2.110.

[67] W.H. Song, Y.K. Jun, Y. Han, S.H. Hong, Biomimetic apatite coatings on micro-arc oxidized titania, Biomaterials. 25 (2004) 3341–3349. https://doi.org/10.1016/j.biomaterials.2003.09.103.

[68] M.A. Faghihi-Sani, A. Arbabi, A. Mehdinezhad-Roshan, Crystallization of hydroxyapatite during hydrothermal treatment on amorphous calcium phosphate layer coated by PEO technique, Ceram. Int. 39 (2013) 1793–1798. https://doi.org/10.1016/j.ceramint.2012.08.026.

[69] S. Durdu, Ö.F. Deniz, I. Kutbay, M. Usta, Characterization and formation of hydroxyapatite on Ti6Al4V coated by plasma electrolytic oxidation, J. Alloys Compd. 551 (2013) 422–429. https://doi.org/10.1016/j.jallcom.2012.11.024.

[70] F. Blateyron, The areal field parameters, in: R. Leach (Ed.), Characterisation Areal Surf. Texture, Springer, New York, 2013: pp. 15–43. https://doi.org/10.1007/978-3-642-36458-7_2.

[71] J. Drelich, E. Chibowski, D.D. Meng, K. Terpilowski, Hydrophilic and superhydrophilic surfaces and materials, Soft Matter. 7 (2011) 9804–9828. https://doi.org/10.1039/c1sm05849e.

[72] H.P. Jennissen, Hyperhydrophilic rough surfaces and imaginary contact angles, Materwiss. Werksttech. 43 (2012) 743–750. https://doi.org/10.1002/mawe.201200961.

[73] T. Young, An essay on the cohesion of fluids, Philos. Trans. R. Soc. Lond. 95 (1804) 65–87. https://doi.org/10.1098/rstl.1805.0005.

[74] W.A. Zisman, Relation of the Equilibrium Contact Angle to Liquid and Solid Constitution, in: R.F. Gould (Ed.), Contact Angle, Wettability, Adhes., American Chemical Society, Washington, DC, 1964: pp. 1–51. https://doi.org/10.1021/ba-1964-0043.ch001.

[75] R.N. Wenzel, Resistance of solid surfaces to wetting by water, Ind. Eng. Chem. 28 (1936) 988–994. https://doi.org/10.1021/ie50320a024.

[76] E.Y. Gatapova, A.A. Semenov, D. V. Zaitsev, O.A. Kabov, Evaporation of a sessile water drop on a heated surface with controlled wettability, Colloids Surf. A Physicochem. Eng. Asp. 441 (2014) 776–785. https://doi.org/10.1016/j.colsurfa.2013.05.046.

[77] S. Shibuichi, T. Onda, N. Satoh, K. Tsujii, Super water-repellent surfaces resulting from fractal structure, J. Phys. Chem. 100 (1996) 19512–19517. https://doi.org/10.1021/jp9616728.

[78] P. Roach, N.J. Shirtcliffe, M.I. Newton, Progess in superhydrophobic surface development, Soft Matter. 4 (2008) 224–240. https://doi.org/10.1039/b712575p.

[79] R.A. Fleming, M. Zou, Silica nanoparticle-based films on titanium substrates with long-term superhydrophilic and superhydrophobic stability, Appl. Surf. Sci. 280 (2013) 820–827. https://doi.org/10.1016/j.apsusc.2013.05.068.

[80] X. Liu, Y. Liang, F. Zhou, W. Liu, Extreme wettability and tunable adhesion: Biomimicking beyond nature?, Soft Matter. 8 (2012) 2070–2086.

https://doi.org/10.1039/c1sm07003g.

[81] E.A. Cavalcanti-Adam, Building nanobridges for cell adhesion, Nat. Mater. 18 (2019) 1272–1273. https://doi.org/10.1038/s41563-019-0537-7.

[82] W. Yang, L. Sun, S. Cai, Y. Chen, W. Liang, P. Zhou, H. Yu, Y. Wang, L. Liu, Dynamically directing cell organization: Via micro-hump structure patterned cell-adhered interfaces, Lab Chip. 20 (2020) 2447–2452. https://doi.org/10.1039/d0lc00477d.

[83] S. Cai, C. Wu, W. Yang, W. Liang, H. Yu, L. Liu, Recent advance in surface modification for regulating cell adhesion and behaviors, Nanotechnol. Rev. 9 (2020) 971–989. https://doi.org/10.1515/ntrev-2020-0076.

[84] S.B. Kennedy, N.R. Washburn, C.G. Simon, E.J. Amis, Combinatorial screen of the effect of surface energy on fibronectin-mediated osteoblast adhesion, spreading and proliferation, Biomaterials. 27 (2006) 3817–3824. https://doi.org/10.1016/j.biomaterials.2006.02.044.

[85] N.J. Hallab, K.J. Bundy, K. O'Connor, R.L. Moses, J.J. Jacobs, Evaluation of metallic and polymeric biomaterial surface energy and surface roughness characteristics for directed cell adhesion, Tissue Eng. 7 (2001) 55–71. https://doi.org/10.1089/107632700300003297.

[86] D.A. Porter, K.E. Easterling, Phase transformations in metals and alloys, Third, CRC Press, New York, 2009.

[87] R.J. Good, C.J. van Oss, The Modern Theory of Contact Angles and the Hydrogen Bond Components of Surface Energies, in: M.E. Schrader, G. Il Loeb (Eds.), Mod. Approaches to Wettability Theory Appl., Springer US, Boston, MA, 1992: pp. 1–27. https://doi.org/10.1007/978-1-4899-1176-6_1.

[88] E. Spooner, A guide to surface energy, (2021). https://www.ossila.com/pages/a-guide-to-

surface-energy.

[89] D.K. Owens, R.C. Wendt, Estimation of the surface free energy of polymers, J. Appl. Polym. Sci. 13 (1969) 1741–1747. https://doi.org/10.1002/app.1969.070130815.

[90] D.H. Kaelble, Dispersion-Polar Surface Tension Properties of Organic Solids, J. Adhes. 2 (1970) 66–81. https://doi.org/10.1080/0021846708544582.

[91] K.R. Awad, N. Ahuja, A. Shah, H. Tran, P.B. Aswath, M. Brotto, V. Varanasi, Silicon nitride enhances osteoprogenitor cell growth and differentiation via increased surface energy and formation of amide and nanocrystalline HA for craniofacial reconstruction, Med. Devices Sens. 2 (2019) e10032. https://doi.org/10.1002/mds3.10032.

[92] J.T.Y. Lee, Y. Leng, K.L. Chow, F. Ren, X. Ge, K. Wang, X. Lu, Cell culture medium as an alternative to conventional simulated body fluid, Acta Biomater. 7 (2011) 2615–2622. https://doi.org/10.1016/j.actbio.2011.02.034.

[93] M. Bohner, J. Lemaitre, Can bioactivity be tested in vitro with SBF solution?, Biomaterials. 30 (2009) 2175–2179. https://doi.org/10.1016/j.biomaterials.2009.01.008.

[94] J. Caetano-Lopes, H. Canhão, J.E. Fonseca, Osteoblasts and bone formation, Acta Reum. Port. 32 (2007) 103–110. https://doi.org/10.1016/s0169-6009(08)80210-3.

[95] D.J. Prockop, Marrow Stromal Cells as Stem Cells for Nonhematopoietic Tissues, Science (80-.). 276 (1997) 71 LP – 74. https://doi.org/10.1126/science.276.5309.71.

[96] S.E. Haynesworth, J. Goshima, V.M. Goldberg, A.I. Caplan, Characterization of cells with osteogenic potential from human marrow, Bone. 13 (1992) 81–88. https://doi.org/https://doi.org/10.1016/8756-3282(92)90364-3.

[97] G.H. Altman, R.L. Horan, I. Martin, J. Farhadi, P.R.H. Stark, V. Volloch, J.C. Richmond, G. Vunjak-Novakovic, D.L. Kaplan, Cell differentiation by mechanical stress, FASEB J.

16 (2002) 1–13. https://doi.org/https://doi.org/10.1096/fj.01-0656fje.

[98] J.N. Beresford, J.H. Bennett, C. Devlin, M.E. Owen, Evidence for an inverse relationship between the differentiation of adipocytic and osteogenic cells, Bone Miner. 17 (1992) 198. https://doi.org/https://doi.org/10.1016/0169-6009(92)92129-E.

[99] S. Wakitani, T. Goto, S.J. Pineda, R.G. Young, J.M. Mansour, A.I. Caplan, V.M. Goldberg, Mesenchymal cell-based repair of large, full-thickness defects of articular cartilage., JBJS. 76 (1994).

[100] B. Johnstone, T.M. Hering, A.I. Caplan, V.M. Goldberg, J.U. Yoo, In VitroChondrogenesis of Bone Marrow-Derived Mesenchymal Progenitor Cells, Exp. Cell Res. 238 (1998) 265–272. https://doi.org/https://doi.org/10.1006/excr.1997.3858.

[101] S. Wakitani, T. Saito, A.I. Caplan, Myogenic cells derived from rat bone marrow mesenchymal stem cells exposed to 5-azacytidine, Muscle Nerve. 18 (1995) 1417–1426. https://doi.org/https://doi.org/10.1002/mus.880181212.

[102] H.P. Jennissen, Ultra-hydrophilic transition metals as histophilic biomaterials, Macromol. Symp. 225 (2005) 43–69. https://doi.org/10.1002/masy.200550705.

[103] C.N. Elias, Y. Oshida, J.H.C. Lima, C.A. Muller, Relationship between surface properties (roughness, wettability and morphology) of titanium and dental implant removal torque, J. Mech. Behav. Biomed. Mater. 1 (2008) 234–242. https://doi.org/10.1016/j.jmbbm.2007.12.002.

[104] L. Le Guéhennec, A. Soueidan, P. Layrolle, Y. Amouriq, Surface treatments of titanium dental implants for rapid osseointegration, Dent. Mater. 23 (2007) 844–854. https://doi.org/10.1016/j.dental.2006.06.025.

[105] J. Bico, C. Tordeux, D. Quéré, Rough wetting, Europhys. Lett. 55 (2001) 214–220.

https://doi.org/10.1209/epl/i2001-00402-x.

[106] W. Gui, J. Lin, G. Hao, Y. Qu, Y. Liang, H. Zhang, Electrolytic plasma processing-an innovative treatment for surface modification of 304 stainless steel, Sci. Rep. 7 (2017) 1–7. https://doi.org/10.1038/s41598-017-00204-w.

[107] R. Leach, Characterisation of areal surface texture, Springer, London, 2013. https://doi.org/10.1007/978-3-642-36458-7.

[108] A.B.D. Cassie, S. Baxter, Wettability of porous surfaces, Trans. Faraday Soc. 40 (1944) 546–551. https://doi.org/10.1039/tf9444000546.

[109] B.S. Kim, S. Shin, S.J. Shin, K.M. Kim, H.H. Cho, Control of superhydrophilicity/superhydrophobicity using silicon nanowires via electroless etching method and fluorine carbon coatings, Langmuir. 27 (2011) 10148–10156. https://doi.org/10.1021/la200940j.

[110] S. Xu, S. Hartvickson, J.X. Zhao, Increasing surface area of silica nanoparticles with a rough surface, ACS Appl. Mater. Interfaces. 3 (2011) 1865–1872. https://doi.org/10.1021/am200052a.

[111] C.W. Extrand, Criteria for ultralyophobic surfaces, Langmuir. 20 (2004) 5013–5018. https://doi.org/10.1021/la036481s.

[112] T.A. Otitoju, A.L. Ahmad, B.S. Ooi, Superhydrophilic (superwetting) surfaces: A review on fabrication and application, J. Ind. Eng. Chem. 47 (2017) 19–40. https://doi.org/10.1016/j.jiec.2016.12.016.

[113] T. Pratap, K. Patra, Fabrication of micro-textured surfaces using ball-end micromilling for wettability enhancement of Ti-6Al-4V, J. Mater. Process. Technol. 262 (2018) 168–181. https://doi.org/10.1016/j.jmatprotec.2018.06.035.

[114] X. Zhu, R. Reichl, J. Geis-Gerstorfer, J. Chen, L. Scheideler, Effects of topography and composition of titanium surface oxides on osteoblast responses, Biomaterials. 25 (2003) 4087–4103. https://doi.org/10.1016/j.biomaterials.2003.11.011.

[115] G. McHale, N.J. Shirtcliffe, S. Aqil, C.C. Perry, M.I. Newton, Topography driven spreading, Phys. Rev. Lett. 93 (2004) 036102 1–4. https://doi.org/10.1103/PhysRevLett.93.036102.

[116] R.A. Fleming, M. Zou, Fabrication of stable superhydrophilic surfaces on titanium substrates, J. Adhes. Sci. Technol. 28 (2014) 823–832. https://doi.org/10.1080/01694243.2012.697754.

[117] X. Lu, Y. Leng, Theoretical analysis of calcium phosphate precipitation in simulated body fluid, Biomaterials. 26 (2005) 1097–1108. https://doi.org/10.1016/j.biomaterials.2004.05.034.

[118] D.R. Schmidt, H. Waldeck, W.J. Kao, Protein Adsorption to Biomaterials, in: D.A. Puleo, R. Bizios (Eds.), Biol. Interact. Mater. Surfaces Underst. Control. Protein, Cell, Tissue Responses, Spring, New York, 2009.

[119] J. Saruta, N. Sato, M. Ishijima, T. Okubo, M. Hirota, T. Ogawa, Disproportionate effect of sub-micron topography on osteoconductive capability of titanium, Int. J. Mol. Sci. 20 (2019) 4027 1–15. https://doi.org/10.3390/ijms20164027.

[120] F.A. Shah, K. Grandfield, A. Palmquist, 9 - Laser surface modification and the tissue-implant interface, in: R. Vilar (Ed.), Laser Surf. Modif. Biomater. Tech. Appl., Elsevier Ltd, New York, 2016. https://doi.org/10.1016/B978-0-08-100883-6.00009-5.

[121] H. Wang, N. Eliaz, Z. Xiang, H.P. Hsu, M. Spector, L.W. Hobbs, Early bone apposition in vivo on plasma-sprayed and electrochemically deposited hydroxyapatite coatings on

titanium alloy, Biomaterials. 27 (2006) 4192–4203. https://doi.org/10.1016/j.biomaterials.2006.03.034.

[122] L. Wang, G.H. Nancollas, Calcium orthophosphates: Crystallization and Dissolution, Chem. Rev. 108 (2008) 4628–4669. https://doi.org/10.1021/cr0782574.

[123] H. Gheisari, E. Karamian, M. Abdellahi, A novel hydroxyapatite -Hardystonite nanocomposite ceramic, Ceram. Int. 41 (2015) 5967–5975. https://doi.org/10.1016/j.ceramint.2015.01.033.

[124] X. Nie, A. Leyland, A. Matthews, Deposition of layered bioceramic hydroxyapatite/TiO2 coatings on titanium alloys using a hybrid technique of micro-arc oxidation and electrophoresis, Surf. Coat. Technol. 125 (2000) 407–414. https://doi.org/10.1016/S0257-8972(99)00612-X.

[125] T. Kokubo, H. Takadama, How useful is SBF in predicting in vivo bone bioactivity?, Biomaterials. 27 (2006) 2907–2915. https://doi.org/10.1016/j.biomaterials.2006.01.017.

[126] W. Boonrawd, K.R. Awad, V. Varanasi, E.I. Meletis, Wettability and In-Vitro study of titanium surface profiling prepared by electrolytic plasma processing, Surf. Coat. Technol. 414 (2021) 127119. https://doi.org/10.1016/j.surfcoat.2021.127119.

[127] A. Vitale, S. Guastella, C. Cassinelli, S. Ferraris, E. Bertone, J. Pan, S. Spriano, Multifunctional commercially pure titanium for the improvement of bone integration: Multiscale topography, wettability, corrosion resistance and biological functionalization, Mater. Sci. Eng. C. 60 (2015) 384–393. https://doi.org/10.1016/j.msec.2015.11.049.

[128] Z. Zhao, X. Chen, A. Chen, G. Huo, H. Li, Preparation of K2Ti6O13/TiO2 bio-ceramic on titanium substrate by micro-arc oxidation, J. Mater. Sci. (2009). https://doi.org/10.1007/s10853-009-3869-x.

[129] J. Sun, Y. Han, K. Cui, Microstructure and apatite-forming ability of the MAO-treated porous titanium, Surf. Coat. Technol. (2008). https://doi.org/10.1016/j.surfcoat.2008.03.020.